

Dipartimento di Fisica e Astronomia  
Corso di Laurea magistrale in Astrofisica e Cosmologia

**SIMCADO spatially resolved simulations of  
high-z optically dark galaxies for  
ELT/MORFEO**

Tesi di Laurea Magistrale

Presentata da:  
Lorenzo Pasquale

Relatore:  
Chiar.mo Prof. Cristian Vignali

Correlatrici:  
Dott.ssa Carlotta Gruppioni  
Dott.ssa Francesca Annibali

# Contents

<b>Abstract</b>	<b>iii</b>
<b>Sommario</b>	<b>v</b>
<b>1 Introduction</b>	<b>1</b>
1.1 Galaxy Formation and Evolution . . . . .	1
1.2 The Cosmic Star Formation History . . . . .	4
1.2.1 Star Formation in Galaxies . . . . .	4
1.2.2 Star Formation Rate Density and Stellar Mass Density . . . . .	7
1.3 Dusty Star-Forming Galaxies at High Redshift . . . . .	11
1.4 HST-dark Galaxies . . . . .	13
1.5 Thesis Goals . . . . .	14
<b>2 ESO’s ELT: The World’s Biggest Eye on the Sky</b>	<b>18</b>
2.1 ELT Design and Mirrors . . . . .	20
2.2 ELT Instruments . . . . .	24
2.3 MICADO . . . . .	25
2.4 MORFEO . . . . .	27
2.4.1 MORFEO Design . . . . .	29
2.5 Science Cases . . . . .	30
<b>3 Simulating HST-dark galaxies with SIMCADO</b>	<b>35</b>
3.1 Main Assumptions . . . . .	38
3.2 Local LIRGs . . . . .	39
3.2.1 The task <i>source-from-image</i> and the plate scale . . . . .	42
3.2.2 The Flux-Luminosity Distance Relation . . . . .	43
3.2.3 High-z Emission of Local LIRGs/ULIRGs . . . . .	48
3.3 HST-dark galaxies . . . . .	49

<b>4</b>	<b>Results</b>	<b>64</b>
4.1	Local LIRGs . . . . .	64
4.2	HST-dark galaxies . . . . .	81
4.3	Surface Brightness . . . . .	87
<b>5</b>	<b>Discussion and Conclusions</b>	<b>93</b>
5.1	Final Discussion and Comparison with JWST . . . . .	93
5.2	Summary . . . . .	96

## Abstract

The study of the early Universe and of the first galaxies is a very fascinating, but still debated and poorly understood topic of modern astrophysics. In fact, our knowledge of the high-redshift sources is limited by the capabilities of current instrumentations, since these objects are faint, have small angular sizes, are redshifted and are more peculiar than local galaxies. Our current understanding of early galaxies is mainly based on optical and UV observations, that are likely not representing the whole galaxy population at high redshift. In fact, optical/UV selection necessarily misses sources characterised by large amounts of dust. In this regard, far-infrared (FIR) and sub-millimeter (sub-mm) surveys show that there are high-redshift sources with very faint or even undetected counterparts in the optical and UV, since their star formation takes place in very dusty environments. In this thesis work, I will focus on a recently discovered population of obscured sources, the HST-dark galaxies. These are massive and dusty sources that are not detected by the deepest optical/NIR surveys, but are likely to contribute significantly to the Star Formation Rate Density and the Stellar Mass Density beyond the epoch of major galaxy activity, the so-called Cosmic Noon ( $z \sim 2-3$ ).

As the discovery of HST-dark galaxies is relatively recent and they are invisible (i.e. heavily extinguished by dust) in the wavelength range from UV to NIR, very little is known about their nature and morphology. High-resolution and very deep observations will be needed to obtain accurate and spatially resolved images of these elusive galaxies. All the questions related to their morphologies, star formation and properties could be answered only by observing them with a very high angular resolution and a very large collecting area telescope. In this work, we have considered the capabilities offered by the ESO's Extremely Large Telescope (ELT) as the largest optical/NIR telescope ever build, that will revolutionize the way astronomers observe the whole Universe. Thanks to the combination of its NIR camera MICADO (Multi-AO Imaging CAmera for Deep Observations) and its last-generation adaptive optics system MORFEO (Multiconjugate adaptive Optic Relay For ELT Observations), the ELT will be capable of delivering diffraction-limited images at an unprecedented angular resolution. In particular, in this work we use SIMCADO, a simulator specifically created to produce synthetic images

as they will be obtained by MORFEO+MICADO@ELT. Our purpose is to simulate with SIMCADO -and so predict- how HST-dark galaxies would be observed by the ELT, based on the limited information that we have about them (i.e. their best-fit spectral energy distributions -SEDs-, stellar masses, SFRs and photometric redshifts) in order to verify the possibility to detect high-redshift heavily obscured galaxies, and provide information on the level of detail that the next-generation telescopes will be able to achieve.

In order to simulate how HST-dark galaxies might appear when observed by MORFEO+MICADO@ELT, we use the SEDs of six ALMA-selected HST-dark galaxies and associate to each of them the morphology of a local Luminous/Ultra-Luminous Infrared Galaxy (LIRG/ULIRG). Since the best-fit SEDs of the HST-dark galaxies resemble those of local LIRGs/ULIRGs, that are very dusty and also obscured, it is reasonable to assume that they also share similar morphologies. For this reason, we choose HST images of local LIRGs/ULIRGs associated with the HST-dark SEDs as the starting point of our spatially resolved simulations.

Our simulations show how a telescope with the capabilities of the ELT, coupled with an instrument such as MORFEO+MICADO, will unveil the obscured side of the high-redshift Universe. We demonstrate that, thanks to the unprecedented spatial resolution of MICADO, we will be able to observe details as single knots of star formation (on a scale of  $\sim 0.16$  kpc) and disturbed morphologies up to  $z=4$  for these obscured galaxies.

The fact that ELT will be able to observe and distinguish the shape and morphology of high-redshift sources is not only an unprecedented result, but is also of crucial importance in order to characterize the early Universe, since the investigation of the morphologies of galaxies at high redshift can provide crucial constraints on models of galaxy formation and evolution.

## Sommario

Lo studio dell'Universo primordiale e delle prime galassie è un argomento molto affascinante, ma ancora molto dibattuto e poco conosciuto dell'astrofisica moderna. Infatti, la nostra conoscenza delle sorgenti ad alto redshift è limitata dalle capacità dell'attuale strumentazione, in quanto sono sorgenti deboli, con piccole dimensioni angolari, redshiftate e più peculiari rispetto alle galassie locali. Le nostre attuali informazioni sulle galassie primordiali si basano principalmente su osservazioni ottiche e UV, che non sono rappresentative dell'intera popolazione di galassie ad alto redshift. Infatti, la selezione ottica/UV perde necessariamente sorgenti caratterizzate da grandi quantità di polvere. In realtà, studi nel lontano infrarosso (FIR) e sub-millimetrico (sub-mm) mostrano che ci sono sorgenti ad alto redshift con controparti ottiche e UV molto deboli o addirittura non rilevate, poiché la loro attività di formazione stellare avviene in ambienti molto polverosi.

In questo lavoro di tesi ci concentreremo su una popolazione di sorgenti oscurate recentemente scoperta, le HST-dark galaxies. Esse sono sorgenti massive e polverose che non sono rivelate nelle survey ottiche/NIR più profonde, ma che probabilmente contribuiscono in modo significativo alle Star Formation Rate Density e Stellar Mass Density dopo l'epoca in cui le galassie erano al massimo della loro attività, il cosiddetto Mezzogiorno Cosmico ( $z \sim 2-3$ ).

Data la recente scoperta delle HST-dark galaxies ed il fatto che esse siano invisibili (fortemente oscurate dalla polvere) nel range di lunghezze d'onda dall'UV al NIR, ancora molto poco è noto riguardo la loro natura e morfologia. Infatti, osservazioni ad alta risoluzione e sensibilità saranno necessarie per ottenere immagini accurate e spazialmente risolte di queste galassie sfuggenti. Tutte le domande riguardanti la loro morfologia, formazione stellare e proprietà potranno essere chiarite solo osservandole con un telescopio con una risoluzione angolare molto alta e un'area di raccolta molto ampia. A tal proposito, abbiamo considerato le capacità dell'Extremely Large Telescope (ELT) dell'ESO, il più grande telescopio ottico/NIR mai costruito, che rivoluzionerà il modo in cui gli astronomi osservano l'intero Universo. Grazie alla combinazione della sua camera infrarossa MICADO (Multi-AO Imaging CAmera for Deep Observations) e il suo sistema di ottiche adattive di ultima generazione MORFEO (Multiconjugate adaptive Optic Relay For ELT

Observations), l'ELT sarà capace di fornire immagini al limite di diffrazione ad una risoluzione angolare senza precedenti. In particolare, in questo lavoro abbiamo fatto uso di SIMCADO, un simulatore creato specificatamente per produrre immagini sintetiche come se fossero state ottenute con MORFEO+MICADO@ELT.

Il nostro scopo è quello di simulare con SIMCADO, e quindi predire, come le HST-dark galaxies saranno osservate dall'ELT, basandoci sulle informazioni limitate che abbiamo (cioè i best-fit delle distribuzioni di energia spettrale -SEDs-, le masse stellari, i tassi di formazione stellare e redshift fotometrici), al fine di verificare la possibilità di rilevare galassie fortemente oscurate ad alto redshift, e di fornire informazioni sul livello di dettaglio che i telescopi di nuova generazione saranno in grado di raggiungere.

Per simulare come le HST-dark galaxies potrebbero apparire osservate da MORFEO+MICADO@ELT, abbiamo considerato le SEDs di sei HST-dark galaxies selezionate da ALMA ed associato ad ognuna di queste la morfologia di una Luminous/Ultra-Luminous Infrared Galaxy (LIRG/ULIRG) locale. Infatti, siccome le SEDs di best-fit delle HST-dark galaxies sono simili a quelle delle LIRGs/ULIRGs locali, che sono anch'esse molto polverose ed oscurate, è ragionevole assumere che esse condividano anche una simile morfologia. Per questa ragione, abbiamo scelto immagini di LIRGs/ULIRGs locali associate con le SEDs HST-dark come punto di partenza per le nostre simulazioni spazialmente risolte.

Le nostre simulazioni mostrano come un telescopio dalle capacità di ELT accoppiato con un strumento come MORFEO+MICADO riuscirà a svelare il lato oscurato dell'Universo ad alto redshift. Abbiamo dimostrato che, grazie alla risoluzione spaziale senza precedenti di MICADO, saremo in grado di osservare dettagli come le singole nubi di formazione stellare e morfologie irregolari fino a  $z=4$  per queste galassie oscurate.

Il fatto che l'ELT sarà in grado di osservare e distinguere la forma e la morfologia delle sorgenti ad alto redshift non è solo un risultato senza precedenti, ma è anche di cruciale importanza per caratterizzare l'Universo primordiale, dato che derivazioni dettagliate delle morfologie delle galassie ad alto redshift possono fornire vincoli fondamentali per i modelli di formazione ed evoluzione delle galassie.

# Chapter 1

## Introduction

### 1.1 Galaxy Formation and Evolution

The study of the formation and evolution of galaxies is one of the most debated and prolific fields in modern astrophysics. The first step in the study of this topic requires the definition of the cosmological framework within which these galaxies form and evolve. The currently accepted cosmological model is the  $\Lambda$ CDM model, in which the Universe is isotropic and homogeneous (i.e. it has no special direction and same properties everywhere), and it is made of ordinary/baryonic matter, neutrinos, photons, cold dark matter (CDM) and dark energy (indicated by the cosmological constant  $\Lambda$ ). In the present-day Universe, dark energy contributes  $\sim 69\%$  of the matter-energy budget, while cold dark matter  $\sim 26\%$ , leaving a small fraction ( $\sim 5\%$ ) of baryonic matter and a negligible contribute ( $< 0.01\%$ ) of neutrinos and photons ([Planck Collaboration et al., 2016](#)). In the  $\Lambda$ CDM model, the first objects to collapse are the smallest dark matter halos, i.e. the result of gravitational collapse of CDM where its density is high enough to locally prevail over the expansion of the Universe, which instead decreases the mean matter density in a fixed volume ([Peebles, 1982](#)). In the early Universe, the typical masses of these halos were small, but they grew with time through merging with other halos and accretion of diffuse dark matter ([Lacey and Cole, 1993](#)). In fact, in CDM cosmology the growth of structure occurs bottom-up: smaller systems virialise first while larger systems form later. On the other hand, a Universe with hot dark matter (HDM) supports a top-down scenario, in which larger objects are more likely to collapse first and smaller structures form later by

fragmentation. This is because low-mass relativistic particles escape rapidly from overdensities not deep enough, therefore the gravitational collapse occurs only in the highest and spatially largest overdensities. However, this scenario is inconsistent with galaxy clustering and cosmic microwave background fluctuations and, on top of that, HDM simulations are not able to reproduce the observed large-scale structure of the Universe, while CDM ones do.

Halo mass functions (HMFs) at different redshifts in a  $\Lambda$ CDM Universe are reported in figure 1.1, left (from [Angrick and Bartelmann 2010](#)) to demonstrate that 1) at fixed redshift, the number density of halos decreases for increasing mass, while 2) at fixed mass, the number density is higher at lower redshift, especially at higher masses. In figure 1.1, right, a schematic representation of the so-called merger tree is shown: as time flows downwards, the progenitor halos/galaxies are on the top of the figure (represented by the thinnest branches of the tree), while the descendants are on the bottom (represented by the trunk of the tree), thus mergers correspond to branch attachments.

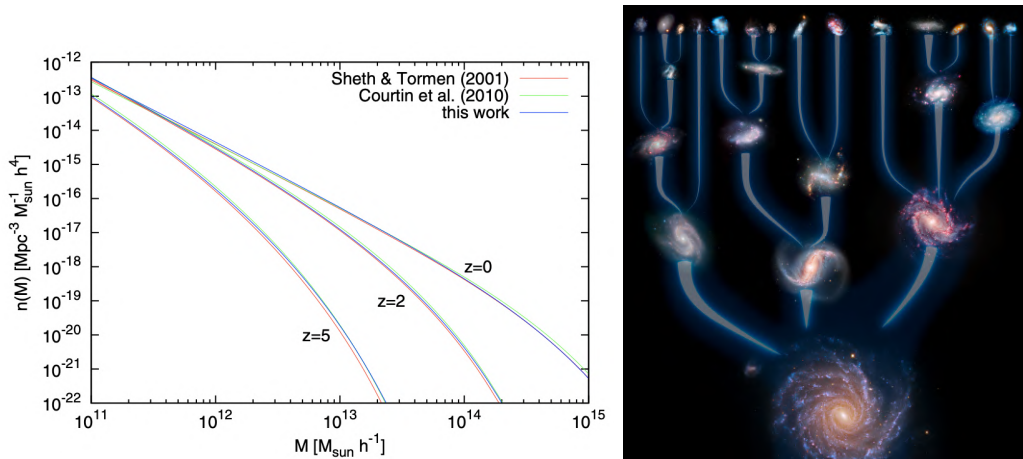


Figure 1.1: Left panel: HMFs at different redshifts (red from [Sheth et al. 2001](#); green from [Courtin et al. 2010](#); blue from [Angrick and Bartelmann 2010](#)). Right panel: representation of the merger tree (Credit: ESO).

During and after the formation of these CDM halos, the gas (i.e. baryonic matter) is believed to follow their gravitational collapse and then to settle into their potential well. Baryonic matter should have the same behavior as

dark matter, growing hierarchically and forming at first smaller galaxies and then (through mergers and accretion of diffuse gas) larger and more massive ones (Kauffmann et al., 1993).

Once the cosmological framework is defined, galaxies can be modelled with two methodologies. The first is based on cosmological hydrodynamic simulations which follow as much as possible self-consistently the evolution of gas, star formation and feedback processes within dark matter halos. These simulations are very time-consuming but capable of investigate sub-galactic scales without covering large volumes of the Universe. The second approach is semi-analytic and is cheaper from the computational point of view, allowing one to simulate large volumes of the Universe up to Gpc scales. However, here the price to pay is that only the global properties of galaxies can be studied, and that the information available is limited by spatial resolution. It should be also noted that while dark matter is relatively “easy” to model, the behaviour of the baryonic component is more uncertain, because of processes that are still not well understood (e.g. feedback processes). These two simulation methods are complementary to each other, as well as theoretical modeling is complementary to direct observations. In fact, since distant galaxies appear to us as they were in the past (as light travels at a finite speed), observations at different redshifts provide information on the past evolution of galaxies. However, studying high-redshift sources is anything but easy for three main reasons:

1. They are faint, so they need long integration times or very deep surveys to be detected;
2. They have small angular sizes, so they need large telescopes with a very high angular resolution;
3. They are redshifted to longer wavelengths, where telescopes have a worse resolution and the sky background could be higher (e.g. 13 mag/ $arcsec^2$  in the K-band).

As the early Universe is populated by small and faint sources, this fascinating scenario is still largely unknown and debated. In this sense, high angular resolution telescopes will have a crucial role in removing the curtains from this topic, since sensitive and defined observations will be needed to firstly detect and secondly obtain spatially resolved images of the elusive sources that inhabit the high-redshift Universe. The angular resolution is an

important factor in astronomical observations as it can provide morphological details that otherwise would be lost with lower resolution telescopes. In fact, observing directly the clumpiness or the shape of a certain source will provide important information and shed light to the phenomena characterizing these unknown epochs, such as intense star formation and interactions between galaxies, and to the nature of these elusive objects. With the current instrumentation we are not able to resolve and characterize high-redshift sources, for which we would need to study the morphology, distinguish mergers from regular disks, resolve star forming regions within galaxies even at early epochs. Therefore, we will need to observe high-redshift galaxies with very high angular resolution and big collecting area telescopes, i.e. large diameter telescopes that work at their diffraction limit (as the new 30-m class of telescopes whose capabilities are discussed in the following chapter).

## 1.2 The Cosmic Star Formation History

### 1.2.1 Star Formation in Galaxies

A powerful tool to understand the formation and evolution of galaxies is the study of the history of their activity across the Universe, i.e., the behaviour with redshift of the star formation rate density (SFRD), discussed in the following section 1.2.2. In general, the Star Formation Rate (SFR) is the rate at which a galaxy turns its gas and dust into stars. The distinctive feature of Star Forming Galaxies (SFGs, or Late-Type Galaxies, LTGs) with respect to Quiescent Galaxies (or Early-Type Galaxies, ETGs) is that they are still forming stars at a non negligible rate ( $0.1 - 10^2 M_{\odot}/yr$ ). In fact, the SFR of a galaxy changes with time and the reconstruction of its past evolution is called Star Formation History (SFH). In the Local Volume (within  $\sim 20$  Mpc distance), the past SFH can be studied using observations of individually resolved stars, allowing one to build the color-magnitude diagram and so reconstruct the SFH in detail. However, at larger distances, thus in most of the cases, stars cannot be observed individually as they are too faint and/or their emission cannot be resolved by a telescope (i.e. the crowding effect). Then, one can collect the entire galaxy emission in different bands and infer its SED. Since the emission in different bands (like UV, optical, IR) is dominated by the contribution of stars of different ages and metallicities, the shape of the SED provides crucial information on the occurred SFH.

This can be derived by comparing the observed SED with state-of-the-art population synthesis models (Bruzual and Charlot, 2003).

One useful method to derive the current/instantaneous SFR is to exploit a variety of indicators based on the luminosity in a particular spectral region of the galaxy that is sensitive to the presence of young stars (see Kennicutt Jr. 1998a):

$$SFR \propto L_{indicator} \quad (1.1)$$

Some of the primary and most common indicators are:

- Recombination lines (like  $H\alpha$ ) from the emission of HII regions (i.e. from gas that is ionized by the UV emission from young massive stars):  $SFR [M_{\odot}/yr] = 7.9 \cdot 10^{-42} L_{H\alpha} [erg/s]$ ;
- Forbidden lines (like [O II] $\lambda$ 3727) from the emission of HII regions:  $SFR [M_{\odot}/yr] = 1.4 \cdot 10^{-41} L_{OI} [erg/s]$ ;
- Monochromatic UV continuum (usually between 1250-2500 Å) from the emission of young (< a few hundreds Myrs) and massive stars:  $SFR [M_{\odot}/yr] = 1.4 \cdot 10^{-28} L_{\nu,UV} [erg/s/Hz]$ ;
- IR luminosity (8-1000  $\mu m$ ), emitted by dust grains that are heated by OB stars:  $SFR [M_{\odot}/yr] = 4.5 \cdot 10^{-44} L_{IR} [erg/s]$ ;
- Radio luminosity (1.4 GHz) from synchrotron radiation emitted in SN Remnants and from free-free emission in HII regions:  $SFR [M_{\odot}/yr] = 5.5 \cdot 10^{-29} L_{1.4GHz} [erg/s/Hz]$ ;
- X-ray luminosity (2-10keV) from high energy emission of massive X-ray binaries:  $SFR [M_{\odot}/yr] = 1.4 \cdot 10^{-40} L_X [erg/s]$ .

The first four relations are taken from Kennicutt Jr. (1998a), while radio and X-ray ones from Vattakunnel et al. (2012).

When both the SFR and the stellar mass  $M_{\star}$  of a galaxy are known, it is possible to estimate the Specific Star Formation Rate (sSFR) defined by the ratio between these two quantities:  $sSFR = SFR/M_{\star}$ . The sSFR is crucial for the study of galaxy formation and evolution since it quantifies the contribution from the ongoing SFR with respect to the stellar mass previously formed in a given galaxy.

The main results of observations at different redshifts and reconstruction of the SFH and sSFR of galaxies are essentially two. The first one is that

SFGs tend to have relatively flat SFHs (i.e. the star formation is roughly constant and less intense), while ETGs seem to have SFHs more peaked (i.e. the star formation occurs in a starburst mode, where the star formation was very intense in relatively short timescales in the past). The second result is the so-called archaeological downsizing, an evolutionary scenario in which massive galaxies evolved earlier and faster than lower-mass ones.

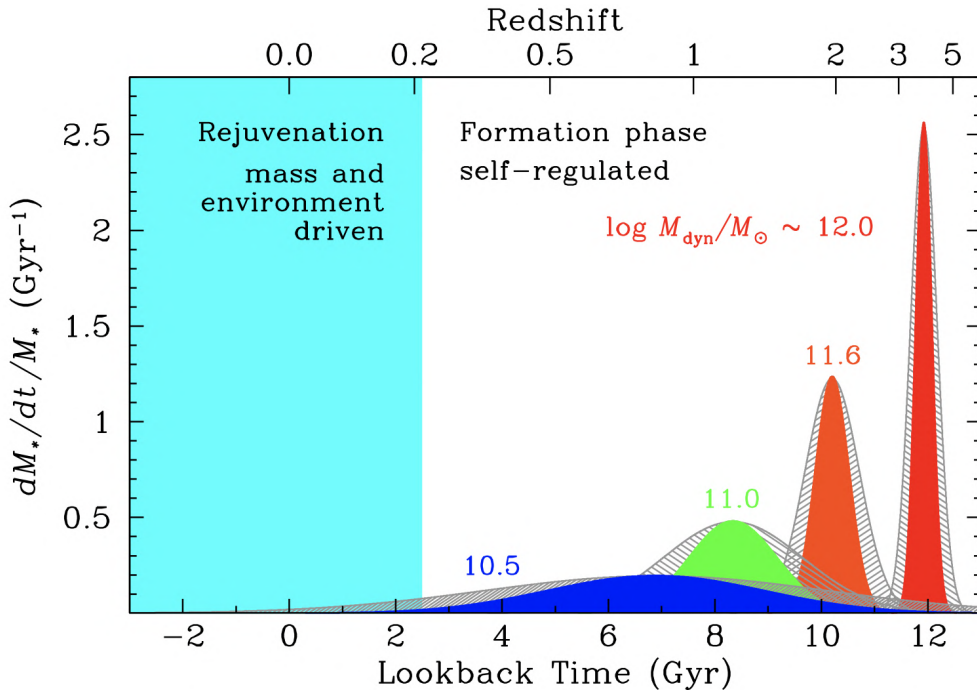


Figure 1.2: Specific star formation rate as function of look-back time (and redshift) for early-type galaxies of various masses as indicated by the labels. The grey hatched curves indicate the range of possible variation in the formation time-scales that are allowed within the intrinsic scatter of the  $[\alpha/\text{Fe}]$  ratios derived in [Thomas et al. \(2010\)](#).

Figure 1.2 illustrates the results from [Thomas et al. \(2010\)](#) based on a sample of local ( $z < 0.06$ ) galaxies from the SDSS. Massive ETGs ( $M_* > 10^{11} M_\odot$ ) formed the bulk of their stars before  $z=2$  and in relatively fast SF episode ( $\tau \sim 0.1 - 0.3$  Gyr): their SFHs are narrow and peaked, therefore their sSFR was high for a short timescale. On the other hand, ETGs with lower masses formed the majority of their stars more recently (i.e. at lower

redshifts) and during a more prolonged time: the peaks of their SFHs are wider. According to this downsizing scenario, where massive ETGs formed most of their stellar mass at high-redshift in a short period of time, powerful starbursts with extremely high SFRs should exist at those redshifts. Indeed, galaxies with these properties (high SFRs and high redshifts) have been identified and could be the progenitors of local quiescent galaxies (see section 1.3).

### 1.2.2 Star Formation Rate Density and Stellar Mass Density

The star formation rate density is a measurement of the average Star Formation Rate (SFR) of the Universe per unit comoving volume at a given cosmic time or redshift. To estimate this quantity (indicated with  $\rho_{SFR}$ ), the first step is to know and integrate the luminosity function ( $\Phi(L)$ , i.e. the function that describes statistically the distribution of galaxy luminosities) obtaining the total luminosity density ( $\rho_L$ ) as follows:

$$\rho_L(z) = \int_0^{\infty} L\Phi(L, z)dL \quad (1.2)$$

Note that the luminosity density  $\rho_L$  can be either bolometric or monochromatic: usually  $\rho_{FUV}$  or  $\rho_{IR}$  are used as in [Madau and Dickinson \(2014\)](#). The second step is to convert  $\rho_L$  ( $erg\ s^{-1}\ Mpc^{-3}$ ) in  $\rho_{SFR}$  ( $M_{\odot}\ yr^{-1}\ Mpc^{-3}$ ) with the relations between SFR and luminosity, discussed in section 1.2.1.

The SFRD is now well understood up to  $z=3$ , when the Universe was 3 Gyr old, thanks to a large number of multi-wavelength studies gathered in the past 30 yr (see [Madau and Dickinson 2014](#), for an exhaustive review) both in the UV ([Wyder et al. 2005](#), [Schiminovich et al. 2005](#), [Dahlen et al. 2007](#), [Reddy and Steidel 2009](#), [Cucciati et al. 2012](#)) and in IR ([Sanders et al. 2003a](#), [Takeuchi et al. 2003](#), [Magnelli et al. 2011](#), [Magnelli et al. 2013](#), [Gruppioni et al. 2013](#)). The obtained results show a rather consistent picture up to  $z\sim 3$  (figure 1.3), where the SFRD rapidly increases from  $z=0$  to  $z=1$ , and then flattens around  $z\sim 2$  (the so-called ‘‘Cosmic Noon’’). A similar evolution is observed for the black hole accretion rate density, a proxy for galactic nuclear activity, peaking at similar redshift ([Madau and Dickinson 2014](#)). The poor and uncertain knowledge of the SFRD evolution at  $z>3$  is mainly due to two limitations:

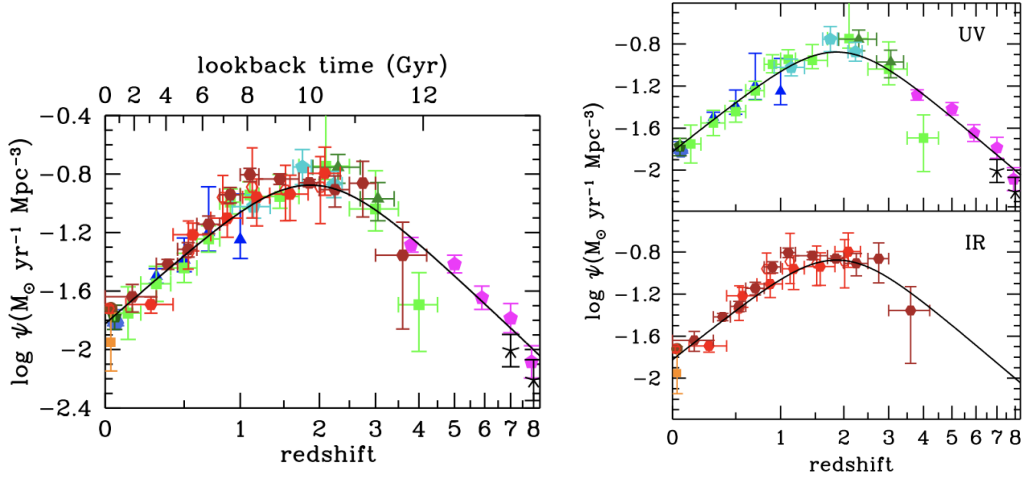


Figure 1.3: The history of cosmic star formation from FUV (top right panel), IR (bottom right panel), and both (left panel) rest-frame measurements (Madau and Dickinson, 2014).

1. At these redshifts, UV surveys are strongly dependent on the assumed dust extinction correction (fig.1.4);
2. IR surveys are not deep enough owing to the sensitivity limits of past and present FIR and sub-mm observatories (bottom right panel in fig.1.3).

Moreover, UV-selected galaxies at  $z > 3$  are known to under-represent the most massive galaxies, which have rich dust content and/or old stellar populations at these cosmic epochs (see following section). This raises the questions of the true abundance of massive galaxies and the star-formation-rate density in the early Universe (Wang et al., 2019). Figure 1.5 shows a more detailed (and recent) estimate for the SFRD from independent multi-wavelength surveys.

Another observable that is crucial to better understand the evolution of the Universe is the behaviour of the stellar mass density with redshift, i.e. the variation of galaxies stellar mass with cosmic time. To compute this, one needs to know the stellar mass function ( $\Phi(M_*)$ , i.e. the function that describes statistically the distribution of galaxy stellar masses) so that,

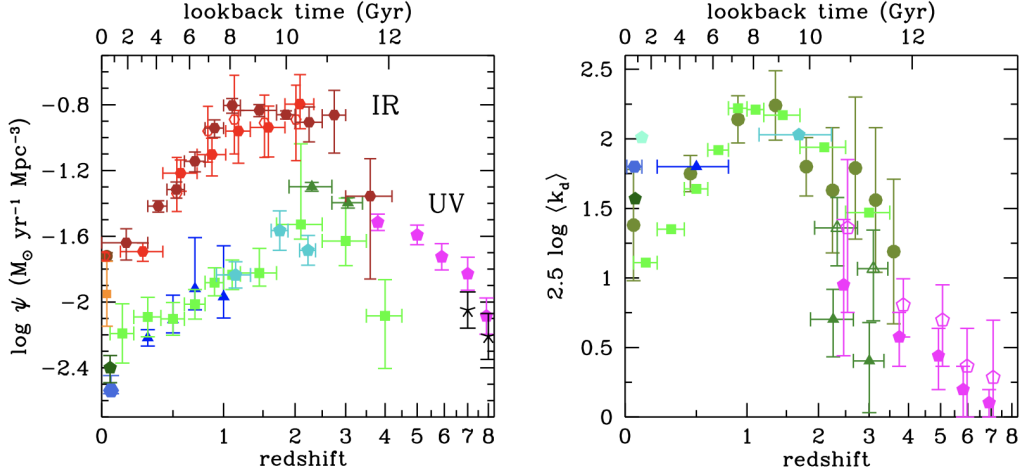


Figure 1.4: Left panel- SFRD obtained in the IR and in the FUV (not corrected for dust attenuation). Right panel- Mean dust attenuation as a function of redshift (Madau and Dickinson, 2014).

following the same approach as eq. 1.2, one has:

$$\rho_{\star}(z) = \int_0^{\infty} M_{\star} \Phi(M_{\star}, z) dM_{\star} \quad (1.3)$$

Figure 1.6 from Davidzon et al. (2017) illustrates the progressive increase of  $\rho_{\star}(z)$  with decreasing redshift, showing how the SMD of the Universe was  $\sim 50\%$ ,  $\sim 10\%$  and  $\sim 1\%$  of its present-day value at  $z \sim 1.3$ ,  $z \sim 2.9$  and  $z \sim 5.7$ , respectively.

A consistency check is provided by the comparison of the observed  $\rho_{\star}$  (expressed in  $M_{\odot} Mpc^{-3}$ ) with that expected from the time integration of  $\rho_{SFR}$  (expressed in  $M_{\odot} yr^{-1} Mpc^{-3}$ ):

$$\rho_{\star,exp}(z) = (1 - R) \int_0^{t(z)} \rho_{SFR}(t'(z)) dt'(z) \quad (1.4)$$

$$\rho_{\star,exp}(z) = (1 - R) \int_z^{\infty} \rho_{SFR}(z') \frac{dz'}{H(z')(1 + z')} \quad (1.5)$$

where  $\rho_{\star,exp}(z)$  is the total mass density of stars at a given  $z$  formed by previous star formation activity,  $H(z) = H_0 \sqrt{\Omega_{m,0}(1+z)^3 + \Omega_{rad,0}(1+z)^4 + \Omega_{\Lambda,0}}$

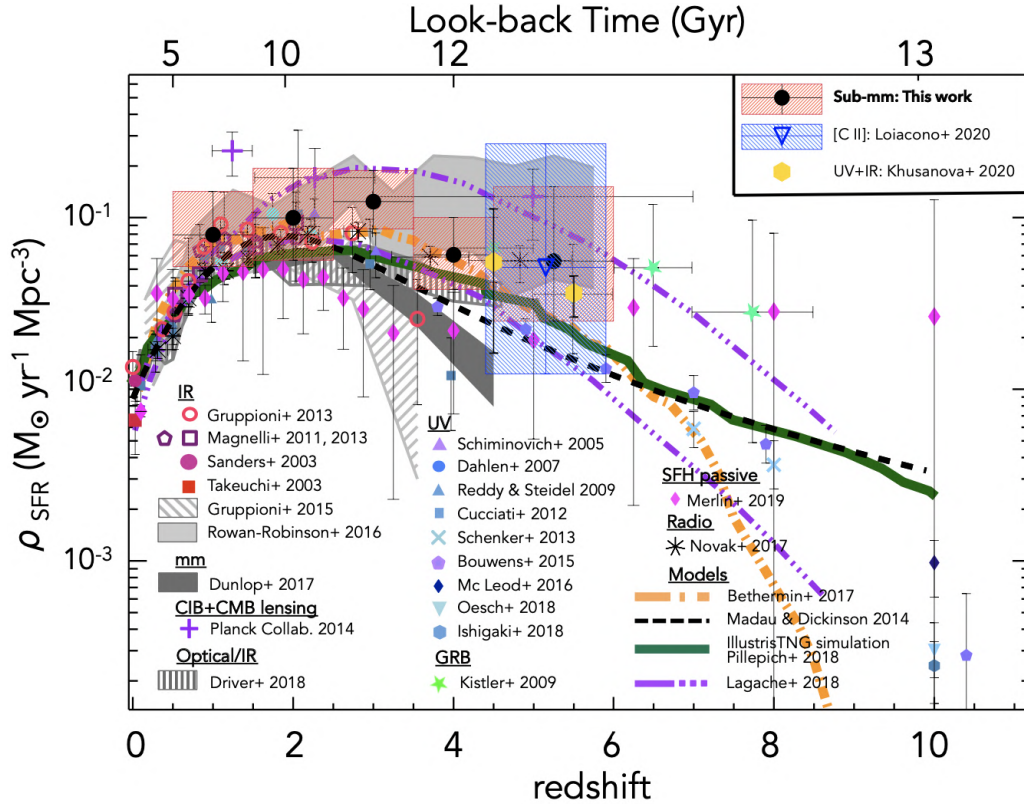


Figure 1.5: SFRD estimated from Gruppioni et al. (2020) and compared with results obtained from surveys in different bands, from the optical/UV to the radio (see references in the legend).

is the Hubble parameter that depends on the chosen cosmology model, and  $R$  is the *return factor* i.e. the fraction of stellar mass returned to the ISM during evolution of a stellar population (due to winds, planetary nebulae, supernovae and so on). In general,  $R \sim 0.3 - 0.4$ , as these values show a good comparison between expected  $\rho_{\star,exp}$  and observed  $\rho_{\star}$  (see figure 1.6); for example, Madau and Dickinson (2014) adopted  $R = 0.27$ .

Finally, it should be noted that both the SFRD and the SMD are strongly dependent on the adopted initial mass function (IMF): the first through the SFR, and the second through the return factor  $R$ , as stars with different masses have different evolutionary scenarios and return different amounts of mass to the interstellar medium. The most used IMFs are the Salpeter (Salpeter, 1955) and the Chabrier (Chabrier, 2003). Other known IMFs are

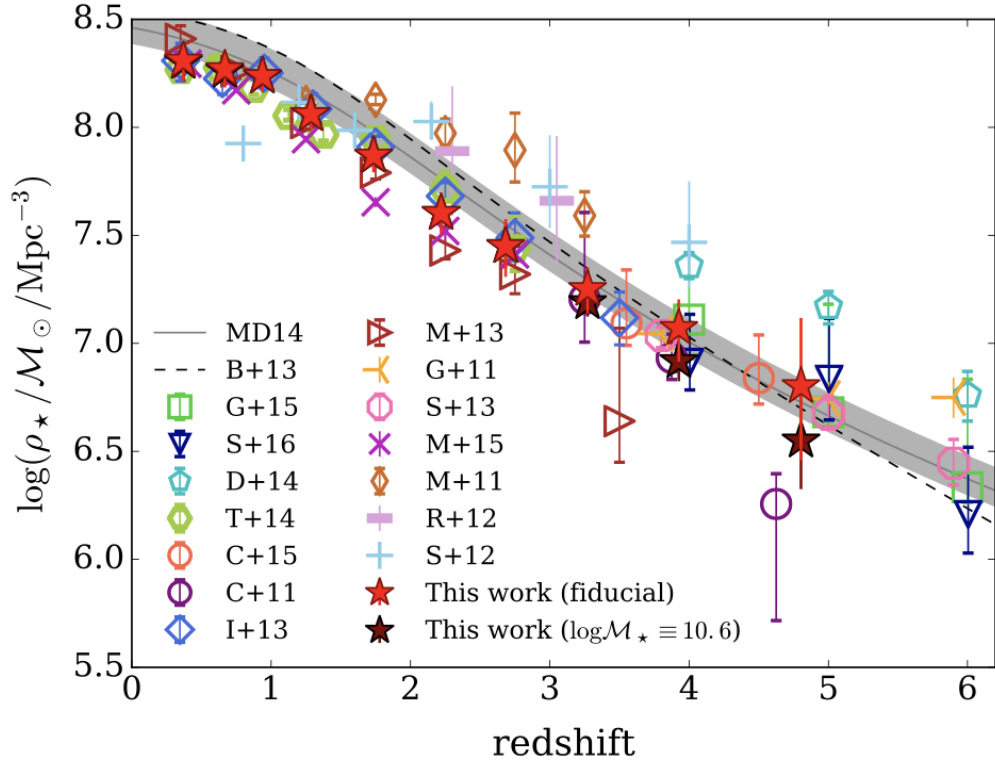


Figure 1.6: Redshift evolution of  $\rho_{\star}(z)$ , as measured in different papers by integration of the SMF. The grey shaded area reports the  $\rho_{\star,exp}(z)$  range calculated from Madau and Dickinson (2014) and enclosed by  $R=0.25$  and  $R=0.50$ . Figure from Davidzon et al. (2017).

the Miller-Scalo (Miller and Scalo, 1979) and the Kroupa (Kroupa, 2001).

### 1.3 Dusty Star-Forming Galaxies at High Redshift

In the previous sections we mentioned that a population of powerful starbursts with extremely high SFRs should exist at high redshifts, likely being the progenitors of local ETGs and contributing significantly to the SFRD and SMD. However, any discussion of the high-redshift infrared-bright galaxy population requires a brief overview of the local Luminous Infrared Galaxies

(LIRGs;  $L_{IR} > 10^{11} L_{\odot}$ ) population, first discovered by the Infrared Astronomy Satellite (IRAS) back in 1983. The majority of local IRAS-selected galaxies were starburst galaxies with  $SFR > 10^2 M_{\odot}/yr$  (for comparison, the Milky Way produces  $\sim 2 M_{\odot}/yr$ , [Robitaille and Whitney 2010](#); [Chomiuk and Povich 2011](#)), and infrared luminosities within  $10^{11} L_{\odot} < L_{IR} < 10^{12} L_{\odot}$  (LIRG), while a small subset were Ultraluminous Infrared Galaxies (ULIRGs) with  $10^{12} L_{\odot} < L_{IR} < 10^{13} L_{\odot}$ . Observational evidence that high infrared luminosities are correlated not only with high SFRs but also with major *wet* mergers led to the widely accepted evolutionary scenario first proposed by [Sanders et al. \(1988\)](#) for this type of sources. A schematic diagram of this evolutionary picture is shown in figure 1.7.

This formulation places the LIRG or ULIRG phenomenon at a fixed stage in a larger evolutionary sequence where two gas-rich galaxies collide and trigger an intense phase of star formation by the rapid compression and cooling of gas. This collision and subsequent star formation cause the prolific formation of dust particles which, in turn, absorb rest-frame optical and ultraviolet emission from young massive stars and re-radiate thermally that light at infrared/submillimeter wavelengths. Significant theoretical progress and numerical simulations toward this picture has been made during the past 20 years, proving that major mergers of gas-rich disk galaxies can actually account for these phenomena (see [Hopkins et al. 2008](#) for a review).

Far-infrared and sub-millimeter surveys have in this sense established the important role of dusty, star-forming galaxies (DSFGs) in the assembly of stellar mass and evolution of galaxies in the Universe. Major advances in far-infrared instrumentation in the past decades, both space-based and ground-based, such as the Infrared Space Observatory (ISO), the Submillimetre Common-User Bolometer Array (SCUBA) of the James Clerk Maxwell Telescope (JCMT), the Spitzer and Herschel satellites, or the Atacama Large Millimetre/submillimetre Array (ALMA) have led to the detection of nearly a million DSFGs ([Casey et al. 2014](#); [Swinbank et al. 2014](#)).

The discovery of a large amount of sub-mm and infrared emitting galaxies at high-redshift (Sub-Millimeter Galaxies, SMGs) has proven to be a significant challenge for theoretical models of galaxy formation and evolution. The existence of a numerous population of massive galaxies already in place or even evolving passively at  $z > 2-3$ , and even up to  $z \sim 6$  (back to just  $\sim 800-900$  Myr after the Big Bang), is very difficult to reproduce by state-of-the-art cosmological simulations and models (see a recent discussion by [Lovell et al. 2022](#)). Whether or not they are simply scaled-up versions of local LIRGs,

observations confirmed that SMGs have comparable (or even higher) masses, SFRs and luminosities to local LIRGs, but crucially demonstrated that the space density of this type of galaxies at  $z \sim 2$  is  $\sim 1000\times$  higher than at  $z=0$ . For this latter reason, while LIRGs contribute  $\ll 1\%$  of the volume average SFR density at  $z = 0$ , SMGs may contribute up to half of the SFR density at  $z \sim 2$  (Simpson et al., 2014). However, it is not clear if these extreme galaxies are representative of the whole situation at high redshift. Along with the flux dimming at increasing redshift, it needs to be considered also that IR and sub-mm telescopes have a worse angular resolution (at a given diameter) and sensitivity than optical ones, so it is more challenging to observe smaller and fainter sources. These two effects limit our observations and surveys to the bright end of a much larger population of obscured galaxies at high redshifts, which are extremely challenging to detect with the current FIR/sub-mm instrumentation.

Finally, the same evolutionary scenario presented early in this section suggests that this starburst SMG phase may be followed by a dust-enshrouded active galactic nucleus (AGN) phase, eventually becoming an optically bright Quasar before turning into a passive/quiescent galaxy: SMGs could be the progenitors of local elliptical galaxies.

## 1.4 HST-dark Galaxies

The advent of ALMA has revolutionized our view on sub-mm/mm wavelengths, enabling astronomers to capture sources much fainter than before. In particular, ALMA blind surveys at high redshift performed in the last few years (Dunlop et al. 2017; Walter et al. 2016; Aravena et al. 2016; Hatsukade et al. 2018; Franco et al. 2018; Yamaguchi et al. 2019; Gruppioni et al. 2020; Gómez-Guijarro et al. 2022) discovered, among classical SMGs, a population of galaxies invisible at optical (and often also NIR) wavelengths, undetected even in the deepest HST images (for this reason called *HST-dark galaxies*) but identified with faint counterparts in Spitzer IRAC (figure 1.8). These objects have been selected in different ways (Enia et al. 2022): serendipitously in deep CO line scan surveys (Williams et al. 2019), in SCUBA surveys (Riechers et al. 2020), via their extreme near-IR color (Wang et al. 2016, Wang et al. 2019), and in continuum far-IR (ALMA surveys nominated early) and radio (Talia et al., 2021) surveys.

Indeed, it was over two decades ago that Dey et al. (1999) first hypoth-

esized the existence of a faint high-redshift population of galaxies that can be missed from the deepest optical surveys. Furthermore, even before the advent of ALMA, there were cases of bright SMGs without an optical/NIR counterpart, such as GOODS 850-5 (also known as GN10, Wang et al. 2009).

Recently, this particular type of galaxies were analysed also with the cutting-edge James Webb Space Telescope (JWST, launched at the end of 2021) by Pérez-González et al. (2022), finding HST-dark galaxies not visible even in the F150W NIRCcam band of JWST.

These results indicate the existence of a prominent population of dusty star-forming galaxies at  $z > 3-4$ , which is fainter than the confusion limit of the single-dish sub-mm surveys that discovered SMGs, but has much larger space densities, providing a significant contribution to the SFRD at high- $z$  (ten times larger than that of equivalently massive ultraviolet-bright galaxies at  $z > 3$ , Wang et al. 2019). It is crystal clear now that HST-dark galaxies have a crucial role not only in improving our knowledge on the formation and evolution of galaxies, but also in obtaining an almost complete estimate of the total SFRD and SMD.

## 1.5 Thesis Goals

As previously stated, a population of massive and dusty sources that are missed from the deepest optical/NIR surveys have recently been discovered in the early Universe. These galaxies are likely to play a crucial role for our understanding of the scenario of formation and evolution of galaxies.

Very little is known about their nature and morphology. Indeed, high resolution and very sensitive observations will be needed to obtain accurate and spatially resolved images of these elusive galaxies. Will they be compact, or clumpy? Will they be disk-like or show merging signatures? How will the stars and the star forming regions distribute within the ISM and dusty clouds? All these questions could be answered only by observing them with a very high angular resolution and a very big collecting area telescope. In this regard, the ESO's Extremely Large Telescope (ELT), that will be the largest optical/NIR telescope ever built and will have unprecedented sensitivity and resolution, will be able to revolutionize our view of the Universe. Indeed, ESO's ELT (Chapter 2) is a giant telescope under construction in Chile that, with its 39m primary mirror and advanced adaptive optics systems, aims at observing the faintest and most distant objects in the Universe at the diffraction limit.

With the combination of its NIR wide-field camera MICADO (section 2.3) and its last-generation adaptive optics system MORFEO (section 2.4), ELT will be capable of delivering NIR images and spectra at an unprecedented angular resolution. Predictions for these revolutionary outputs can be generated using a simulator specifically created for MICADO, called SIMCADO (Chapter 3), which produces synthetic images with the same properties as those that will be obtained by MORFEO+MICADO@ELT.

The purpose of this thesis is to simulate with SIMCADO -and so predict-how HST-dark galaxies would be observed by the ELT, based on the information provided by ALMA (such as their best-fit SEDs and redshifts). This will probe the capabilities of high-resolution telescopes in revolutionize our view of high-redshift galaxies, enabling us to observe details so far inaccessible with current telescopes.

This work is organized as follows:

- Chapter 2: introduction to ELT's properties and capabilities;
- Chapter 3: simulations with SIMCADO of local LIRGs and HST-dark galaxies;
- Chapter 4: simulation results;
- Chapter 5: final discussion and conclusions.

Throughout this project, we assume a flat cosmology with  $\Omega_M = 0.286$ ,  $\Omega_\Lambda = 0.714$  and a Hubble constant  $H_0 = 69.6 \text{ km s}^{-1} \text{ Mpc}^{-1}$  from Wright (2006). All magnitudes are in the AB photometric system (Oke and Gunn, 1983).

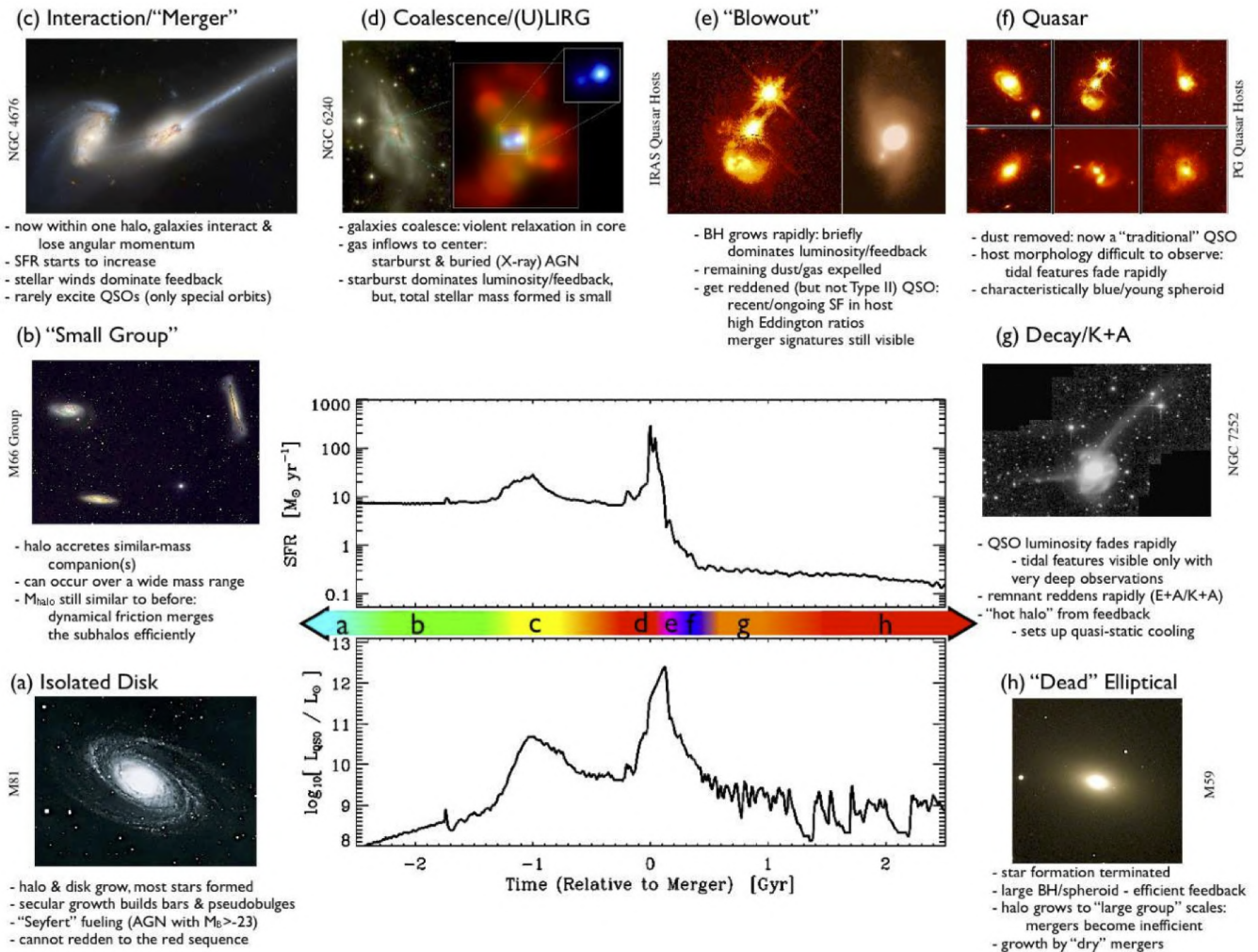


Figure 1.7: Schematic outline of the phases of growth in a typical galaxy undergoing a gas-rich major merger. Figure reproduced from Hopkins et al. (2008).

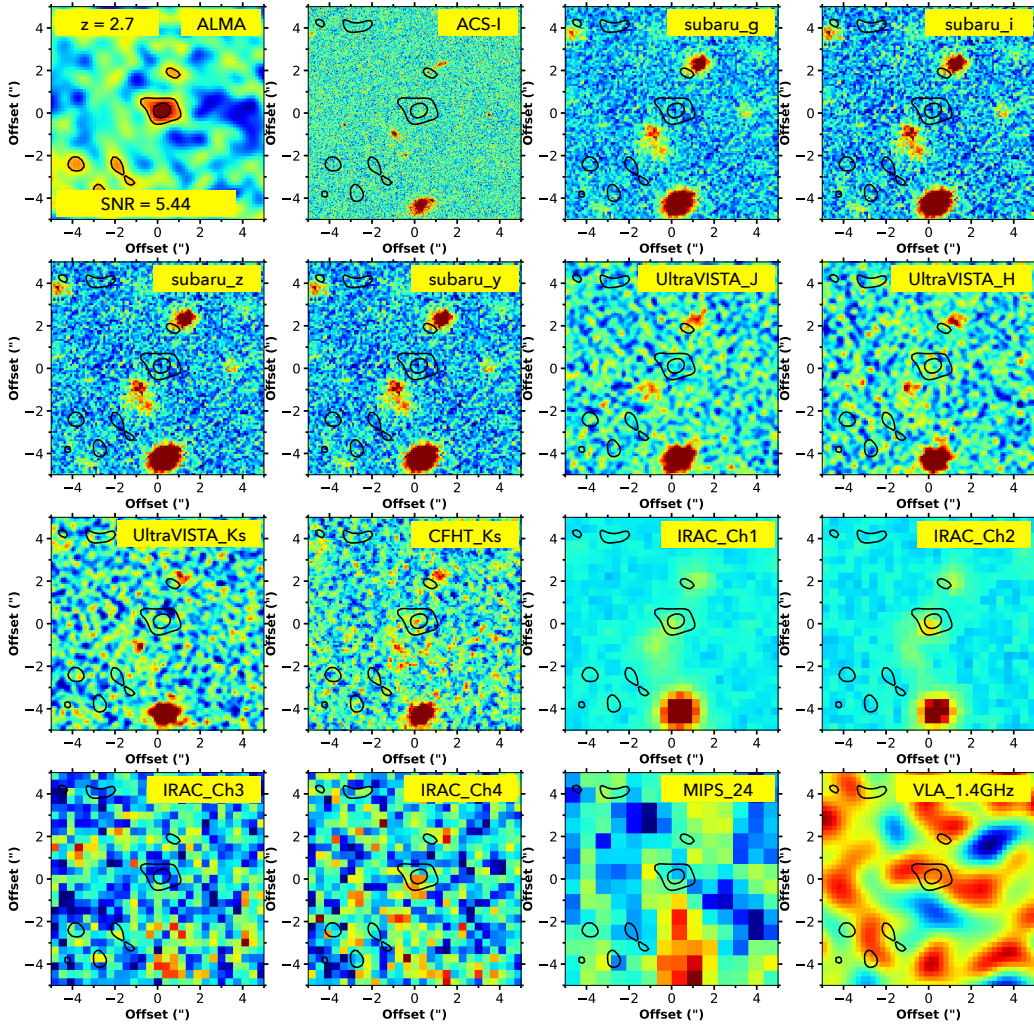


Figure 1.8: Optically/NIR dark galaxy detected only with IRAC. The plotted contour levels are at  $3$  and  $5 \sigma$  from ALMA detection, corresponding to  $0.14$ ,  $0.23$  mJy, superimposed to the ALMA, HST/ACS-I, Subaru, UltraVISTA, IRAC, MIPS, and radio VLA-1.4 GHz images (Gruppioni et al., 2020).

## Chapter 2

# ESO's ELT: The World's Biggest Eye on the Sky

Extremely large telescopes will lead a leap forward in astrophysical knowledge, allowing a deeper exploration of our Universe, and giving sharper views of cosmic objects than ever before. In the near future, 30-m class telescopes will open a new window on the sky, as the extreme spatial resolution offered by these telescopes will be unprecedented, and with the help of adaptive optics they will reach their diffraction limit from the ground.

The European Southern Observatory (ESO) is currently building the largest telescope ever built. ESO's Extremely Large Telescope (ELT) is a revolutionary ground-based telescope that will have a 39-metre primary mirror and will be the largest telescope in the world in the optical and near-infrared (near-IR) wavelength range: the world's biggest eye on the sky. With its huge primary mirror and intrinsic adaptive optics systems, ELT aims at observing the faintest and most distant objects in the Universe at the diffraction limit, covering a wide range of scientific possibilities.

We recall that the size of a telescope is important for two main reasons: 1) the amount of light it can collect and 2) the level of detail it can see. As a 39-metre telescope, the ELT will gather 15 times ( $39^2/10^2 \sim 15$ ) more light than the largest optical telescopes operating today ( $\sim 10$  m) such as the Gran Telescopio Canarias on La Palma, in the Canary Islands (10.4 m, [Espinosa and Alvarez Martin 1997](#)), the two Keck telescopes on Mauna Kea, in the Hawaii Islands (10 m, [Nelson 1990](#)), the Large Binocular Telescope in Arizona (8.4 m, [Hill and Salinari 1998](#)) or the ESO's Very Large Telescope on Cerro Paranal, about 20 kilometres from the site of ELT itself (8.2 m). In fact, at

fixed wavelength, the angular resolution of a telescope is set by its diameter, so that the ELT (39 m) will provide images  $\sim 15$  times sharper than those from the Hubble Space Telescope (2.4 m), as well as  $\sim 5$  times sharper than VLT ones (8.2 m). For example one can have a more quantitative approach comparing the performances of both ELT and HST in the I-band (800 nm), obtaining that:

$$\theta_{HST} \sim \frac{\lambda}{D} = \frac{800 \text{ nm}}{2.4 \text{ m}} = 0.069 \text{ arcsec} \quad (2.1)$$

$$\theta_{ELT} \sim \frac{\lambda}{D} = \frac{800 \text{ nm}}{39 \text{ m}} = 0.004 \text{ arcsec} \quad (2.2)$$

In infrared bands as well, a 39-m telescope like ELT offers a resolution about six times better than the one obtained by the cutting-edge James Webb Space Telescope (JWST) launched in December 2021 and now in full operations. Again, one can achieve a quantitative approach comparing the resolving capabilities of the two revolutionary telescopes, in Ks-band (2200 nm) for example:

$$\theta_{JWST} \sim \frac{\lambda}{D} = \frac{2200 \text{ nm}}{6.5 \text{ m}} = 0.070 \text{ arcsec} \quad (2.3)$$

$$\theta_{ELT} \sim \frac{\lambda}{D} = \frac{2200 \text{ nm}}{39 \text{ m}} = 0.012 \text{ arcsec} \quad (2.4)$$

Indeed, the fraction  $\lambda/D$  (where  $\lambda$  is the wavelength of observation and  $D$  is the telescope diameter) sets the diffraction limit (DL) of a certain instrument, which holds under ideal conditions such as above the atmosphere where there is no turbulence. On the other hand, under the atmosphere our observations have worse resolution than the diffraction limit because of distortions introduced by the turbulence, and become seeing-limited. Nevertheless, the resolving power can be drastically improved thanks to adaptive optics systems, like MORFEO (Multiconjugate adaptive Optic Relay For ELT Observations, whose performances will be extensively discussed in this thesis), allowing to reach the diffraction limit from the ground.

Besides, the astrometric accuracy of ELT, with its high-resolution imager MICADO (section 2.3), is predicted to be better than  $50 \mu\text{as}$  down to a magnitude of  $H \sim 20$  mag, thus comparable to the Gaia astrometric precision at  $G \sim 15$  (where  $G$  is the magnitude in the Gaia passband, [Lindegren et al. 2021](#)) in uncrowded stellar region ([Fiorentino et al., 2020](#)).

The past decade has brought unprecedented astronomical revelations, such as the discover of an enormous amount of exoplanets (Howell, 2020) or the construction of the first image of a black hole (Collaboration, 2019). Therefore in the next epoch, giant telescopes such as the ELT will shed light on some of the most important scientific challenges of our time, listed briefly in section 2.5.

The ELT programme was approved in 2012 and the green light for construction at Cerro Armazones ( $\sim 3000$  m) in Chile’s Atacama Desert was given at the end of 2014. ESO has been working alongside a worldwide community and dozens of Europe’s most cutting-edge companies to bring the telescope to its “technical first light” later this decade. The construction cost of the full baseline is estimated to be around 1.3 billion euros.

## 2.1 ELT Design and Mirrors

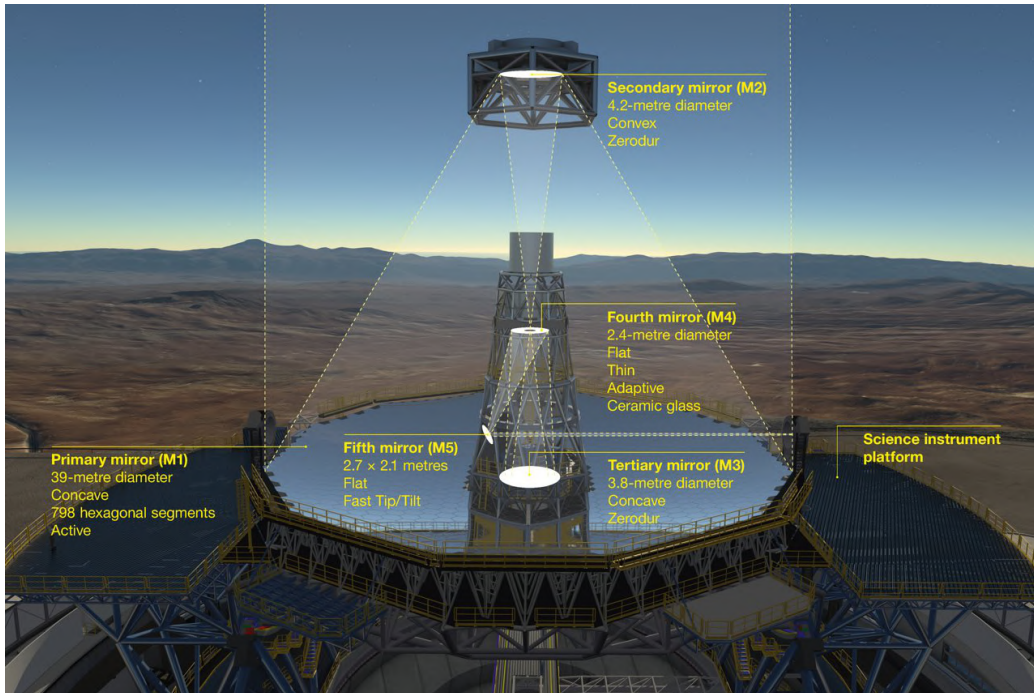


Figure 2.1: Diagram that shows the 5-mirror optical system and the light path of ESO’s ELT. Credits: ESO

The ELT will have a five-mirror optical design showed in figure 2.1. The mirrors all have different shapes, sizes and roles but will work together seamlessly:

- M1 Mirror;

The M1 is one of the most impressive and challenging aspects of the entire ELT project. Too large to be made from a single piece of glass, the 39 m diameter mirror has a radius of curvature of 68.7 m and consists in a set of 931 hexagonal segments, 798 of which will be on the telescope anytime whereas 133 will be spare segments. The segments are about 5 cm thick, measuring 1.45 m across and have a gap between them of 4 mm (figure 2.2). On top of that, to adjust its position and maintain the perfect co-alignment of all the segments, each side of each segment has two sensors that constantly measure the gap with the adjacent one (to nm accuracy) and provide the necessary information to activate the positioning actuators (PACTs) able to move and adjust the position of every segment. Therefore, since the system has to work together as a single mirror, M1 require almost 2500 PACTs and  $\sim 9000$  edge sensors. Keeping this infrastructure working is extremely challenging, as the full structure will move during an observation (being affected by wind and thermal changes), and has to support the total M1 weight (each mirror segment weights 250 kg). To achieve the required scientific performance, the mirror needs to be maintained in position and with no surface irregularity greater than about 8 nm across its entire diameter.

- M2 and M3 Mirrors;

Contrary to most famous telescopes (such as VLT or HST) that use just two curved mirrors to form an image, the ELT has three mirrors: the light collected by M1 will be reflected by its secondary mirror (M2) and then to the tertiary mirror M3 (as seen in fig.2.1). The M2 mirror (fig.2.3-left) will be the largest optical secondary mirror ever used, having a diameter of 4.25 m. It is  $\sim 10$  cm thick, with an 80 cm central hole, and has a radius of curvature of  $\sim 8.8$  m. As seen in fig.2.1, M2 will hang over the M1 mirror about 60 m above the ground, hosted in its dedicated cell but anchored to the telescope main structure. While M2 is convex mirror, the M3 mirror (fig.2.3-right) is a concave mirror with a radius of curvature of  $\sim 21$  m, with a similar diameter of 4 m. It is  $\sim 10$  cm thick, with a 3 cm central hole and it will be also hosted in

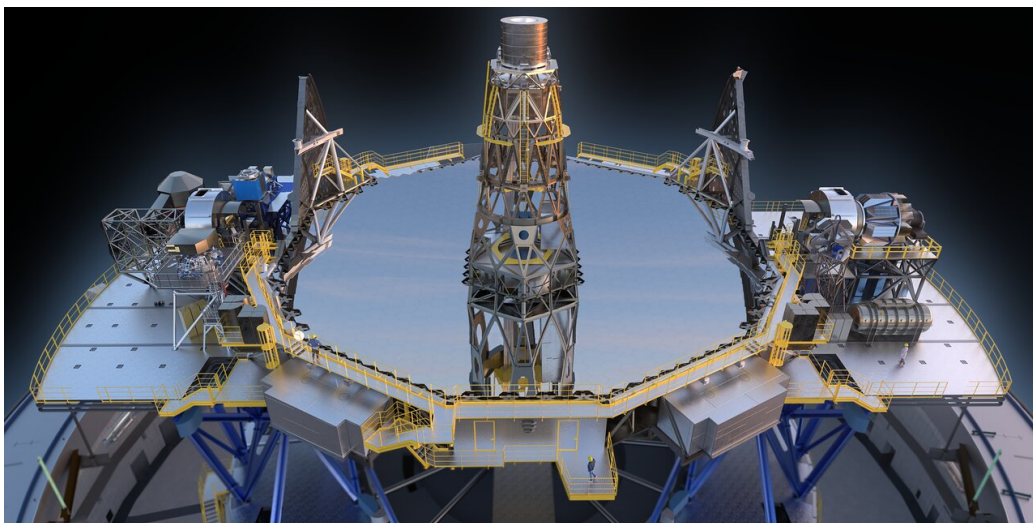


Figure 2.2: Artist's impression of the main mirror M1 of the ELT. Credit: ESO.

its dedicated cell, like M2. Finally, the mirrors alone weigh more than 3 tonnes each and, with cell and structure included, the overall weight of each assembly is about 12 tonnes.

- M4 Mirror;  
The ELT's adaptive optics is mainly based on two corrective surfaces, a tilting mirror (M5, fig.2.4-right) and a high-order adaptive mirror (M4, fig.2.4-left). M4 is the main adaptive mirror of the ELT and all of its instruments. It will be the largest deformable mirror ever built, in fact its surface can be distorted and adapted to correct for atmospheric turbulence, as well as for the vibrations of the telescope structure induced by its motion and the wind. This is achieved thanks to a thin shell levitating only  $90 \mu\text{m}$  away from the mirror's surface, which acts like a membrane that deforms -under the effect of  $\sim 5300$  contactless magnetic actuators- up to 1000 times per second and with an accuracy of a few tens of nm. M4 will measure 2.4 m in diameter and will be made up of six  $60^\circ$  petal sections, each only 1.95 mm thick and with a thickness uniformity better than  $15 \mu\text{m}$ .
- M5 Mirror.  
M5 will be a flat and elliptical mirror measuring 2.7 by 2.2 m, there-

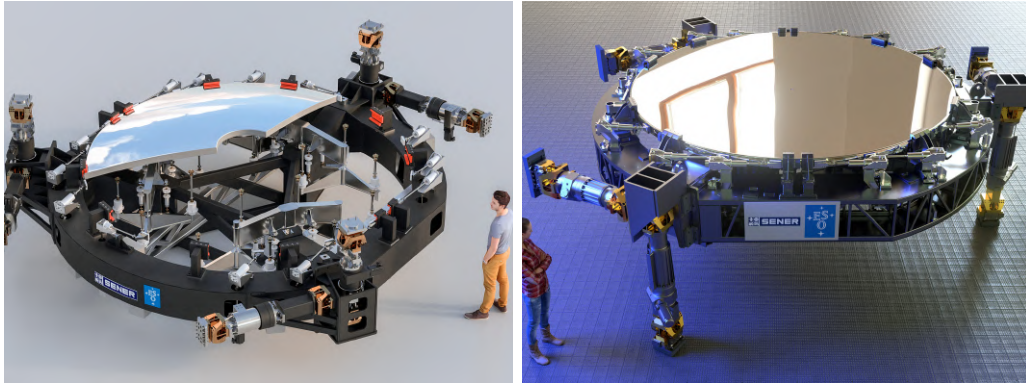


Figure 2.3: Artist's impression of the M2 (left) and M3 (right) mirrors that will be used on ELT. Credit: ESO/SENTER.

fore the largest tip-tilt mirror ever employed in a telescope. In fact the cell in which M5 is hosted includes a fast tip-tilt system for image stabilisation that will compensate perturbations caused by the telescope mechanisms, wind vibrations, atmospheric turbulence, by adjusting the mirror's tip and tilt angles to a few tens *mas* ( $1 \text{ mas} = 10^{-3} \text{ arcsec}$ ) accuracy. When complete, M5 will be constructed from six lightweight silicon-carbide segments brazed together, in order to achieve both lightness and stiffness.

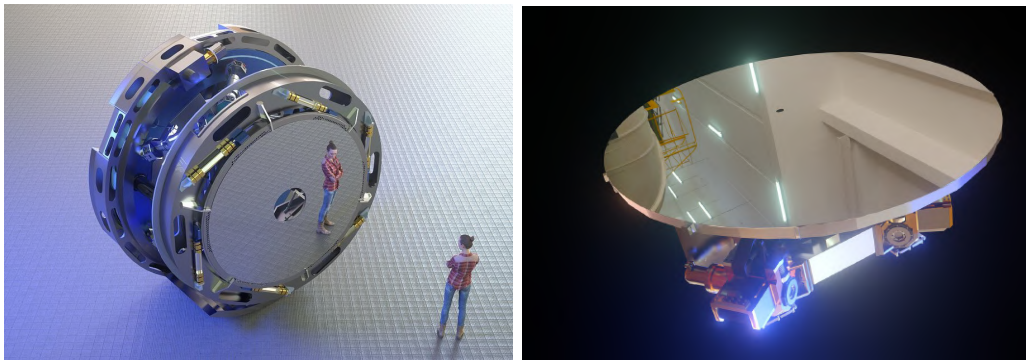


Figure 2.4: Artist's impression of the M4 (left) and M5 (right) mirrors that will be used on ELT. Credit: ESO.

## 2.2 ELT Instruments

After the ELT's mirrors have collected and corrected the light from astronomical objects, it is up to the instruments to analyse it. The suite of instruments planned for the ELT includes cameras, spectrographs and other important "tools". Four of the instruments (HARMONI, MICADO, MORFEO, METIS) will start to operate at ELT technical first light, while additional two instruments (ANDES and MOSAIC) will start operations at a later stage. The next two chapters are entirely spent on discussing MICADO and MORFEO capabilities, since they are integral parts of this thesis and of crucial importance regarding the topics covered along with it. Therefore, for now we will focus briefly on the other four instruments:

- HARMONI (High Angular Resolution Monolithic Optical and Near-infrared Integral field spectrograph) will be one of the first generation ELT instruments. Its 3D spectrograph's core capability is near-IR (0.82-2.45  $\mu m$ ) integral field spectroscopy over a wide range of resolving powers ( $R = \lambda/\delta\lambda = 3500$  to 17000). It also offers a variety of plate scales (60 $\times$ 30, 20 $\times$ 20, 10 $\times$ 10, and 4 $\times$ 4 *mas*) with their corresponding FoV (9"  $\times$  12", 3"  $\times$  4", 1.5"  $\times$  2", 0.6"  $\times$  0.8", respectively). It will enable astronomers to study many different astronomical targets, from distant galaxies to individual stars in nearby galaxies and exoplanets in the Milky Way.
- METIS (Mid-infrared ELT Imager and Spectrograph) is a spectrograph and high-contrast imager. The three fundamental observing functionalities of METIS will be: 1) imaging at L/M bands (3–5  $\mu m$ ) with medium spectral resolution ( $R \sim 1400$ ) slit spectroscopy; 2) imaging at N band (7.5–13.5  $\mu m$ ) with low resolution ( $R \sim 400$ ) slit spectroscopy; and 3) high resolution ( $R \sim 100.000$ ) IFU spectroscopy at L/M bands, including a mode with extended instantaneous wavelength coverage. On top of that, the two imaging modes also present a coronagraphy for high contrast imaging, for this reason METIS is expected to make large contributions in the exoplanets field, as well as in Solar System objects, circumstellar discs and star forming regions, properties of brown dwarfs, the centre of the Milky Way, the environment of evolved stars, and active galactic nuclei.

- ANDES (ArmazoNes high Dispersion Echelle Spectrograph), formerly known as HIRES, is a powerful spectrograph that covers the optical and NIR spectral ranges simultaneously. It consists of three echelle spectrographs VIS-BLUE (UBV bands), VIS-RED (RIZ bands) and NIR (YJH bands), providing a simultaneous wavelength coverage of 0.4-1.8  $\mu m$  at a  $R = 100,000$ . Besides, ANDES will also have an IFU mode fed by the Single-Conjugate Adaptive Optics (SCAO, discussed in the following section) module to correct for the effect of turbulence in the atmosphere. It will be used to search for signs of life in Earth-like exoplanets, find the first stars born in the Universe, test for possible variations of the fundamental constants of physics, and measure the acceleration of the Universe's expansion.
- MOSAIC is a versatile Multi-Object Spectrograph that can measure the light from many different sources at the same time. It will be composed of an highly-multiplexed visible and near-infrared spectrograph targeting numerous unresolved objects (High Multiplex Modes; HMM-VIS and HMM-NIR) with a mode featuring a more modest multiplex which is, however, able to spatially resolve extended sources (multi-IFU modes). The three instrument modes (HMM-VIS, HMM-NIR, and multi-IFU) operate between 0.45 and 1.8  $\mu m$  at  $R = 4000$  with selected high resolution settings in the VIS ( $R > 18000$  in two bands) and the NIR ( $R > 9000$  or  $R > 18000$  depending on the chosen band). MOSAIC will use the widest field of view provided by ELT (40  $arcmin^2$ ) to conduct the first exhaustive inventory of matter in the early Universe. This will be crucial to show how matter is distributed in and among galaxies, improving our understanding of their formation and evolution scenario.

## 2.3 MICADO

MICADO (Multi-AO Imaging CAmera for Deep Observations) will be the near-infrared (NIR) wide-field camera available on the E-ELT at first-light. Offering large filter wheels which are able to hold more than 30 narrow and broad filters (e.g. IJHK broad filters, in figure 2.5), MICADO is designed to work between 0.8 and 2.4  $\mu m$  with the assistance of a single or multi-conjugate adaptive optics system (following section) at the diffraction limit

of the ELT. In imaging mode it will provide a wide field option, where the field of view will be  $50.4 \times 50.4 \text{ arcsec}^2$  with a pixel scale of  $4 \text{ mas}$ , and a higher-resolution zoom mode with a  $1.5 \text{ mas}$  pixel scale over a  $18.9 \times 18.9 \text{ arcsec}^2$  FoV. MICADO will also have similar sensitivity to JWST and 6 times better resolution, as discussed early on this chapter (eq. 2.3 and 2.4).

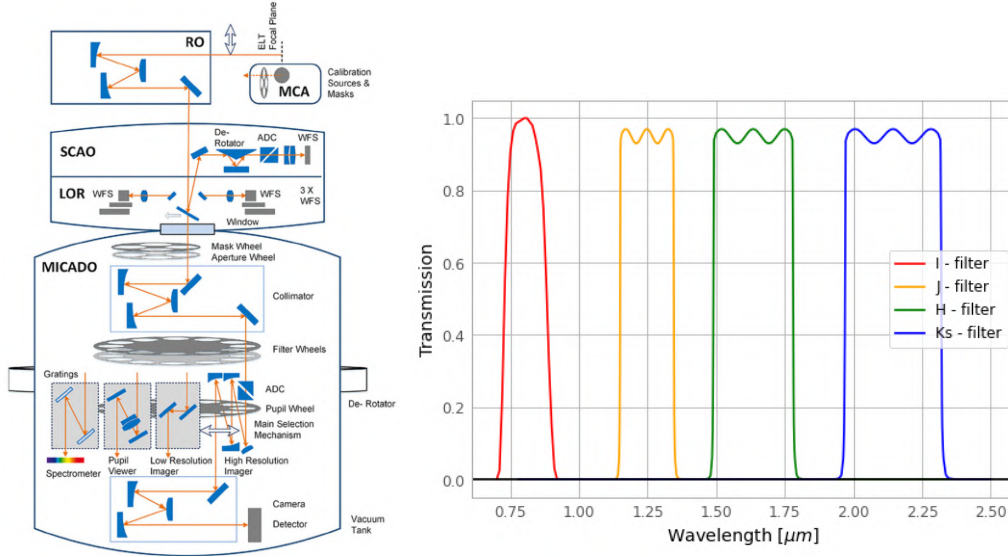


Figure 2.5: Left: Details of MICADO. Credit: ESO/MICADO consortium; Right: The main optical/infrared filters of MICADO.

The design of MICADO was driven by a desire for high sensitivity, resolution, astrometric accuracy (from  $10 \mu\text{as}$  to  $50 \mu\text{as}$  over the full field of view), high-contrast imaging (with the possibility of using a coronagraph like other instruments) and wide wavelength coverage spectroscopy. In particular, the whole bandpass is covered using a short ( $3''$ ) slit in the  $0.84\text{--}1.48 \mu\text{m}$  wavelength range, and a long ( $15''$ ) slit at  $1.48\text{--}2.46 \mu\text{m}$  (and also  $1.16\text{--}1.35 \mu\text{m}$ ) that allow extraction of the off-axis sky background (Davies et al. 2016, Davies et al. 2018). The slit width is  $\sim 16 \text{ mas}$  and the spectral resolution  $R$  is between 10.000 and 20.000.

The image of the astronomical field being observed will be formed on a  $3 \times 3$  array of near-infrared sensitive detectors (fig. 2.6). Each of the nine state-of-the-art detectors will have  $4096 \times 4096$  pixels, with each pixel  $15 \mu\text{m} \times 15 \mu\text{m}$  in size.

Finally, another engineering challenge is that since MICADO is designed

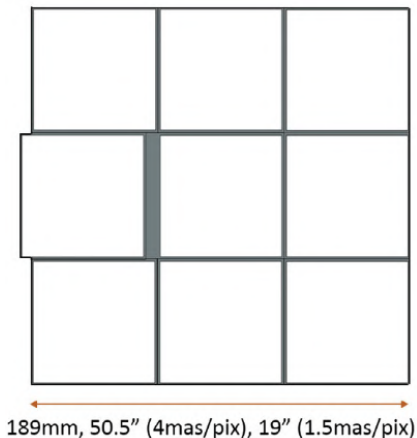


Figure 2.6: The layout of the 9 MICADO detectors, with the gaps shown in grey. In the imaging layout, the 50.4" field of view is standard mode, and the 18.9" is the zoom mode.

to observe near-infrared wavelengths, the instrument needs to be housed in a cryostat and cooled to 80 K using liquid nitrogen. The instrument is designed and built by a consortium of institutes in Germany, France, Netherlands, Austria, and Italy.

## 2.4 MORFEO

MORFEO (Multiconjugate adaptive Optic Relay For ELT Observations, formerly known as MAORY) is the post-focal Adaptive Optic module that will be installed at the E-ELT at the first light of the telescope. The main function of MORFEO is to relay the light beam from the ELT focal plane to the client instrument while compensating the effects of the atmospheric turbulence and other disturbances affecting the wavefront from a source. MORFEO will provide the ELT with two adaptive optics modes: a very high correction over a small FoV ( $\sim 10$  arcsec, with performances rapidly degrading with distance from the bright natural star used to probe the wavefront – Single-Conjugate Adaptive Optics, SCAO mode) and a moderate correction over a wide FoV ( $\sim 60$  arcsec, with homogeneous performances over the whole FoV – Multi-Conjugate Adaptive Optics, MCAO mode). The applicability of the SCAO mode will be limited by the need of a bright (approximately  $V \leq 16.0$ ) star within a few arcsec of the scientific target. In the ideal SCAO case, the bright star that is used to sense the wavefront (natural guide star, NGS) coincides with the scientific target (e.g. for exoplanet imaging). On the other hand, the MCAO mode will use three NGS (with  $H \leq 21.0$ ) to be found within an

annular patrol field with inner radius of  $\sim 45$  arcsec and outer radius of  $\sim 100$  arcsec (figure 2.7).

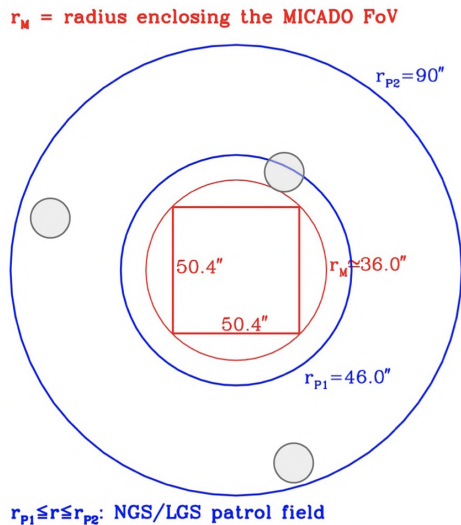


Figure 2.7: Schematic view of the MORFEO exit focal plane. The red square is the MICADO FoV. The three grey circles are the pick-off mirrors for the three NGS, which can be deployed on the NGS patrol field. In MCAO mode, the three small movable pick-off mirrors (each patrols one of three  $120^\circ$  sectors) will pick the light from three suitable NGS lying within the NGS patrol field.

According to the current version of the instrument design, these NGS will correct low-order modes of the wavefront distortions, while the sensing of six artificial laser guide stars (LGS) will be used to correct for high-order modes. The six LGS are produced by excitation of the atmospheric sodium layer (at an altitude of  $\sim 90$  km) with six laser beacons (with  $\lambda = 589.2$  nm) propagated from ELT. Concerning the usage of the SCAO versus the MCAO modes, it is worth noticing that the requirement of a bright star very close ( $10''$ ) to the source of interest (i.e. the SCAO mode) may severely limit the targets that can be observed (i.e. the sky-coverage). For the above reasons, the MCAO mode may be often the only or recommended way to observe targets, and so it is the chosen mode adopted in this work. In fig.2.8 a comparison of the Strehl ratio (SR) obtained in SCAO (left) and MCAO (right) modes in Ks band is reported. It should be recalled that the SR is frequently defined as the ratio of the peak aberrated image intensity from a point source compared to the maximum attainable intensity using an ideal optical system limited only by diffraction over the system's aperture. From fig.2.8 it is possible to note that the maximum values (at the center) are  $SR_{scao} \sim 0.78$  and  $SR_{mcao} \sim 0.68$ , whereas at a distance of  $20''$  from the centre  $SR_{scao} \sim 0.40$  (roughly half of the max value) and  $SR_{mcao} \sim 0.65$  (similar to the max value): as expected, the SCAO mode provides a stronger

correction at the detector center (where the NGS is positioned) but degrades faster than the MCAO mode.

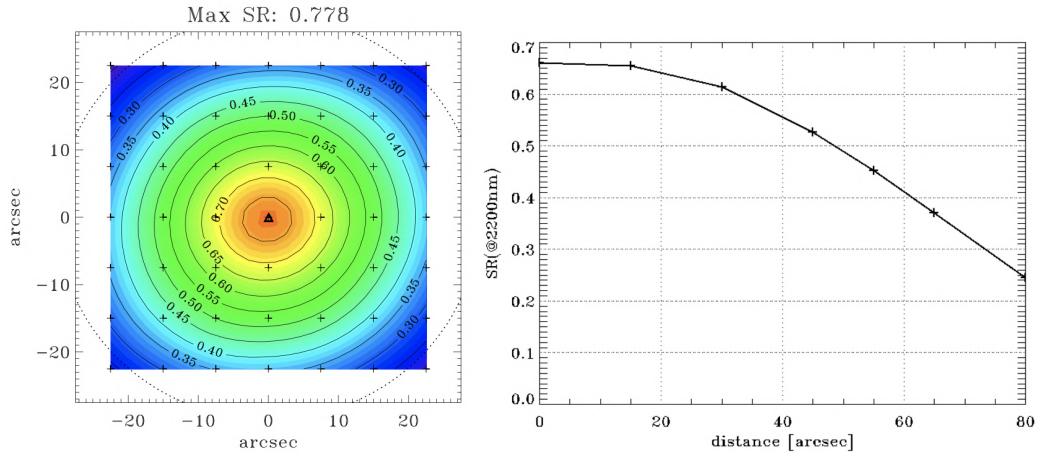


Figure 2.8: Comparison between the Strehl ratio in the SCAO (left) and MACO (right) modes, showing typical values and how fast it degrades with the distance from the center.

## 2.4.1 MORFEO Design

A simplified overview of the MORFEO structure and architecture is shown in fig.2.9, while its functional overview is reported in fig.2.10.

The main optical path baseline has 8 reflections: 2 aspheric concave mirrors, 2 spherical deformable mirrors (DMs, one convex and one concave), 1 dichroic and 3 fold mirrors. In fact, in the current configuration the MORFEO baseline provides the presence of the two DMs, indicated as M9 and M10 in the two reported figures. In particular, the DM1/M9 is a convex mirror with a radius of curvature of  $\sim 15.8$  m and a diameter of 928 mm, whereas the DM2/M10 is a concave mirror with a radius of curvature of  $\sim 15.3$  m and a diameter of 1225 mm. The effect of the 2nd DM is to increase image quality and its stability under variations of atmospheric turbulence and seeing conditions, as well as to significantly improve the spatial homogeneity of the point spread function (fig.2.11). This means that the fraction of targets for which a scientifically useful minimum Strehl ratio can be achieved (sky coverage) will increase significantly thanks to the addition of the second deformable mirror.

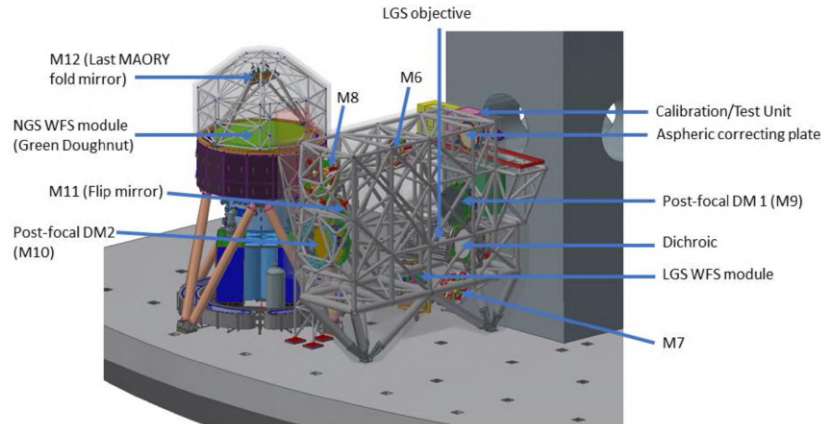


Figure 2.9: General overview of the MORFEO instrument installed on the Nasmyth platform with MICADO.

The plot in fig.2.11 was obtained assuming average atmospheric conditions (i.e. indicated with  $P50$  on the top of the figure), that are indeed the ones adopted in this project.

Coupled with MICADO, MORFEO will enable ELT to perform diffraction limited near infrared observations over a large fraction of the sky accessible from Cerro Armazones. Finally, MORFEO is being designed and built by a consortium of partners in Italy (with INAF as the lead institute), France and Ireland, together with ESO. Regarding to the status of MORFEO’s project, it recently passed the Preliminary Design Review. Subsequently, the project will enter the final design phase (12-18 months duration), followed by the manufacture and test phase in Europe. Therefore the first light of the instrument is expected by the end of 2028.

## 2.5 Science Cases

A preliminary collection of science cases that will be possible with MORFEO/MICADO is reported in the *MORFEO science cases white book* (see [Fiorentino et al. 2020](#)). The collected science cases address many of the major questions of astrophysics:

1. Planetary systems including our own Solar System, exoplanets and formation of planetary systems.

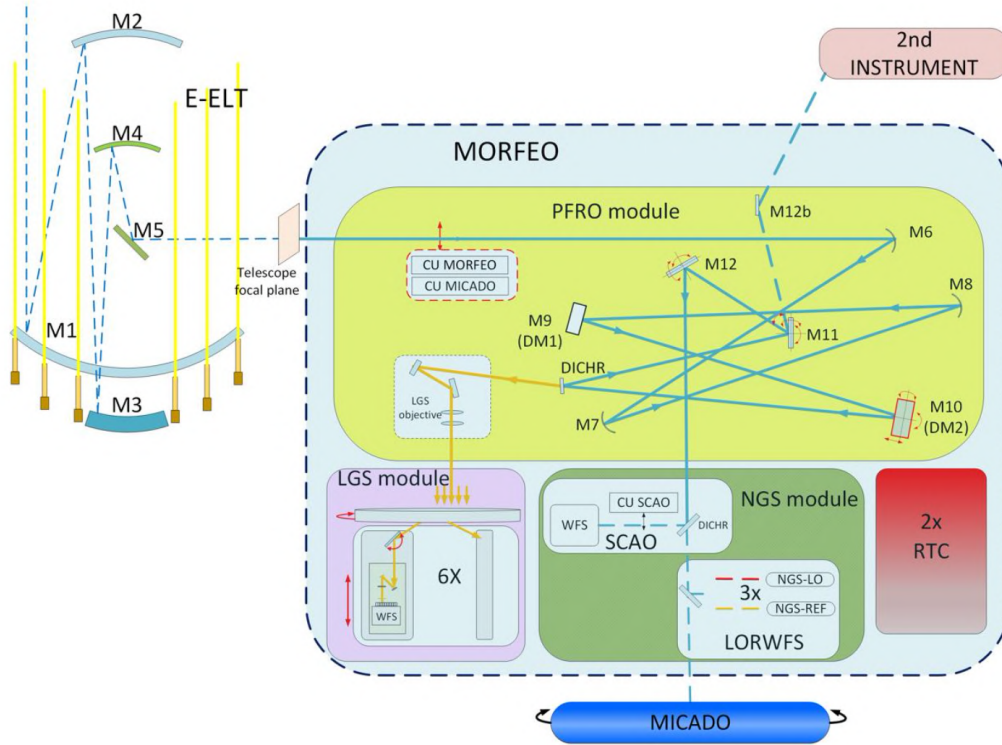


Figure 2.10: Functional overview of the MORFEO module in the context of the ELT and MICADO client instruments

The ELT will make important contributions to the study of the Solar System, especially for the faint trans-Neptunian objects and Moons, characterizing their surfaces with a detail never obtained before. In addition, the system MICADO+MORFEO has an incredible potential for the study of exoplanets, distant planetary systems, over a range of evolutionary stages in order to shed light on planetary systems formation and evolution.

2. Nearby stellar systems within our own Galaxy and its satellites.

The unprecedented angular resolution of the ELT makes crowded field photometry and astrometric applications particularly attractive. An example on this topic is reported in fig.2.12, which shows a comparison of how crowded stellar fields (with the three indicated stellar densities) appear when observed by the the Hubble Space Telescope (HST),

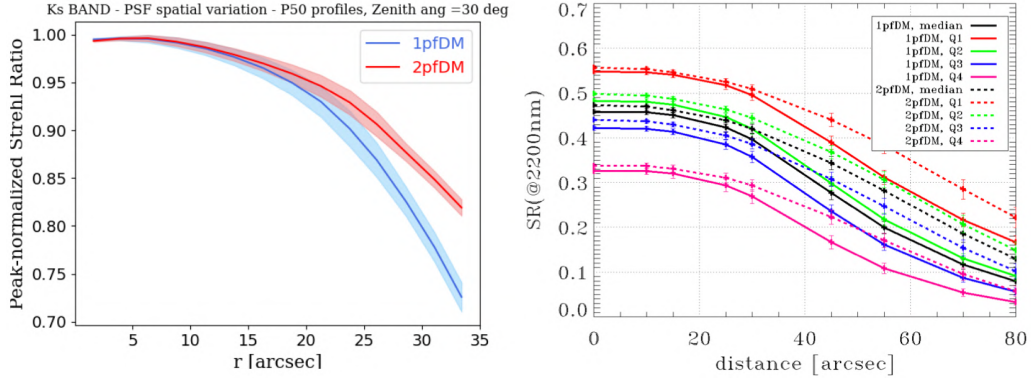


Figure 2.11: Left: Peak-normalized SR ratio as a function of the distance in arcsec from the MICADO center, in Ks, and for 1 post-focal DM (blue) and 2 post-focal DMs (red) MORFEO configurations. The solid line is the average SR within the annulus at distance  $r$ , while the shaded region denotes the standard deviation. Right: SR as function of the distance in arcsec from the MICADO center, in Ks, for 1DM (solid lines) and 2DM (dashed lines) MOREFO configurations in different atmospheric conditions.

left), the James Webb Space Telescope (JWST, centre), and MORFEO+MICADO@ELT (right). The bottom row is comparable with the stellar density at a radius of  $4\text{--}5 R_{eff}$  for the elliptical galaxy NGC 4472 in the Virgo Cluster, whereas the top row corresponds to an internal region at  $2 R_{eff}$  and illustrates the superb capability of ELT in resolving individual stars in extremely dense stellar fields.

The ELT capabilities will permit to map individual stellar orbits in external stellar systems, or gas closer to the event horizon of Sgr A\* with unprecedented accuracy with direct imaging. Astrometry and proper motions measurements will be doable for numerous individual stars in resolved stellar systems, as globular clusters, enabling us to trace the presence (or absence) of black holes in a range of environments even in other galaxies, as well as making accurate mass models by combining these results with radial velocity measurements to obtain a 3D view of stellar motions. This type of studies will be possible up to roughly the distance of the Virgo cluster ( $\sim 18$  Mpc).

3. Local Universe, with science cases aimed to study the stellar content and the structure of distant stellar systems that can be at least partially

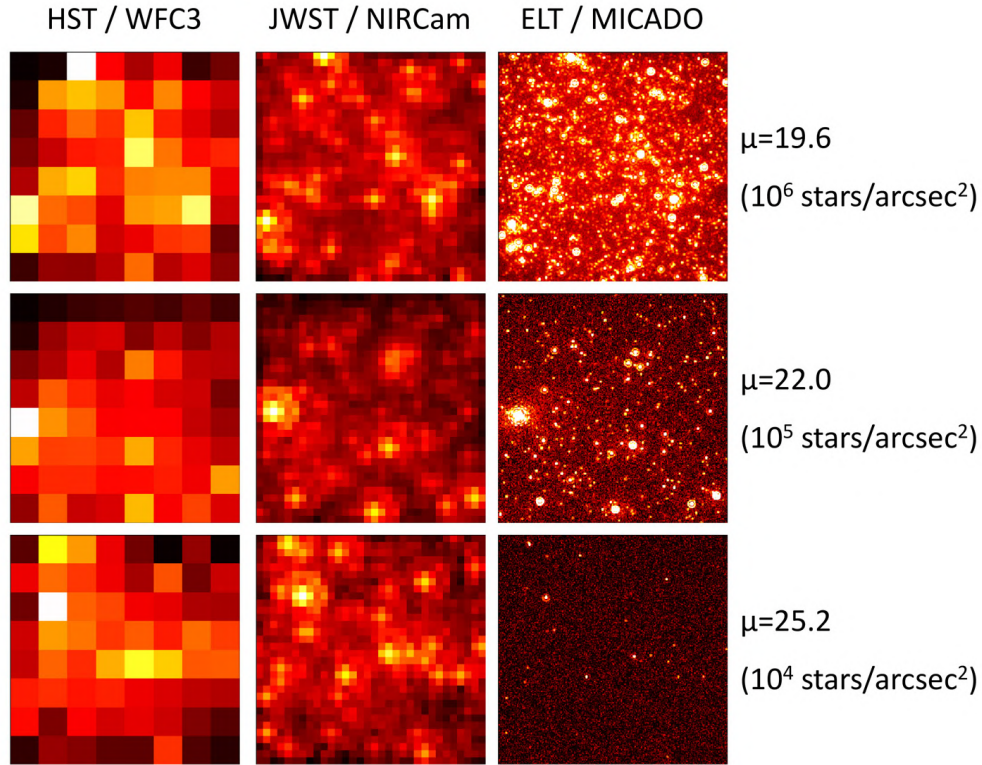


Figure 2.12: Comparison of how crowded stellar fields appear when observed by the HST (left), the JWST (centre), and MICADO@ELT (right) for three different stellar densities. The images shown in the last column are ScopeSim simulations and each individual panel is 1" across. Credit: ESO/MICADO consortium.

resolved.

With the spatial resolution of MICADO, it will be possible to make uniquely detailed studies of both local and very high-redshift galaxies. In particular, new dense regions in nearby galaxy groups will fall within the range of systems whose individual stars will be resolved with MORFEO+MICADO, and their SFH derived through resolved-star color-magnitude diagrams.

4. High-redshift Universe, with science cases addressing the formation and evolution of structures as well as cosmology.

For much more distant and high-redshift ( $z > 1$ ) galaxies, multi-wavelength broad-band and narrow-band imaging will reveal the structure of galaxies at the peak of their star formation activity, mass assembly, and morphological transformations (referring to the Cosmic Noon at  $z \sim 2-3$ ). As we will demonstrate in this thesis work, the formidable sensitivity and resolution of MORFEO+MICADO will also be able to probe the star formation activity in the centre of dense high-redshift galaxies in extraordinary detail. On top of that, we will be able to trace the evolution with redshift of the black hole mass and determine how this relates to the other galaxy properties, observing the effects of AGN feedback and the role of environment in triggering and shutting down its activity.

## Chapter 3

# Simulating HST-dark galaxies with SIMCADO

The purpose of this project is to verify the possibility to detect the high-redshift obscured galaxies described in section 1.4. These sources are known to be heavily obscured and, with our current instrumentation, they tend to escape the sensitivity limit of optical and UV observations. In this sense the ELT will be tremendously useful for both its large collective area and its high angular resolution, allowing us to study faint sources with levels of details never achieved until now with the current telescopes.

For these reasons, starting from assumptions on the nature and morphology of these observed and still not understood HST-dark galaxies, we simulated images as acquired with MICADO+MORFEO in different bands using the SIMCADO simulation tool.

SIMCADO is a data simulation package written in Python 3 and designed to simulate the effects of the atmosphere, ELT, and MICADO instruments on the incoming light (Leschinski et al., 2016). It provides to the user raw data sets that will be similar to what MICADO will produce. Although SIMCADO is still under development, its current version (v0.7) can be used to address many questions about the future performance of the MORFEO+MICADO imaging mode for various science cases.

SIMCADO gives the user the possibility to choose and to simulate either point-like or extended sources; in both cases, the simulator provides a library of stellar spectra, as well as various templates for the most common types of galaxies (e.g. ellipticals, spirals, starbursts, ULIRGs). On top of that, there is also the possibility to import new spectra or images provided by the user:

this is an important and necessary function to reach the scientific goal of this project, as we will discuss largely in this chapter.

First of all, to show the versatility of this simulator, in fig. 3.1 and 3.2 are reported some image examples generated by SIMCADO, showing its utility and capabilities. In particular, in fig.3.1-left a simulated elliptical galaxy at redshift 0.01, with a Vega magnitude of  $mag_J = 18.0$ , a concentration (or Sérsic) index of 4 and a half light radius of  $1.8''$  is shown .

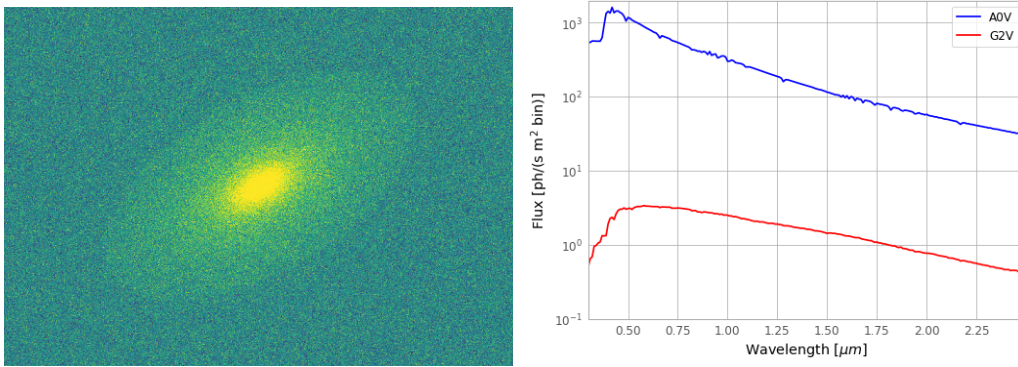


Figure 3.1: Left: simulated elliptical galaxy with  $mag_J = 18.0$ . Right: Examples of stellar spectra in the SIMCADO library: an A0V class star normalized to J=15 (blue spectrum) and a G2V star normalized to J=20 (red).

```

SED_z02 = simcado.source.redshift_SED(0.2, "spiral", 18.0, "TC_filter_J.dat")
star1 = simcado.source.star("G2V",19.0,filter_name="TC_filter_J.dat",x=-1,y=-1)
star2 = simcado.source.star("B0V",20.0,filter_name="TC_filter_J.dat",x=1,y=1)
my2stars = star1 + star2

gal = simcado.source.spiral(half_light_radius=1.0,
plate_scale=0.004, magnitude=18.0, filter_name='TC_filter_J.dat',
normalization='total', spectrum=SED_z02, n=1)

system = gal + my2stars

gal_sim = simcado.run(system, OBS_DIT=360, OBS_NDIT=1.0,
detector_layout="small", INST_FILTER_TC="TC_filter_J.dat",
filename="Galaxy_&_2stars.fits")

```

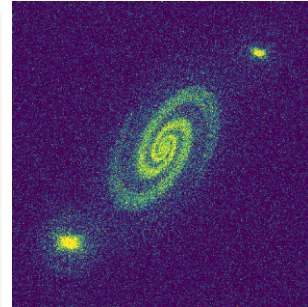


Figure 3.2: Simulated composite system including a spiral galaxy and two stars. The output image on the right is created using the code reported on the left.

On the other hand, fig.3.1-right shows as an example some stellar spectra available in the SIMCADO library, normalized into the desired photometric

band. In this particular case, the emission between  $0.3$  and  $2.5\mu m$  of two different stars is shown: an A0V class star with  $mag_J = 15.0$  (in blue) and a G2V class star with  $mag_J = 20.0$  (in red). The units are wavelength [ $\mu m$ ] on the x-axis and fluxes [photons/s/m<sup>2</sup>/bin] on the y-axis (where *bin* denotes the wavelength bins whose centers are indicated in the x-axis): these are the units used by the simulator for all stellar spectra and galaxy SEDs.

Finally, fig.3.2 shows the possibility to also combine two (or more) source objects such as, in this example, a spiral galaxy and two stars. On the left the script that produced the output image on the right is reported, showing that the system is composed by: 1) a spiral galaxy at redshift 0.2, normalised at  $mag_J = 18.0$ , with a concentration (or Sérsic) index of 1 and a half light radius of 1", 2) a G2V class star with  $mag_J = 19.0$  and 3) a B0V class star with  $mag_J = 20.0$ . To run a simulation and create the displayed images, it is necessary to constrain several parameters. To be brief, the majority of these parameters are not mentioned in this work but here are reported the most important ones and their associated values, when possible:

- *obs-dit*: length of a single simulated exposure time in [s];
- *obs-ndit*: number of exposures taken;
- *inst-filter-tc*: file of the filter used for the simulated observation;
- *detector-layout*: detector layout chosen. It could be set as “small” (1024 × 1024 pixels detector at the centre of the middle chip), “centre” (4096 × 4096 pixels detector; middle chip of the 9 total in MICADO) and “full” (all 9 MICADO chips). To observe and so simulate high-z galaxies, there is no need to read out all 9 MICADO chips for each observation but, since they have small angular dimensions, the middle chip covers the entire galaxy extension in the majority of cases. For this reason, and to save simulation time, we set the *detector-layout* parameter to “centre” along this work;
- *mode*: can be either “wide” (4 mas/pixel) or “zoom” (1.5 mas/pixel). Along this work, the wide mode is used, as the zoom mode is typically used for astrometric studies;
- *inst-ao-temperature*: temperature inside of AO module in [deg Celsius]. As MORFEO is supposed to operate at ambient temperature in the range [0 °C - 15 °C], this parameter is set to 5 °C;

- *scope-psf-file*: the file where the PSF is stored. As discussed in section 2.4, MORFEO will provide two different types of AO correction, a very high correction over a small FoV (diameter  $\sim 10$  arcsec, with performances rapidly degrading with distance from the bright natural star used to probe the wavefront – SCAO mode) and a moderate correction over a wide FoV (diameter  $\sim 60$  arcsec, with homogeneous performances over the whole FoV – MCAO mode). As anticipated in section 2.4, the chosen mode for this work is the MCAO, for the larger portion of sky accessible (i.e. sky coverage).

In this project, the potential of SIMCADO is used to simulate HST-dark galaxies in the four main filters of MICADO, reported in fig.2.5, that are I, J, H and Ks. In order to accomplish this goal, it is necessary first of all to have information about their SEDs and magnitudes (section 3.3) and assumptions about their morphologies (following section).

### 3.1 Main Assumptions

As mentioned in section 1.3, LIRGs and ULIRGs are galaxies extremely luminous at IR wavelengths with values of  $L_{IR} \gtrsim 10^{11} L_{\odot}$  (LIRGs) and  $L_{IR} \gtrsim 10^{12} L_{\odot}$  (ULIRGs). These luminosities are caused by their high star formation rates ( $\sim 10\text{-}10^2 M_{\odot}/yr$ ) and by the presence of large amount of dust absorbing the optical/UV light emitted by young massive stars, and re-emitting at IR/sub-mm wavelengths. In the evolutionary scenario already presented, these starburst phenomena are often triggered by mergers and/or accretion by gas filaments, therefore the morphology of LIRGs is typically irregular.

In order to simulate HST-dark galaxies with SIMCADO, it is necessary to make assumptions about their morphologies. In the end, we will see how these galaxies would appear if observed by MICADO in the  $0.8\text{-}2.4\mu m$  range. However, as mentioned in section 1.4, these galaxies are often invisible in this wavelength range (i.e. so faint that they escape even the sensitivity of recent deep surveys) or are observed with poor spatial resolution (see IRAC images in fig.1.8), so that their morphologies remains unconstrained. Therefore, we assume that, since HST-dark galaxies and local LIRGs are likely to have similar SEDs (i.e. similar spectral features such as dust absorption of UV emission and strong dust emission in FIR), also their morphologies could be similar (i.e. often characterised by mergers and/or gas filaments, and so

presenting irregular shapes). Once verified the assumption of similar SEDs in section 3.3, we simulate HST-dark galaxies adopting HST images of local LIRGs to describe their morphologies.

In this regard, it is necessary to consider the redshift effect on the galaxies' spectra: when observing a distant (i.e. high-redshift) galaxy in a given wavelength range, a different rest-frame range is sampled, according to the formula 3.1:

$$z = \frac{\lambda_{obs} - \lambda_{em}}{\lambda_{em}} \rightarrow 1 + z = \frac{\lambda_{obs}}{\lambda_{em}} \quad (3.1)$$

According to eq.3.1, in order to simulate the morphology of an HST-dark source at  $z=2$  in the I and H bands, one needs to use local (i.e. considered rest-frame) images at about 2600 Å and at about 5300 Å, respectively. Thus, for each simulation at given redshift, we adopt the HST local image in the filter that best matches the rest-frame wavelengths of the simulated observation band, as summarized in tab.3.1:

z	I	J	H	Ks
0	8000 Å	12480 Å	16350 Å	21450 Å
2	2670 Å	4160 Å	5450 Å	7150 Å
3	2000 Å	3120 Å	4090 Å	5360 Å
4	1600 Å	2500 Å	3270 Å	4290 Å

Table 3.1: The first row ( $z=0$ ) shows the values of central wavelengths corresponding to the IJHKs bands, whereas the rows below report the rest-frame sampled wavelengths at redshifts 2, 3 and 4.

## 3.2 Local LIRGs

To perform our simulations, we choose five of the most popular and studied local LIRGs/ULIRGs listed in tab.3.2.

In particular, their redshifts were taken from the NASA/IPAC Extragalactic Database (NED), while their total IR luminosities (8-1000  $\mu m$ ) are given by Sanders et al. (2003b). The SFR of these galaxies can be estimated from their  $L_{IR}$  using the relation from Kennicutt Jr. (1998b), calibrated with a Salpeter IMF, between SFR and IR-luminosity:

$$SFR [M_{\odot}/yr] \sim 1.7 \cdot 10^{-10} L_{FIR} [L_{\odot}] \quad (3.2)$$

Name	$z$	$D_L$ [Mpc]	$Log L_{IR}$ [ $L_\odot$ ]
M82	0.00090	3.9	10.77
ARP220	0.01840	80.4	12.21
NGC6240	0.02431	106.7	11.85
NGC6090	0.02930	129.1	11.51
IRAS 20551-4250	0.04300	188.6	12.00

Table 3.2: Names, redshifts, luminosity distances and IR-luminosities of the five chosen local LIRGs/ULIRGs.

Relation 3.2 provides SFR values of  $\sim 10^1$ - $10^2 M_\odot/yr$ .

The semi-empirical SEDs of these galaxies are taken from the SWIRE Template Library (Polletta et al., 2007) and are shown in fig.3.3 in units of [ $erg/s/cm^2/\text{\AA}$ ], while their HST images are taken from the Mikulski Archive for Space Telescopes (MAST). The chosen sample contains star-forming galaxies (starbursts in some cases) characterised by dusty, obscured and irregular shapes (see HST images on the following chapter) and therefore classified as irregulars (I0 in most cases): in fact, galaxies such as ARP220, NGC6240, NGC6090 and IRAS 20551-4250 have all a peculiar morphology, suggesting some stage of merging (see Scoville et al. 1998, Dinshaw et al. 1999, Dasyra et al. 2006). Thus, by adopting this sample of local LIRGs/ULIRGs for our simulations, we are intrinsically assuming that also high-redshift HST-dark galaxies are systems where the intense SF is triggered by some sort of merging with companions or interaction with the surrounding intergalactic medium (i.e. gas accretions, see Putman 2017). However, as we will later discuss in Chapter 5, this is a mere assumption, and other types of galaxy morphologies may be implemented into the simulations.

As the goal is to simulate sources in the NIR (IJHK bands) at redshift  $> 2$ , we need images from FUV to optical wavelengths, as shown in tab.3.1. Therefore the LIRGs selection (tab.3.2) was made also considering the availability of HST images in those bands, in particular we selected their images as follows:

- The images should contain the emission of the whole galaxy in the bands needed to match the rest-frame at different redshifts (from FUV to red optical bands);

- The images should be taken with HST in order to be at the highest possible resolution;
- We choose images corrected for cosmic rays (i.e. files fits with format *drc* or *drz*);

Therefore, our sample of these five specific galaxies was chosen in order to respect the three conditions that we have already discussed:

1. The local galaxies have common characteristics with HST-dark galaxies, such as, presumably, a high IR luminosity and a high SFR;
2. Their semi-empirical SEDs are included in the SWIRE Template Library;
3. They are sufficiently sampled in the literature, and in such a way that their images respect the three criteria listed early.

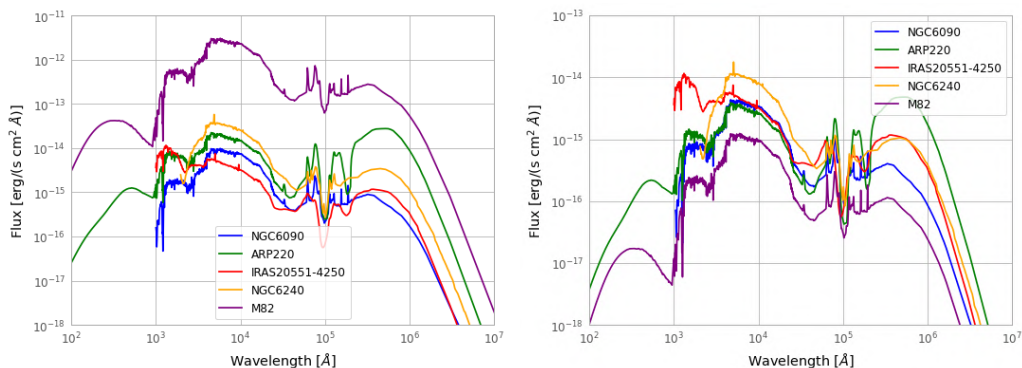


Figure 3.3: Observed SEDs of the 5 chosen local LIRGs, located at different redshifts (left), and shifted to the same redshift for a straightforward comparison (right). In particular, the plot on the right shows the galaxies at the same distance as IRAS 20551-4250 ( $z=0.043$ ). Note that the two graphs are not on the same y-scale; note also how luminous M82 is at its redshift as it is much closer than the other sources (see table 3.2).

In order to simulate how these galaxies would appear at higher-redshift we accounted for that objects appear fainter and smaller with increasing redshift (i.e. there is a flux dimming and also an angular size shrinking

with distance). The following sections describe in detail the image and SED transformations that we applied in order to simulate the selected galaxies at different (higher) redshifts.

### 3.2.1 The task *source-from-image* and the plate scale

A crucial task of SIMCADO is *source-from-image()*. It allows to create a source based on a 2D numpy array provided by the user and therefore different from the default ones, like elliptical and spiral galaxies as in fig.3.1 and 3.2. In our study, the 2D array comes from HST fits images, while for the source spectra we adopt the SEDs described in the previous section. In order to simulate our images, we also need to assign an angular scale to the image pixels. SIMCADO then saves the pixel coordinates and associates to each pixel a flux value computed from the provided spectrum properly scaled by the 2D array image values. Therefore this task is fundamental to import images of galaxies with morphologies different from those contained in the simulator. The “plate-scale” parameter, i.e. the pixel angular size of the user-provided image, is a crucial ingredient to properly simulate how local LIRGs would appear at higher redshifts. In fact, since sources appear smaller at higher distances, one needs to reduce the real plate scale of the local image accordingly to the simulated redshift. In particular, four kind of information are needed:

- The number of pixels on the chosen image;
- The real plate scale of the adopted local image (this depends on the observation instrument, for example 0.025”/pixel for ACS/HRC@HST and 0.05”/pixel for ACS/WFC);
- The local and simulated scales (i.e. the scales [kpc/”] corresponding to the local image and the simulated high-z image).

Once adopted a cosmological framework, these last two scales are fixed by the redshift of the local image and the redshift of the simulation. From these information one could calculate: 1) the dimension in kpc of the whole image containing the galaxy, 2) the dimension in arcsec (i.e. its angular diameter) of the whole simulated image at high redshift and therefore, dividing by the number of pixels, 3) the plate scale for this specific simulation.

We need to keep in mind that the angular diameter of an object does not decrease monotonically with redshift. That would be the case of a static Universe, but since the Universe is expanding, distant objects will appear to increase in size, i.e., the light traveling from a distant galaxy appears to spread out. For closer galaxies this is not significant and their apparent diameter decrease, but around  $z \sim 1.6$  cosmic expansion starts becoming a dominant factor compared to galaxy distance: as a result, galaxies with higher redshifts actually start appearing larger. Therefore also their respective simulated plate scales have similar behavior.

From trigonometry considerations, one can recall the classical formula that defines the angular size distance  $D_A$ :

$$D_A = \frac{D}{\theta} \quad \rightarrow \quad \theta = \frac{D}{D_A} \quad (3.3)$$

where  $D$  is the transverse extent or diameter of an object and  $\theta$  is the angle in radians that it subtends on the sky. Therefore  $D_A(z)$  has a maximum at  $z \sim 1.6$ , corresponding to the redshift at which objects of a given proper size  $D$  will subtend the minimum angle  $\theta$  on the sky (this trend is shown in fig.3.4-left for a redshift range between 0 and 10). Besides, one could expect that also the scale at a given redshift has a similar behavior since  $scale[kpc/'' ] = D/\theta = D_A$ . On the contrary, we would expect that  $\theta$  would have an inverse behavior since, for a fixed diameter,  $\theta \propto 1/D_A$  (fig.3.4-right).

Finally, recalling the correlation between  $D_L(z)$  and  $D_A(z)$ , i.e.  $D_L(z) = D_A(z) \cdot (1+z)^2$ , it is possible also to rewrite the relation 3.3 as:

$$\theta = \frac{D \cdot (1+z)^2}{D_L} \quad (3.4)$$

The plots in fig.3.4 show that when an object (with a fixed dimension) is moved to higher redshifts, its angular size first decrease but soon begins to increase, indeed presenting a minimum angular diameter at  $z \sim 1.6$ .

### 3.2.2 The Flux-Luminosity Distance Relation

Another problem to face is that the apparent brightness (or apparent flux) of a galaxy depends on how far away it is, i.e. a galaxy becomes fainter and redder with redshift. Indeed, we have that the luminosity (L), apparent flux (F), and distance (r) are related by the equation (see [Peebles 1993](#)):

$$F = \frac{L}{4\pi(a_0 r)^2(1+z)^2} \quad (3.5)$$

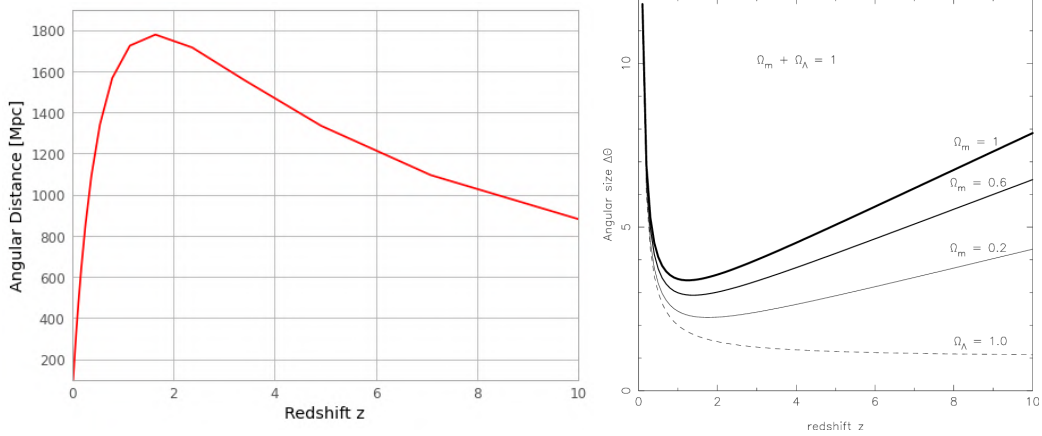


Figure 3.4: Angular distance in Mpc (left) and angular size (right) as a function of redshift. These plots are shown to demonstrate how objects appear to increase in size after a certain distance, and to show also typical values of these two quantities in the range of redshift [0-10]. The image on the right was taken from [Sahni and Starobinsky \(2000\)](#).

So that the apparent brightness of a source is equal to the intrinsic luminosity divided by  $4\pi$  times the square of the distance. We can interpret this equation by thinking of the photons being “spread out” over a sphere whose area is  $4\pi(a_0r)^2$  at the present epoch, where  $a_0$  is the cosmological scale factor for the current Universe. On top of that, the apparent flux is diminished by the factor  $(1+z)^2$  because the energy of each photon is diminished by the redshift factor  $(1+z)$ , as well as the rate of arrival of photons.

Since  $D_L = a_0r(1+z)$ , we can write:

$$F = \frac{L}{4\pi D_L^2} \quad (3.6)$$

We can rewrite this equation recalling the relation between the cosmological scale factor  $a$ , its current value  $a_0$  and the redshift  $z$ :

$$\frac{a_0}{a} = 1+z \quad , \quad \frac{a}{a_0} = \frac{1}{1+z} \quad (3.7)$$

and the definition of redshift, using the wavelength emitted ( $\lambda_{em}$  or  $\nu_{em}$ ) from an object at a generic  $z$  and the observed one ( $\lambda_{obs}$  or  $\nu_{obs}$ ):

$$\frac{\lambda_{obs}}{\lambda_{em}} = \frac{a_0}{a} = 1+z \quad , \quad \frac{\nu_{obs}}{\nu_{em}} = \frac{a}{a_0} = \frac{1}{1+z} \quad (3.8)$$

Therefore, equation 3.6 can be written considering that the monochromatic flux observed at a wavelength  $\lambda_{obs}$  in a bandwidth  $\delta\lambda_{obs}$  was radiated at a wavelength  $\lambda_{em} = \lambda_{obs}(a/a_0)$  in a bandwidth  $\delta\lambda_{em} = \delta\lambda_{obs}(a/a_0)$  so:

$$\frac{F_{obs,\lambda_{obs}}}{\delta\lambda_{em}} = \frac{L_{em,\lambda_{em}}}{4\pi D_L^2} \quad (3.9)$$

$$\frac{F_{obs,\lambda_{obs}}}{\delta\lambda_{obs}(a/a_0)} = \frac{L_{em,\lambda_{obs}(a/a_0)}}{4\pi D_L^2} \quad (3.10)$$

$$\frac{F_{obs,\lambda}}{\delta\lambda}(1+z) = \frac{L_{em,\lambda/(1+z)}}{4\pi D_L^2} \quad (3.11)$$

$$F_{obs,\lambda} = \frac{L_{em,\lambda/(1+z)}}{4\pi D_L^2} \frac{1}{1+z} \quad (3.12)$$

Where  $F_{obs,\lambda}$  is the flux observed at  $\lambda_{obs}$ ,  $L_{\lambda/(1+z)}$  is the luminosity emitted at  $\lambda_{em} (= \lambda_{obs}/(1+z))$ , and  $D_L(z)$  is the luminosity distance. Equation 3.12 is useful since it relates the redshifted observed monochromatic flux with the rest-frame emitted luminosity of a source if its redshift is known (through  $z$  and  $D_L(z)$ ).

However, our goal is to find an equation containing the flux of a local object at its true redshift and the one that it would have at a higher redshift. Therefore, to achieve such a relation, we have to express  $L_{em,\lambda/(1+z)}$  in eq.3.12 using known quantities. In fact, the observed flux  $F^0$  of a source with luminosity distance  $D_{L,0}$  can be written as:

$$F_{obs,\lambda}^0 = \frac{L_{em,\lambda}}{4\pi D_{L,0}^2} \quad \rightarrow \quad L_{em,\lambda} = 4\pi D_{L,0}^2 \cdot F_{obs,\lambda}^0 \quad (3.13)$$

Therefore, eq.3.12 could be expressed as:

$$F_{obs,\lambda} = \frac{F_{obs,\lambda/(1+z)}^0 4\pi D_{L,0}^2}{4\pi D_L^2} \frac{1}{1+z} \quad (3.14)$$

$$F_{obs,\lambda} = F_{obs,\lambda/(1+z)}^0 \left( \frac{D_{L,0}}{D_{L,z}} \right)^2 \frac{1}{1+z} \quad (3.15)$$

Eq.3.15 is crucial for this work since it shows the correlation between the fluxes of the same source at different luminosity distances (i.e. redshifts),

that is indeed what is needed to achieve here. The goal, in fact, is to scale the local SED of a LIRG at a higher distance  $D_{L,z}$ , different from the true luminosity distance  $D_{L,0}$  that is much closer/lower as shown in table 3.2. Note that eq.3.15 is valid for  $F_\lambda$ , but it can be used also for  $F_\nu$  with the term  $1+z$  in the numerator rather than the denominator:

$$F_{obs,\nu} = F_{obs,\nu}^0 \left( \frac{D_{L,0}}{D_{L,z}} \right)^2 (1+z) \quad (3.16)$$

Fig.3.5 shows how this method works.

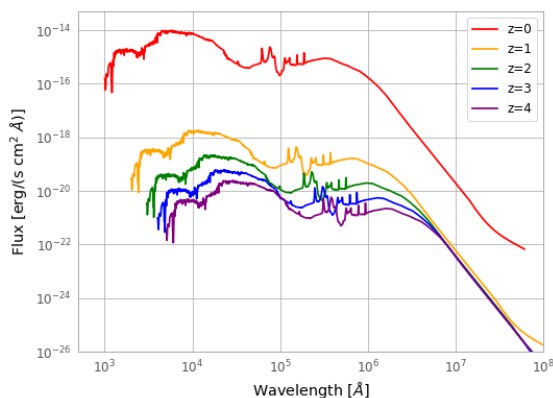


Figure 3.5: SEDs of NGC6090, at  $z=0$  (in red) and at higher redshifts (indicated in the legend).

Finally, this method was used to create fig.3.3-right by scaling the four galaxies' emission to the redshift of IRAS 20551-4250 ( $z=0.043$ ).

Once our SEDs have been properly shifted to higher redshifts, we need to convert them into the units required by the SIMCADO simulator. In practice, our SEDs have to be transformed as follows:

1. Shifted with the distance, as described above;
2. Resampled in wavelength to a regular grid (wavelengths expressed in micron);
3. Converted to the units required in input by SIMCADO [ $photons/s/m^2/bin$ ].

In order to perform the SED resampling, we used a Python package named *specutils* and, in particular, its task *FluxConservingResampler*. This resampling algorithm conserves the overall integrated flux and is based on the

equations reported in Carnall (2017). The accuracy of this algorithm is shown in fig.3.6, where we report the SED of NGC6090 in the range [4000-30000 Å] first with an irregular binning (on the left) and then with a regular bin width of 10 Å along the whole wavelength interval (on the right).

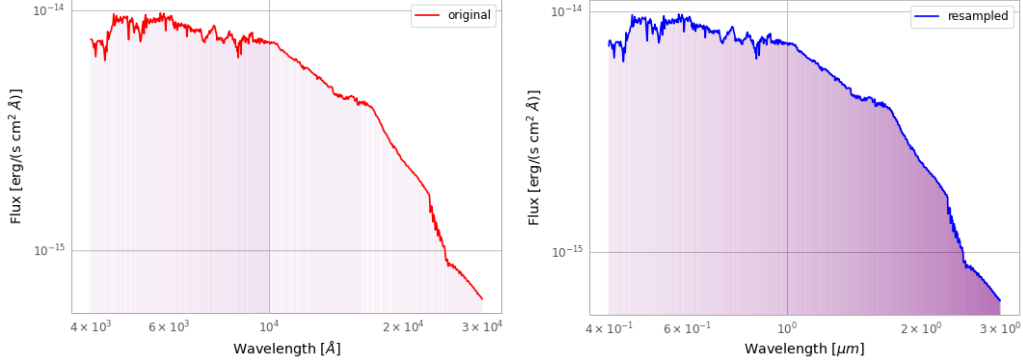


Figure 3.6: Demonstration on how the Python task *FluxConservingResampler* transforms an irregular vector into a regular one. The vertical lines indicate the binning before (560 points) and after (2600 points) the resampling task.

Finally, to convert the flux in units of  $[erg/s/cm^2/\text{Å}]$  into units of  $[photons/s/m^2/bin]$  we need to divide by  $h\nu$ , and multiply by  $\lambda/hc$ :

$$F \left[ \frac{photons}{s \cdot cm^2 \cdot \text{Å}} \right] = \frac{\lambda}{6.6 \cdot 10^{-27} \text{ erg s} \cdot 3 \cdot 10^{18} \text{ Å/s}} \cdot F \left[ \frac{erg}{s \cdot cm^2 \cdot \text{Å}} \right] \quad (3.17)$$

$$F \left[ \frac{photons}{s \cdot cm^2 \cdot \text{Å}} \right] = 5.03 \cdot 10^7 \cdot \lambda[\text{Å}] \cdot F \left[ \frac{erg}{s \cdot cm^2 \cdot \text{Å}} \right] \quad (3.18)$$

$$F \left[ \frac{photons}{s \cdot m^2 \cdot \text{Å}} \right] = 5.03 \cdot 10^{11} \cdot \lambda[\text{Å}] \cdot F \left[ \frac{erg}{s \cdot cm^2 \cdot \text{Å}} \right] \quad (3.19)$$

Fig.3.7 shows the comparison between these two quantities: similarly to fig.3.6, here we report the SED of NGC6090 in the range [4000-30000 Å], first in units of  $erg/s/cm^2/\text{Å}$  and then converted to  $photons/s/m^2/\text{Å}$ .

Finally, to get  $[photons/s/m^2/bin]$  from  $[photons/s/m^2/\text{Å}]$ , one can simply multiply the photon flux by the bin width (in Å) chosen to regrid the wavelengths.

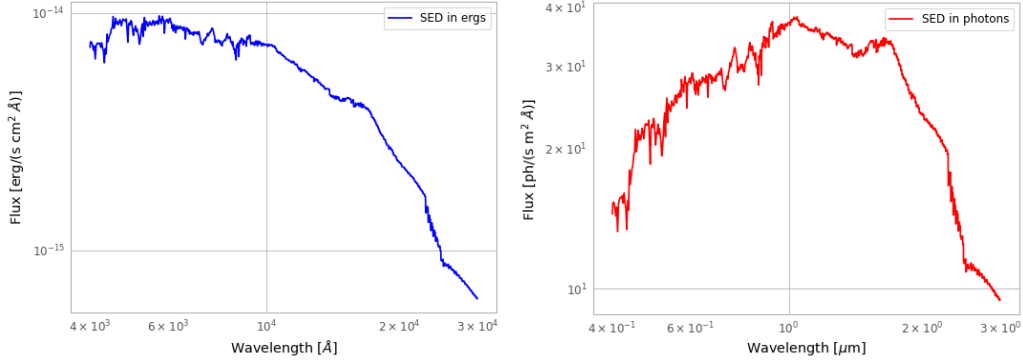


Figure 3.7: Comparison between the SED of NGC6090 expressed in  $[\text{erg/s/cm}^2/\text{\AA}]$  (left) and in  $[\text{photons/s/m}^2/\text{\AA}]$  (right), obtained from eq.3.19.

### 3.2.3 High-z Emission of Local LIRGs/ULIRGs

Using the method discussed in this chapter, it is possible to simulate the emission that local galaxies would have at high redshifts. Given our ultimate goal to simulate how HST-dark galaxies will be observed by ELT, we first consider their potentially local analogues, LIRGs and ULIRGs, and move them to redshifts in the range 2 to 4. In Figures 3.8 to 3.12 we show the SEDs of the five local galaxies (M82, Arp220, NGC6240, NGC6090, IRAS 20551-4250) shifted to higher redshifts.

Each figure contains the SED in  $[\mu\text{m}, \text{Jy}]$  of one galaxy at its true redshift (indicated for simplicity with  $z=0$  in the legend) and simulated at  $z=2$  (orange line), 3 (green line) and 4 (blue line). The vertical lines reported in all the plots indicate the four principal filters of MICADO (IJHKS) already shown in fig.2.5 and used for the simulations of both local LIRGs and HST-dark galaxies. The four broad bands are reported at their central wavelengths, i.e. at  $\lambda = 8000 \text{ \AA}$  (yellow),  $\lambda = 12480 \text{ \AA}$  (orange),  $\lambda = 16350 \text{ \AA}$  (red) and  $\lambda = 21450 \text{ \AA}$  (brown), respectively.

It should also be mentioned that, for a better comparison, all the plots are on the same scale, both in x and y axes, except for M82 in which the y-scale is slightly larger.

For each galaxy we report in a table the values of the fluxes obtained at the three different redshifts, 2, 3, 4, in the four different MICADO bands, I, J, H, Ks (tables 3.3, 3.4, 3.5, 3.6, 3.7 for M82, ARP220, NGC6240, NGC6090 and IRAS 20551-4250, respectively).

From the fluxes, we obtained the AB magnitudes (listed in the last column of the tables) using the formula:

$$m_{AB} = -2.5 \text{Log}_{10} F_{\lambda} [Jy] + 8.90 \quad (3.20)$$

### 3.3 HST-dark galaxies

Among all the HST-dark galaxy samples available in the literature, we choose to consider those found by [Gruppioni et al. \(2020\)](#) within the ALMA Large Program to INvestigate CII at Early Times (ALPINE), assuming that they are representative enough of the whole population of HST-dark sources. Of the whole catalogue of 56 sources serendipitously detected by ALMA in continuum, 12 ( $\sim 21\%$ ) do not present any optical or near-IR counterparts. Six of these HST-dark sources have been observed in the IRAC 3.6 or 4.5  $\mu m$  bands, while the remaining six have no counterpart at all. Of these unidentified sources, two have been detected as line emitters (likely [C II] emitters, [Loiacono et al. 2021](#)), while the four remaining are still unidentified (but compatible with the number of spurious sources expected). Therefore, excluding the last four sources, the survey finds 8 ( $\sim 14\%$  of the total catalogue) HST-dark galaxies.

For the six dark galaxies with an IRAC counterpart it was possible to find a photometric redshift through SED fitting by using the *Le Phare* software (also used in [Arnouts et al. 2002](#) and [Ilbert et al. 2006](#)), which performs a chi-squared fit by considering different templates, comprehending the semi-empirical library mentioned before (i.e. the SWIRE Template Library from [Polletta et al. 2007](#)). Their best fit SEDs are reported in [fig.3.13](#), finding a photometric redshifts range of [2.23–5.85], with an average value of  $z = 3.5$ .

In [tab.3.8](#) some important parameters found using best fit templates are reported: the IDs (taken from [Gruppioni et al. 2020](#)) of the mentioned six HST-dark galaxies, their photometric redshifts, their IR total luminosity (in the range [8-1000  $\mu m$ ]) and their estimated stellar masses.

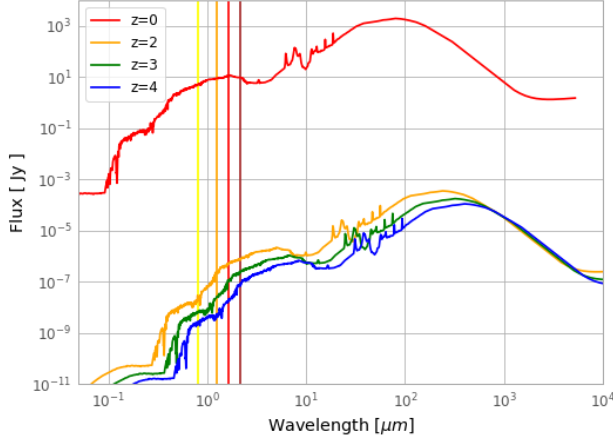


Figure 3.8: SEDs of M82 at different redshifts, as indicated in the legend, in units of  $[\mu m, Jy]$ . The vertical lines denote the central wavelengths of the IJHKs bands.

$z$	Band	$F_{\lambda}$ [ $erg/s/cm^2/\text{\AA}$ ]	$F_{\nu}$ [Jy]	$m_{AB}$
0	I	2.35e-12	5.01	7.15
	J	1.71e-12	8.88	6.53
	H	1.29e-12	11.53	6.25
	Ks	6.26e-13	9.61	6.44
2	I	1.08e-20	2.29e-8	27.99
	J	4.68e-20	2.43e-7	25.44
	H	5.77e-20	5.14e-7	24.62
	Ks	4.67e-20	7.16e-7	24.26
3	I	2.99e-21	6.39e-9	29.39
	J	4.95e-21	2.57e-8	27.87
	H	1.27e-20	1.13e-7	26.26
	Ks	1.61e-20	2.47e-7	25.42
4	I	1.26e-21	2.69e-9	30.33
	J	8.81e-22	4.58e-9	29.75
	H	2.38e-21	2.12e-8	28.09
	Ks	4.84e-21	7.43e-8	26.72

Table 3.3: Values of fluxes and AB magnitudes derived for M82 shifted at redshifts of 2, 3 and 4.

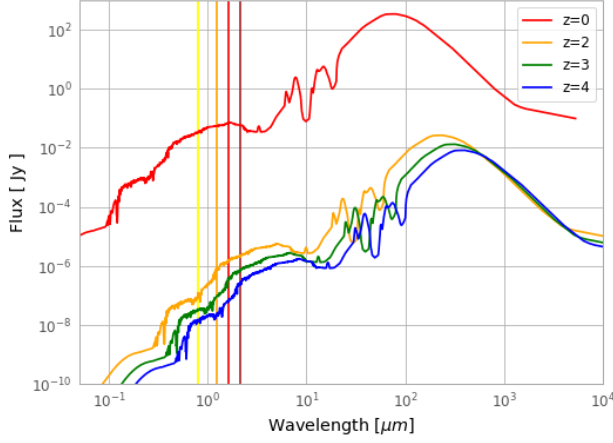


Figure 3.9: SEDs of ARP220 at different redshifts, as indicated in the legend, in units of  $[\mu m, Jy]$ . The vertical lines denote the central wavelengths of the IJHKs bands.

$z$	Band	$F_{\lambda}$ [ $erg/s/cm^2/\text{\AA}$ ]	$F_{\nu}$ [Jy]	$m_{AB}$
0	I	1.57e-14	0.034	12.59
	J	1.09e-14	0.056	12.02
	H	8.07e-15	0.072	11.76
	Ks	3.86e-15	0.059	11.97
2	I	4.71e-20	1.01e-7	26.39
	J	1.59e-19	8.24e-7	24.11
	H	1.76e-19	1.57e-6	23.41
	Ks	1.37e-19	2.10e-6	23.09
3	I	1.52e-20	3.22e-8	27.63
	J	1.91e-20	9.83e-8	26.42
	H	4.23e-20	3.78e-7	24.96
	Ks	4.90e-20	7.54e-7	24.21
4	I	7.32e-21	1.55e-8	28.42
	J	4.24e-21	2.20e-8	28.04
	H	8.58e-21	7.65e-8	26.69
	Ks	1.65e-20	2.53e-7	25.39

Table 3.4: Values of fluxes and AB magnitudes derived for ARP220 shifted at redshifts of 2, 3 and 4.

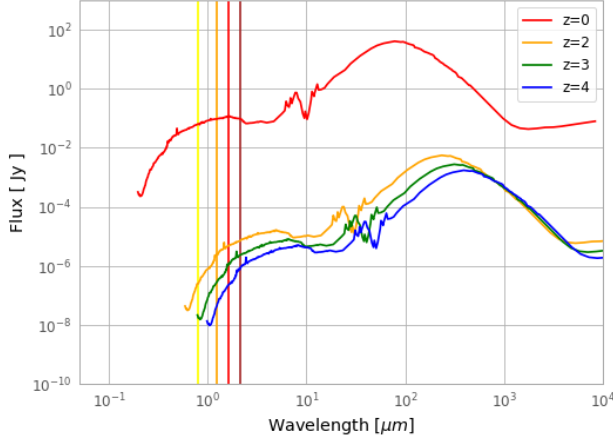


Figure 3.10: SEDs of NGC6240 at different redshifts, as indicated in the legend, in units of [ $\mu m$ , Jy]. The vertical lines denote the central wavelengths of the IJHKs bands.

$z$	Band	$F_{\lambda}$ [ $erg/s/cm^2/\text{\AA}$ ]	$F_{\nu}$ [Jy]	$m_{AB}$
0	I	3.02e-14	0.065	11.88
	J	1.87e-14	0.097	11.43
	H	1.30e-14	0.116	11.24
	Ks	6.22e-15	0.096	11.45
2	I	1.19e-19	2.53e-7	25.39
	J	4.94e-19	2.57e-6	22.88
	H	5.59e-19	4.99e-6	22.16
	Ks	4.77e-19	7.32e-6	21.74
3	I	9.18e-21	1.96e-8	28.17
	J	5.87e-20	3.05e-7	25.19
	H	1.38e-19	1.23e-6	23.67
	Ks	1.54e-19	2.37e-6	22.97
4	I			
	J	1.02e-20	5.28e-8	27.10
	H	2.62e-20	2.33e-7	25.48
	Ks	5.80e-20	8.89e-7	24.03

Table 3.5: Values of fluxes and AB magnitudes derived for NGC6240 shifted at redshifts of 2, 3 and 4. The values in the I-band at  $z=4$  are missing because the local template SED of this source is truncated in UV as one could note from the above figure 3.10.

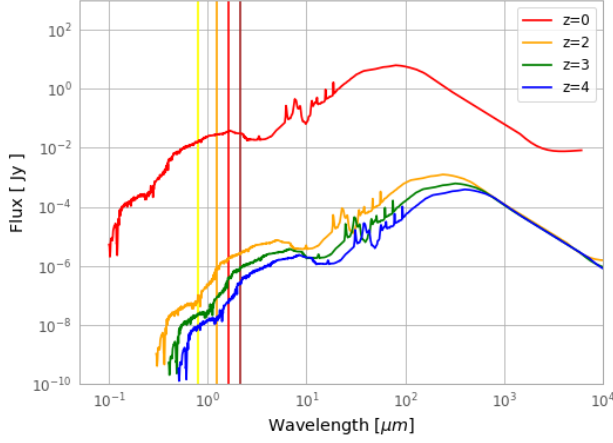


Figure 3.11: SEDs of NGC6090 at different redshifts, as indicated in the legend, in units of [ $\mu m$ , Jy]. The vertical lines denote the central wavelengths of the IJHKs bands.

$z$	Band	$F_{\lambda}$ [ $erg/s/cm^2/\text{\AA}$ ]	$F_{\nu}$ [Jy]	$m_{AB}$
0	I	7.54e-15	0.016	13.39
	J	5.51e-15	0.029	12.76
	H	4.17e-15	0.037	12.47
	Ks	2.02e-15	0.031	12.67
2	I	3.80e-20	8.10e-8	26.63
	J	1.65e-19	8.54e-7	24.07
	H	2.04e-19	1.82e-6	23.25
	Ks	1.65e-19	2.53e-6	22.89
3	I	1.07e-20	2.27e-8	28.01
	J	1.78e-20	9.20e-8	26.49
	H	4.49e-20	4.01e-7	24.89
	Ks	5.68e-20	8.74e-7	24.05
4	I	4.62e-21	9.80e-9	28.92
	J	3.11e-21	1.62e-8	28.38
	H	8.39e-21	7.49e-8	26.71
	Ks	1.71e-20	2.63e-7	25.35

Table 3.6: Values of fluxes and AB magnitudes derived for NGC6090 shifted at redshifts of 2, 3 and 4.

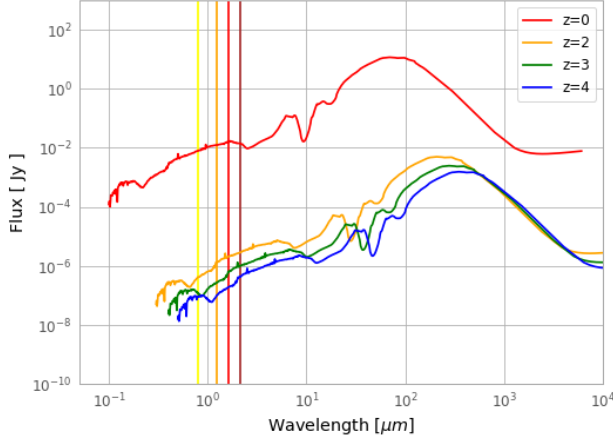


Figure 3.12: SEDs of IRAS 20551-4250 at different redshifts, as indicated in the legend, in units of  $[\mu m, Jy]$ . The vertical lines denote the central wavelengths of the IJHKs bands.

$z$	Band	$F_{\lambda}$ [ $erg/s/cm^2/\text{\AA}$ ]	$F_{\nu}$ [Jy]	$m_{AB}$
0	I	3.73e-15	0.008	14.15
	J	2.42e-15	0.013	13.66
	H	1.80e-15	0.016	13.39
	Ks	9.23e-16	0.014	13.52
2	I	1.99e-19	4.24e-7	24.83
	J	2.62e-19	1.37e-6	23.56
	H	2.35e-19	2.09e-6	23.10
	Ks	1.87e-19	2.87e-6	22.76
3	I	5.37e-20	1.15e-7	26.25
	J	5.39e-20	2.80e-7	25.28
	H	7.31e-20	6.52e-7	24.37
	Ks	6.63e-20	1.02e-6	23.88
4	I	4.14e-20	8.85e-8	26.53
	J	1.97e-20	1.02e-7	26.38
	H	2.21e-20	1.97e-7	25.67
	Ks	2.91e-20	4.47e-7	24.78

Table 3.7: Values of fluxes and AB magnitudes derived for IRAS 20551-4250 shifted at redshifts of 2, 3 and 4.

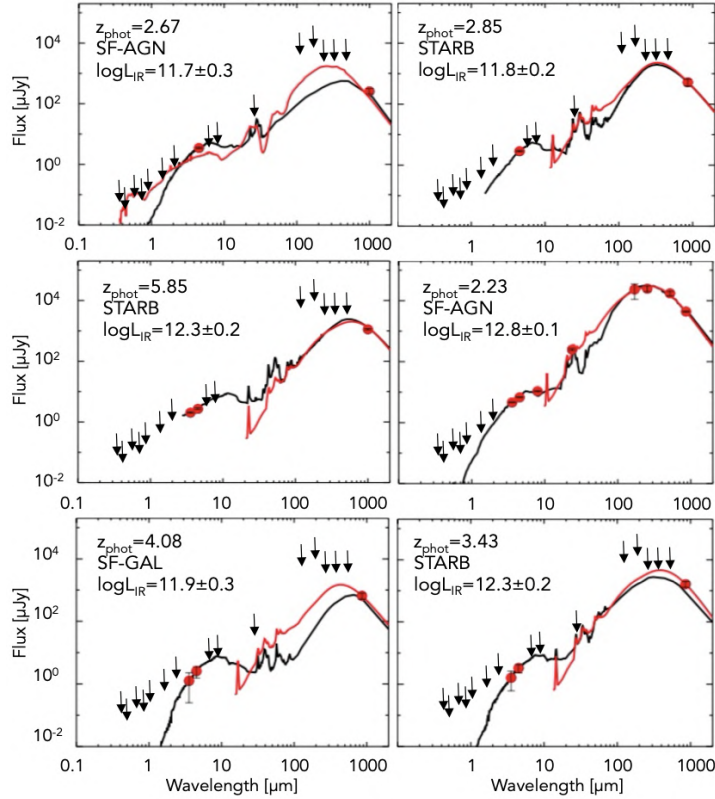


Figure 3.13: Observed SEDs for HST-dark galaxies, with their best fit template shown in black, while the template best reproducing the IR data (i.e. from 8 to 1000  $\mu m$  rest frame) is shown in red. The majority of best-fits are based only on the observed emission in IRAC and ALMA, combined with the  $3\sigma$  UV, optical, near- and far-IR  $3\sigma$  upper limits (Gruppioni et al., 2020).

We then verified that these HST-dark galaxies have similar SEDs to the local chosen sample. This can be done for each HST-dark galaxy, shifting the five local SEDs to the best-fit photometric redshift. Figures 3.14 to 3.19 show the ALPINE HST-dark galaxy SEDs compared to those of the local LIRGs/ULIRGs at the same redshift. Each figure contains the SED in units of [ $\mu m$ ,  $\mu Jy$ ] of one HST-dark galaxy compared to the five local LIRGs (indicated in the legend), together with the IRAC (3.6 and 4.5  $\mu m$ ) and ALMA (860  $\mu m$ ) data used to derive the best-fit SED. The vertical lines displayed in all plots indicate the central  $\lambda$  of the four filters IJHKs. In order to provide a better comparison, all the following plots are on the same scale,

ID	$z$	$Log L_{IR}$ [ $L_{\odot}$ ]	$Log M_{\star}$ [ $M_{\odot}$ ]
3	$2.67^{+1.1}_{-0.5}$	$11.70^{+0.06}_{-0.03}$	$10.22 \pm 0.2$
12	$2.85^{+1.2}_{-0.6}$	$11.79^{+0.04}_{-0.02}$	$10.14 \pm 0.2$
32	$5.84^{+0.5}_{-1.1}$	$12.31^{+0.02}_{-0.01}$	$10.97 \pm 0.1$
41	$2.23^{+0.3}_{-0.3}$	$12.81^{+0.04}_{-0.28}$	$10.51 \pm 0.3$
48	$4.08^{+0.8}_{-0.7}$	$11.85^{+0.02}_{-0.01}$	$10.70 \pm 0.2$
54	$3.43^{+1.1}_{-1.0}$	$12.32^{+0.02}_{-0.01}$	$10.06 \pm 0.2$

Table 3.8: IDs, redshifts, infrared luminosity and stellar mass estimated for the six HST-dark galaxies reported in fig.3.13.

both x and y.

It is crucial to note that all the sources have a SED shape similar to those of the local sample, confirming our initial assumption. Given that, one can speculate that also their morphologies could be.

We note that:

1. For some sources, the best-fit template SEDs cover the whole IJHKs spectral range (HST-dark galaxies with IDs 3, 41 and 48). Therefore the emission of these sources can be simulated simply using the best fit SED reported in black in fig.3.14, 3.17 and 3.18;
2. For other three sources (ID 12, 32 and 54 in fig.3.15, 3.16 and 3.19), the best-fit template does not cover the whole range covered by MICADO (i.e. the IJHKs bands). In order to be able to simulate these sources, and therefore predict how they would appear in that part of the spectrum, we thus used the most similar local template SED, properly normalised to the IRAC (3.6 and 4.5  $\mu m$ ) and ALMA (860  $\mu m$ ) fluxes. In the case of HST-dark 12, we used the SED of NGC6090, while for HST-dark 32 we used the SED of M82, and finally for HST-dark 54 we used the SED of IRAS 20551-4250.

In tables 3.9 to 3.14 we report the fluxes and AB magnitudes of the HST-dark galaxies in the four MICADO bands.

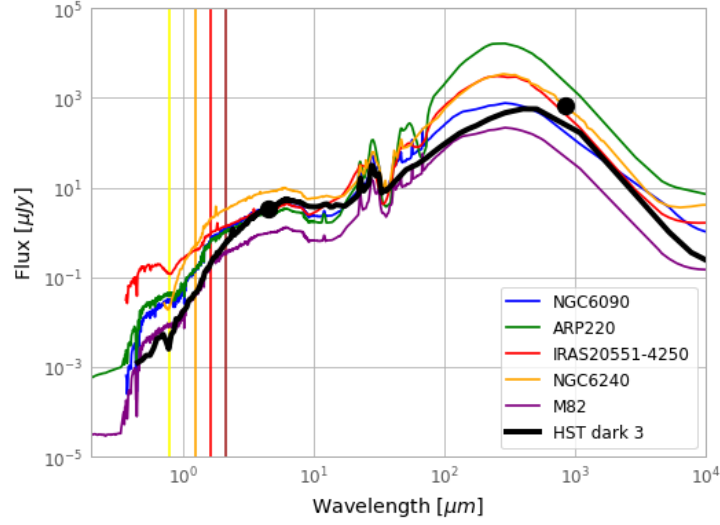


Figure 3.14: Comparison of the SEDs of local LIRGs with the SED of the HST-dark 3, in units of  $[\mu m, Jy]$ . The vertical lines represent the central wavelengths of IJHKs bands, while the black points are the IRAC ( $4.5 \mu m$ ) and ALMA ( $860 \mu m$ ) detections from Gruppioni et al. (2020).

$z$	Band	$F_\lambda$ [ $erg/s/cm^2/\text{\AA}$ ]	$F_\nu$ [Jy]	$m_{AB}$
2.67	I	2.38e-21	5.08e-9	29.63
	J	8.47e-21	4.40e-8	27.29
	H	2.20e-20	1.96e-7	25.67
	Ks	3.75e-20	5.75e-7	24.50

Table 3.9: Values of fluxes and AB magnitudes found for the HST-dark 3.

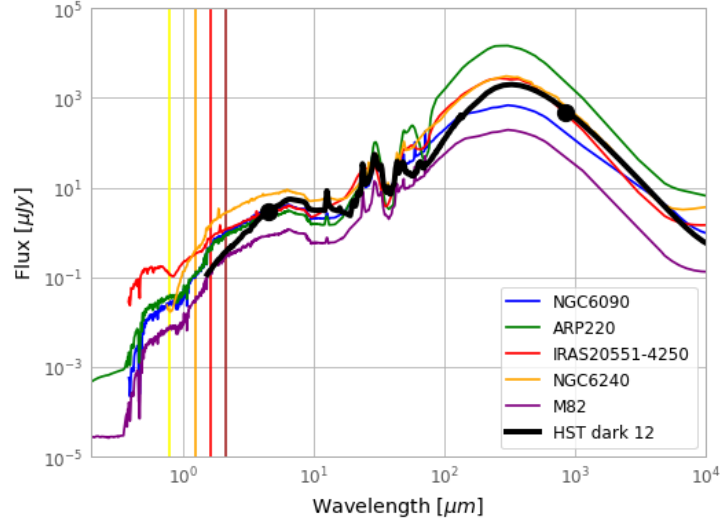


Figure 3.15: Comparison of the SEDs of local LIRGs with the SED of the HST-dark 12, in units of  $[\mu m, Jy]$ . The vertical lines represent the central wavelengths of IJHKs bands, while the black points are the IRAC ( $4.5 \mu m$ ) and ALMA ( $860 \mu m$ ) detections from [Gruppioni et al. \(2020\)](#).

$z$	Band	$F_\lambda$ [ $erg/s/cm^2/\text{\AA}$ ]	$F_\nu$ [Jy]	$m_{AB}$
2.85	I	1.50e-20	3.21e-8	27.63
	J	2.46e-20	1.28e-7	26.14
	H	6.00e-20	5.35e-7	24.58
	Ks	7.29e-20	1.12e-6	23.78

Table 3.10: Values of fluxes and AB magnitudes found for the HST-dark 12.

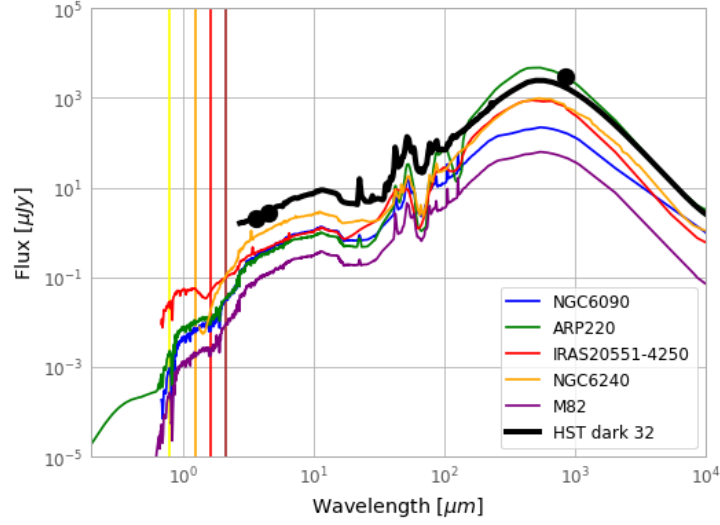


Figure 3.16: Comparison of the SEDs of local LIRGs with the SED of the HST-dark 32, in units of  $[\mu m, Jy]$ . The vertical lines represent the central wavelengths of IJHKs bands, while the black points are the IRAC (3.6 and  $4.5 \mu m$ ) and ALMA ( $860 \mu m$ ) detections from [Gruppioni et al. \(2020\)](#).

$z$	Band	$F_\lambda$ [ $erg/s/cm^2/\text{\AA}$ ]	$F_\nu$ [Jy]	$m_{AB}$
5.84	I	2.79e-21	5.96e-9	29.46
	J	8.44e-21	4.38e-8	27.29
	H	4.99e-21	4.45e-8	27.28
	Ks	1.31e-20	2.01e-7	25.64

Table 3.11: Values of fluxes and AB magnitudes found for the HST-dark 32.

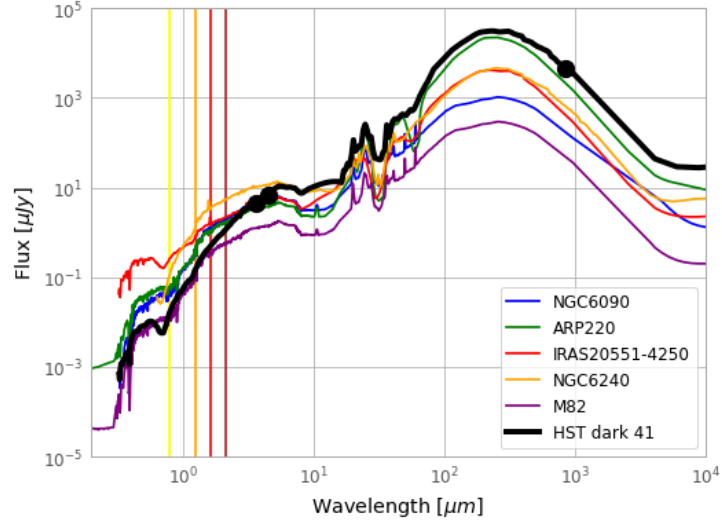


Figure 3.17: Comparison of the SEDs of local LIRGs with the SED of the HST-dark 41, in units of  $[\mu m, \text{Jy}]$ . The vertical lines represent the central wavelengths of IJHKs bands, while the black points are the IRAC (3.6 and 4.5  $\mu m$ ) and ALMA (860  $\mu m$ ) detections from Gruppioni et al. (2020).

$z$	Band	$F_\lambda$ [ $\text{erg/s/cm}^2/\text{\AA}$ ]	$F_\nu$ [Jy]	$m_{AB}$
2.23	I	7.53e-21	1.61e-8	28.39
	J	2.77e-20	1.44e-7	26.01
	H	5.59e-20	4.99e-7	24.66
	Ks	7.65e-20	1.18e-6	23.73

Table 3.12: Values of fluxes and AB magnitudes found for the HST-dark 41.

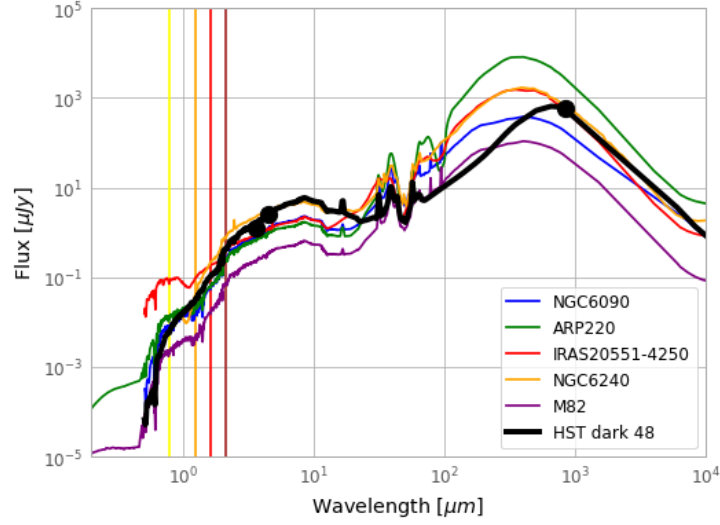


Figure 3.18: Comparison of the SEDs of local LIRGs with the SED of the HST-dark 48, in units of  $[\mu m, Jy]$ . The vertical lines represent the central wavelengths of IJHKs bands, while the black points are the IRAC (3.6 and 4.5  $\mu m$ ) and ALMA (860  $\mu m$ ) detections from [Gruppioni et al. \(2020\)](#).

$z$	Band	$F_\lambda$ [ $erg/s/cm^2/\text{\AA}$ ]	$F_\nu$ [Jy]	$m_{AB}$
4.08	I	3.20e-21	6.82e-9	29.32
	J	6.28e-21	3.26e-8	27.62
	H	1.16e-20	1.04e-7	26.36
	Ks	2.91e-20	4.47e-7	24.78

Table 3.13: Values of fluxes and AB magnitudes found for the HST-dark 48.

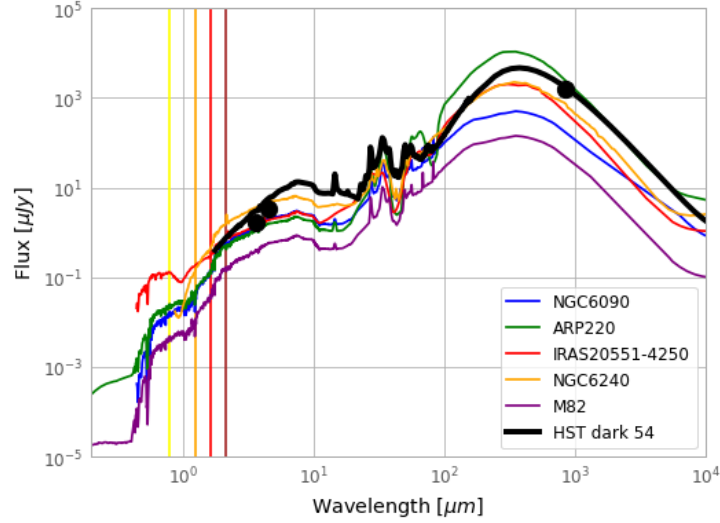


Figure 3.19: Comparison of the SEDs of local LIRGs with the SED of the HST-dark 54, in units of  $[\mu m, \text{Jy}]$ . The vertical lines represent the central wavelengths of IJHKs bands, while the black points are the IRAC (3.6 and 4.5  $\mu m$ ) and ALMA (860  $\mu m$ ) detections from [Gruppioni et al. \(2020\)](#).

$z$	Band	$F_\lambda$ [ $\text{erg/s/cm}^2/\text{\AA}$ ]	$F_\nu$ [Jy]	$m_{AB}$
3.43	I	1.30e-19	2.78e-7	25.29
	J	7.86e-20	4.08e-7	24.87
	H	7.10e-20	6.33e-7	24.40
	Ks	1.01e-19	1.54e-6	23.43

Table 3.14: Values of fluxes and AB magnitudes found for the HST-dark 54.

The next chapter is entirely dedicated to the results of our simulations. As already mentioned in section 3.1, the optical-NIR morphologies of the HST-dark galaxies are unknown because they are too faint to be detected or too small to be resolved with the available instruments (see IRAC images in fig.1.8 with a resolution of  $\sim 2''$ ). Therefore, the choice of the images to be used to simulate these sources is somewhat arbitrary. However, since their best-fit templates resemble the SEDs of local LIRGs, we assume that also their morphologies may be similar, and use the local LIRGs images to simulate HST-dark galaxies.

We thus associated to each HST-dark galaxy the morphology of the local galaxy whose SED more closely matches the best-fit template. We therefore considered NGC6090 for HST-dark 3 and HST-dark 12, M82 for HST-dark 32, Arp220 for HST-dark 41, NGC6240 for HST-dark 48 and IRAS 20551-4250 for HST-dark 54.

Although for this thesis we adopt local ULIRGs/LIRGs to simulate the morphologies of HST-dark galaxies, future work may implement different assumptions, considering for instance different galaxy types (from ellipticals to spirals) and also dwarfs galaxies, challenging further more the resolution power and the versatility of the system MORFEO+MICADO. Furthermore, high-redshift sources are believed to be typically more compact than low-redshift/local ones. Therefore, one could consider an additional shrinking, other than the scaling relation for the angular dimension in eq.3.4, that account for the fact that high-redshift galaxies are intrinsically more compact and smaller.

In the end, the assumed morphologies, SEDs, and various parameters described in sec.3 are inputed into the *simcado.run* task to generate the MORFEO+MICADO simulated images. We simulated the middle chip (of the 9 in total) of MICADO in the four bands IJHKs, adopting the PSFs for the MCAO mode and a pixel size of 4 *mas*. In the simulations, the total exposure time was divided into individual exposures of 300 s duration (*obs-dit=300*).

# Chapter 4

## Results

### 4.1 Local LIRGs

In this section, we report the simulation results obtained for a local sample of LIRGs shifted at different redshifts, as described in section 3.2. Figures 4.1 to 4.15 show the MORFEO+MICADO simulated images. In particular, the first column shows real HST images of local LIRGs observed at different wavelengths, while the second column shows how these galaxies would be seen by ELT at increasing higher redshifts. Because of the behaviour of angular size with distance, described by relation 3.4, local sources with typical apparent size of several tens of *arcsec* are observed to have angular dimensions of less than 1-2 *arcsec* at  $z > 2$ . For a better visualization of the galaxies' morphological details, we provide in the third column zoomed-in portions of the simulated images.

Therefore, each figure refers to a simulated redshift and is structured into a grid of images with the following meaning:

- The first column reports rest-frame HST images;
- The second column reports the simulation results;
- The third column reports a zoomed central portion of the simulated image, with a FoV small enough to allow for image details to be visible;
- Every row reports the simulation done in a different MICADO band: I, J, H and Ks, from top to bottom;

- For each image, the filter central wavelength or the photometric band are reported on the top left corner, the simulated magnitude on the top right corner, and the displayed angular scale on the bottom.

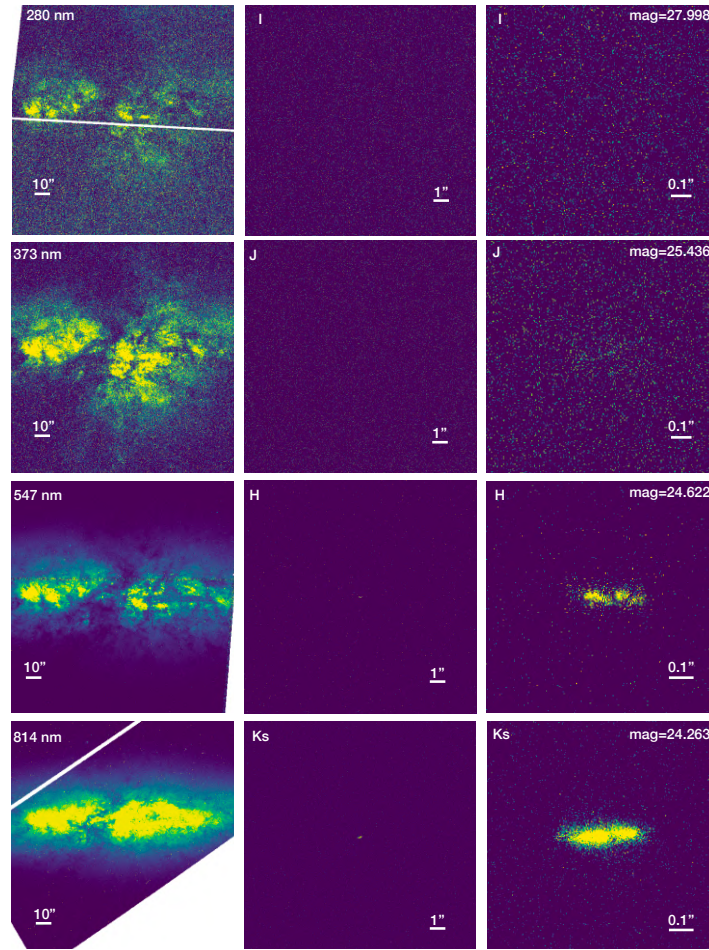


Figure 4.1: SIMCADO simulations for a galaxy like M82 shifted at redshift 2. The first, second and third columns correspond to a FoV of  $160'' \times 160''$ ,  $16.4'' \times 16.4''$ , and  $1'' \times 1''$ , respectively, with the first column being the local observed galaxy, and the second and third ones corresponding to the high-redshift simulations. For each image, we provide the HST filter central wavelength or the MICADO band (top left), the displayed angular scale (bottom), and the magnitude of the simulated galaxy (third column, top right). The images were obtained adopting a total exposure time of  $\sim 8.3$  h.

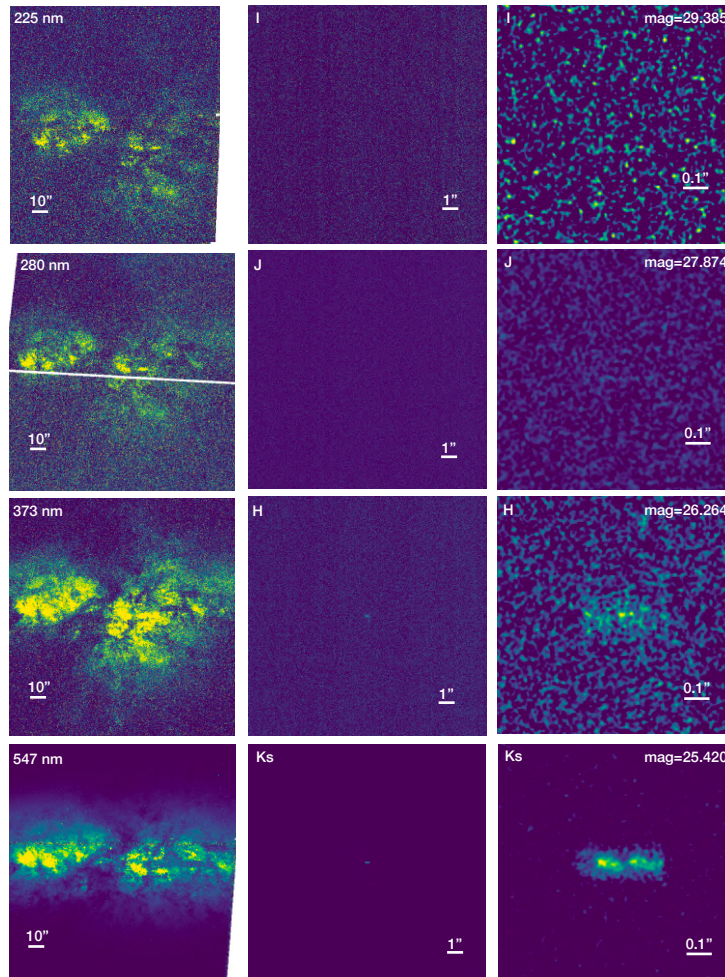


Figure 4.2: Same as in fig.4.1, with M82 shifted at  $z=3$ . The simulated images were obtained adopting a total exposure time of  $\sim 10.4$  h. In order to enhance low signal-to-noise features, a Gaussian smoothing with a radius of 3 pixels has been applied to the simulations.

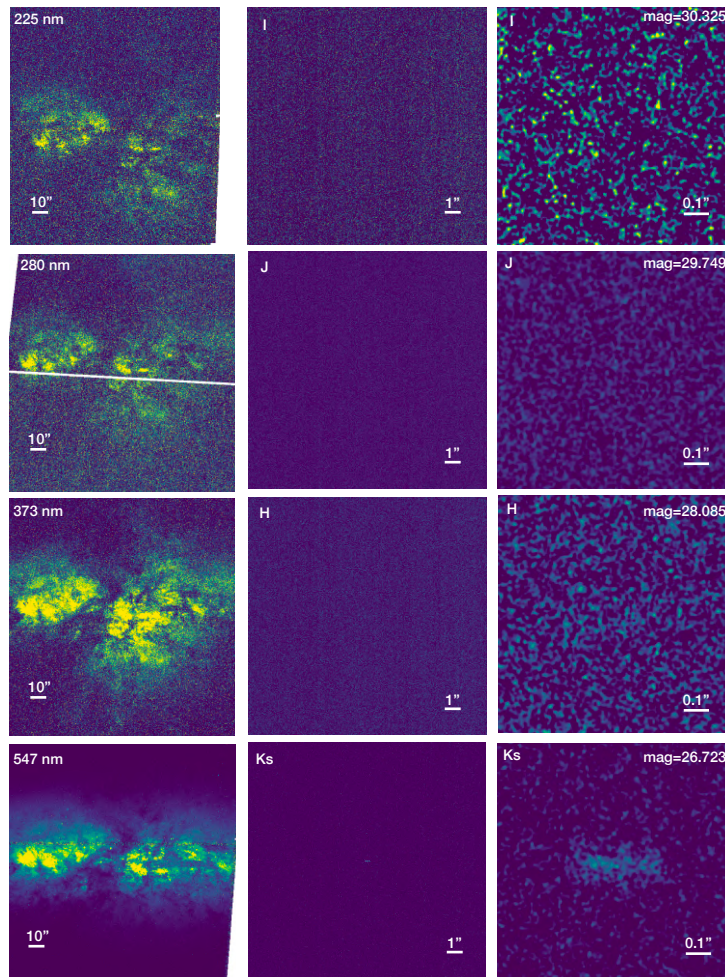


Figure 4.3: Same as in fig.4.1, with M82 shifted at  $z=4$ . The simulated images were obtained adopting a total exposure time of  $\sim 12.5$  h. In order to enhance low signal-to-noise features, a Gaussian smoothing with a radius of 3 pixels has been applied to the simulations.

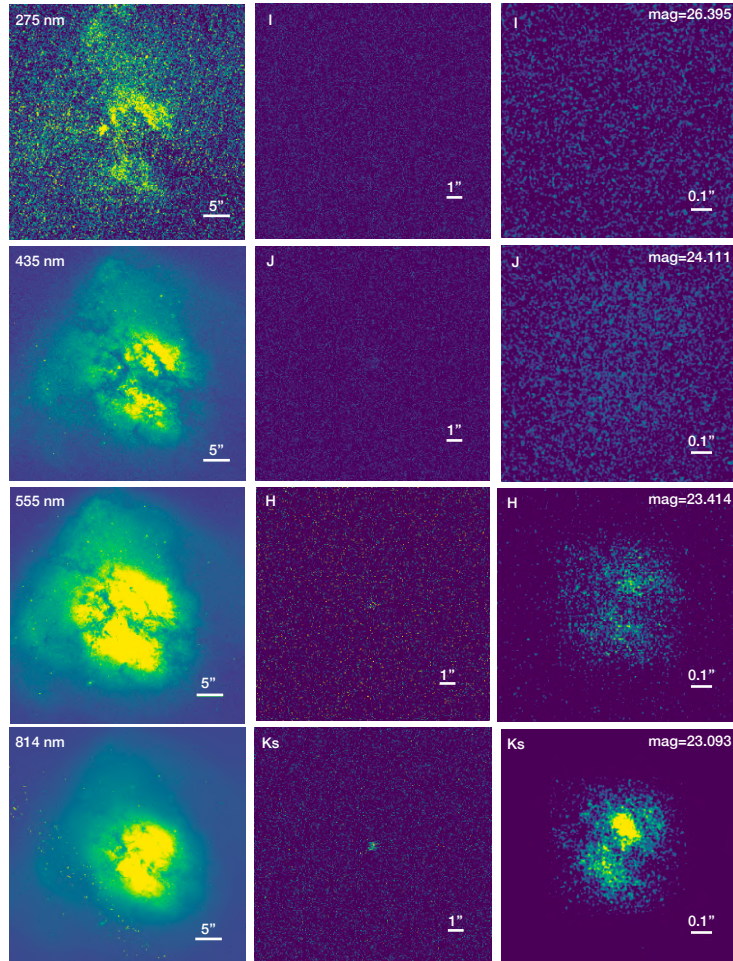


Figure 4.4: SIMCADO simulations for a galaxy like ARP220 shifted at  $z=2$ . The first, second and third columns correspond to a FoV of  $45'' \times 45''$ ,  $16.4'' \times 16.4''$ , and  $1.2'' \times 1.2''$ , respectively, with the first column being the local observed galaxy, and the second and third ones corresponding to the high-redshift simulations. For each image, we provide the HST filter central wavelength or the MICADO band (top left), the displayed angular scale (bottom), and the magnitude of the simulated galaxy (third column, top right). The images were obtained adopting a total exposure time of  $\sim 8.3$  h. In order to enhance low signal-to-noise features, a Gaussian smoothing with a radius of 2 pixels has been applied to the simulations.

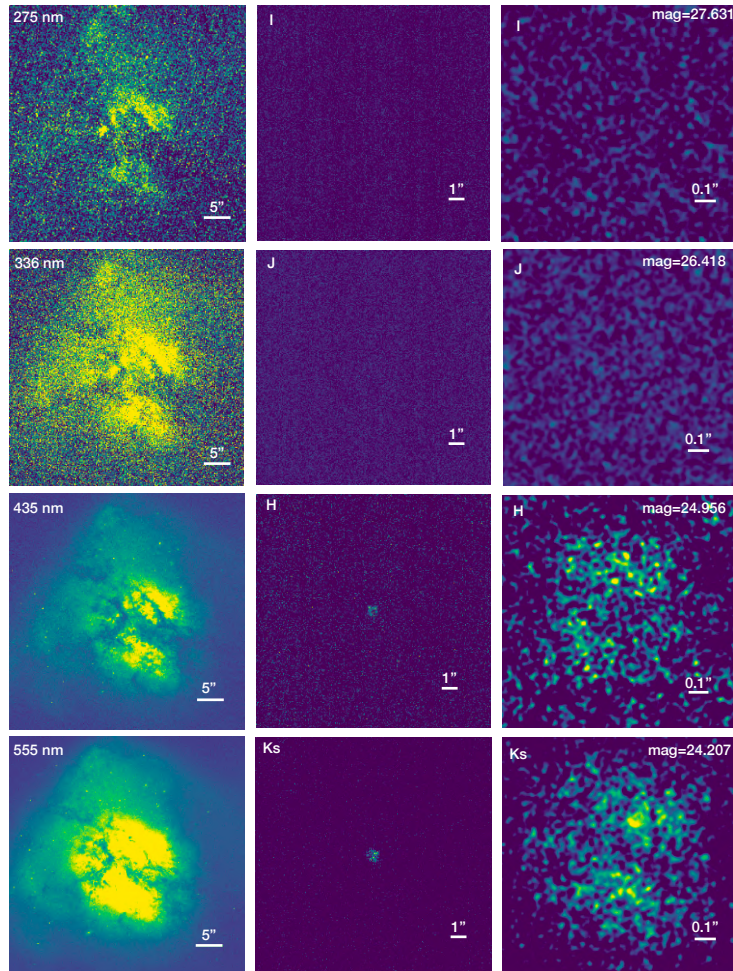


Figure 4.5: Same as in fig.4.4, with ARP220 shifted at  $z=3$ . The simulated images were obtained adopting a total exposure time of  $\sim 10.4$  h. In order to enhance low signal-to-noise features, a Gaussian smoothing with a radius of 5 pixels has been applied to the simulations.

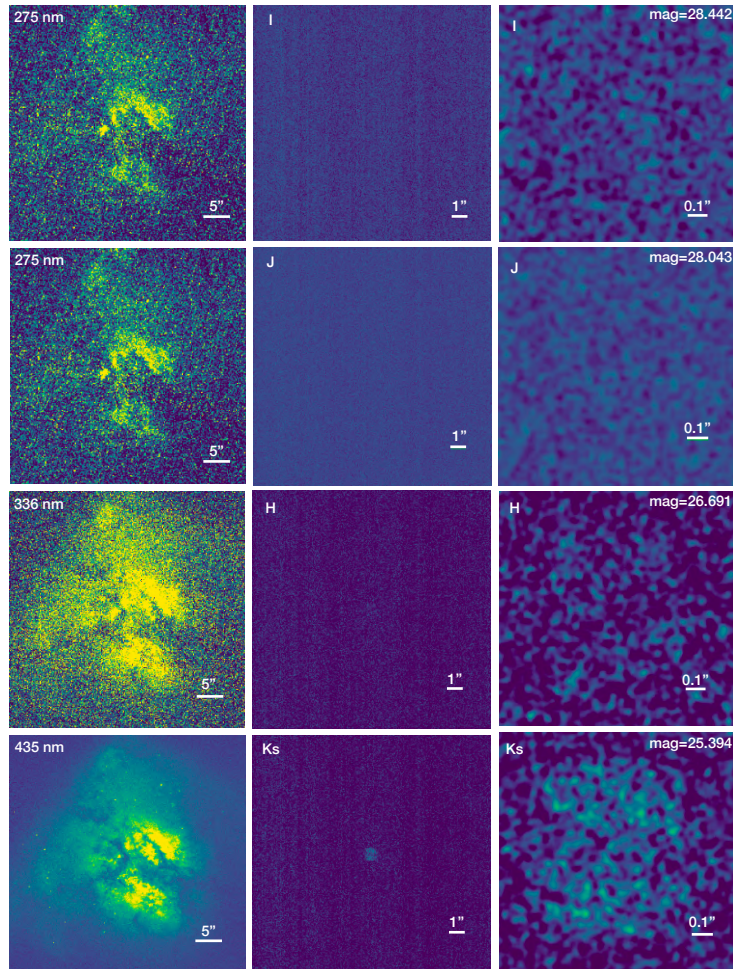


Figure 4.6: Same as in fig.4.4, with ARP220 shifted at  $z=4$ . The simulated images were obtained adopting a total exposure time of  $\sim 12.5$  h. In order to enhance low signal-to-noise features, a Gaussian smoothing with a radius of 7 pixels has been applied to the simulations.

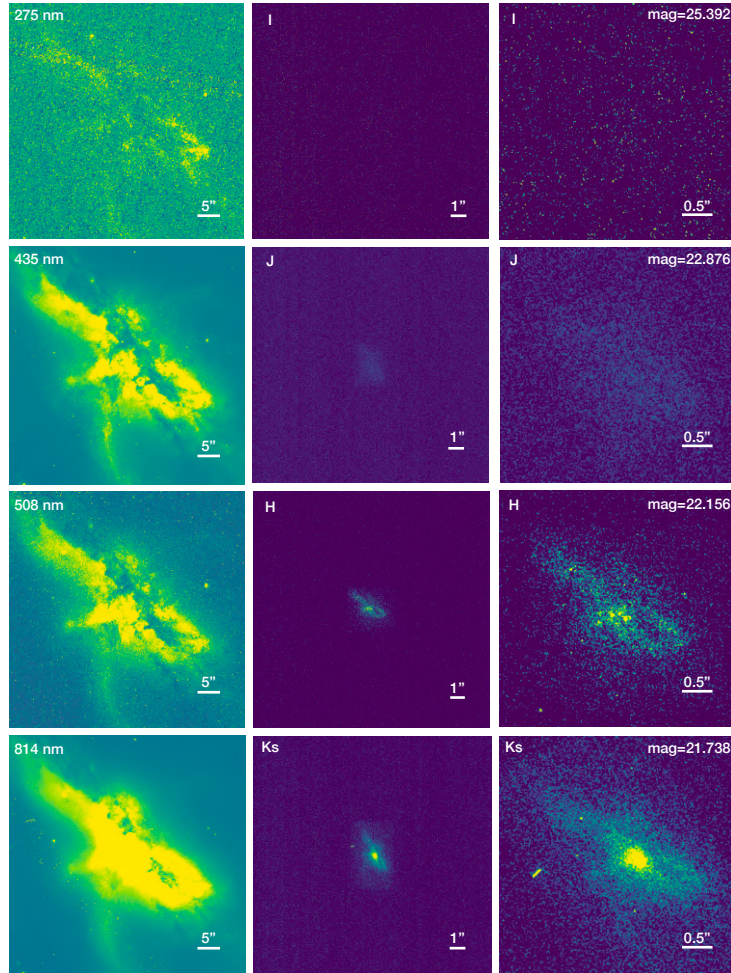


Figure 4.7: SIMCADO simulations for a galaxy like NGC6240 shifted at  $z=2$ . The first, second and third columns correspond to a FoV of  $55'' \times 55''$ ,  $16.4'' \times 16.4''$ , and  $4'' \times 4''$ , respectively, with the first column being the local observed galaxy, and the second and third ones corresponding to the high-redshift simulations. For each image, we provide the HST filter central wavelength or the MICADO band (top left), the displayed angular scale (bottom), and the magnitude of the simulated galaxy (third column, top right). The images were obtained adopting a total exposure time of  $\sim 8.3$  h. In order to enhance low signal-to-noise features, a Gaussian smoothing with a radius of 4 pixels has been applied to the simulations.

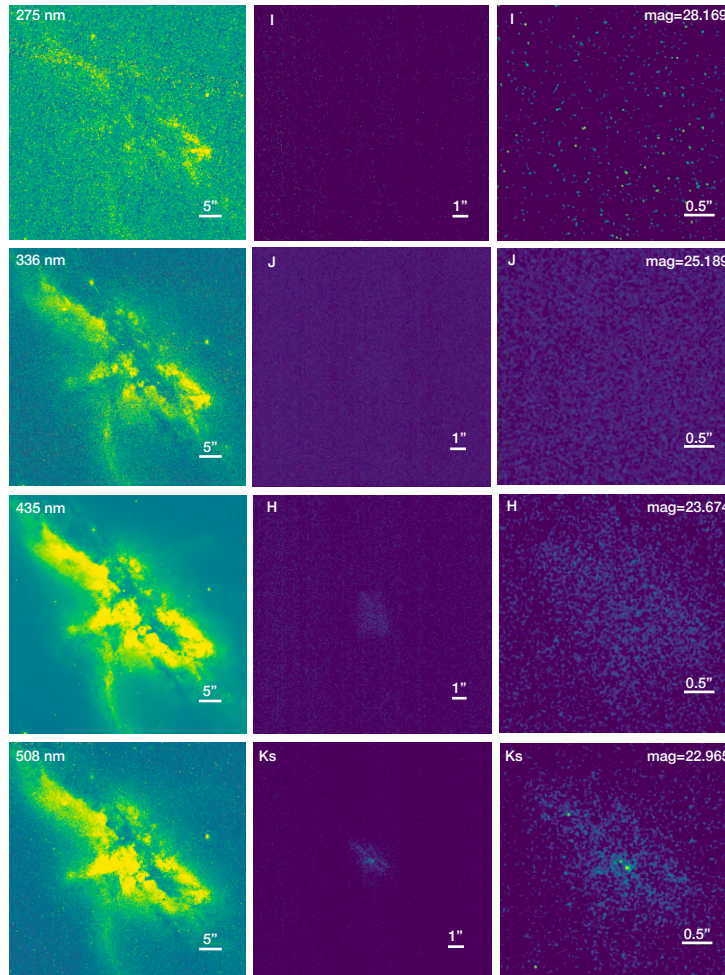


Figure 4.8: Same as in fig.4.7, with NGC6240 shifted at  $z=3$ . The simulated images were obtained adopting a total exposure time of  $\sim 10.4$  h. In order to enhance low signal-to-noise features, a Gaussian smoothing with a radius of 7 pixels has been applied to the simulations.

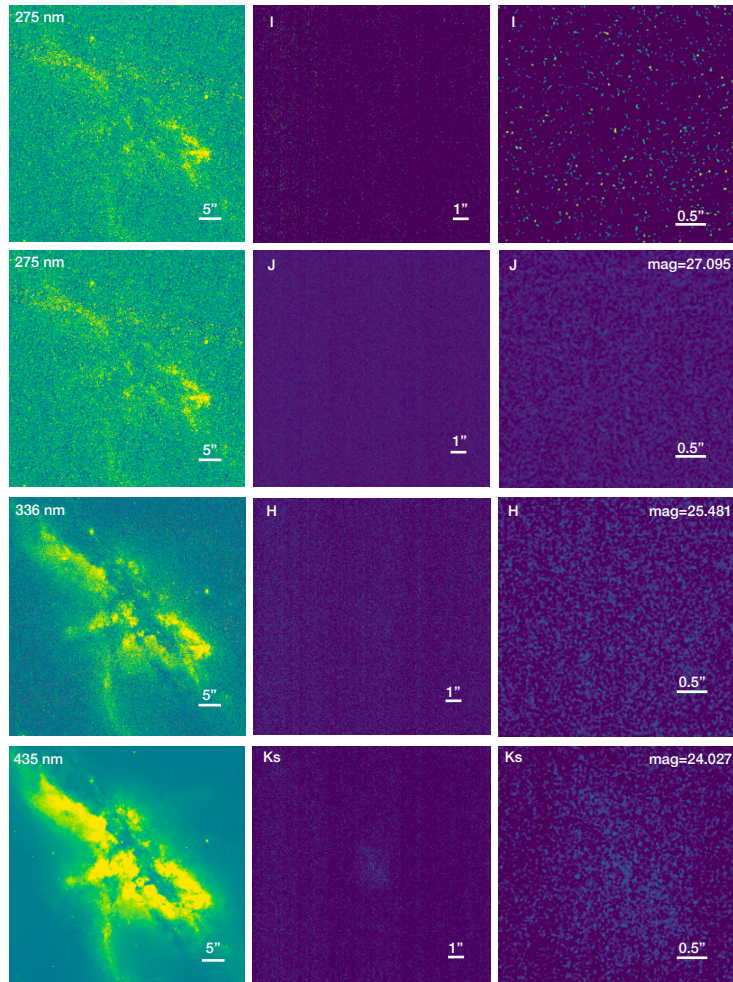


Figure 4.9: Same as in fig.4.7, with NGC6240 shifted at  $z=4$ . The simulated images were obtained adopting a total exposure time of  $\sim 12.5$  h. In order to enhance low signal-to-noise features, a Gaussian smoothing with a radius of 7 pixels has been applied to the simulations.

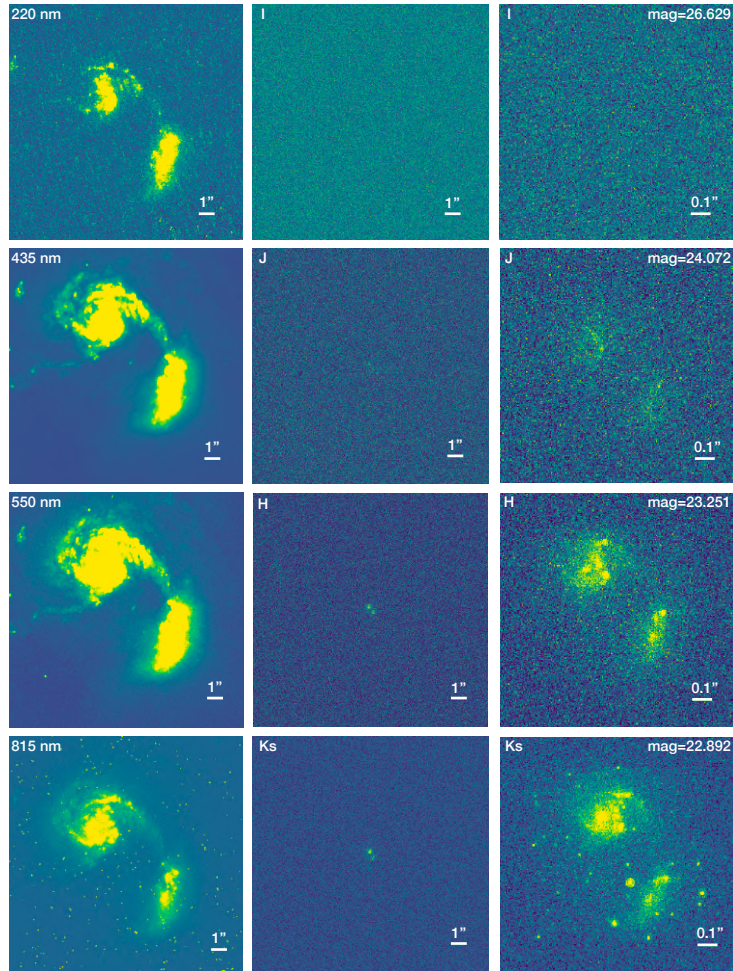


Figure 4.10: SIMCADO simulations for a galaxy like NGC6090 shifted at  $z=2$ . The first, second and third columns correspond to a FoV of  $16.4'' \times 16.4''$ ,  $16.4'' \times 16.4''$ , and  $1.2'' \times 1.2''$ , respectively, with the first column being the local observed galaxy, and the second and third ones corresponding to the high-redshift simulations. For each image, we provide the HST filter central wavelength or the MICADO band (top left), the displayed angular scale (bottom), and the magnitude of the simulated galaxy (third column, top right). The images were obtained adopting a total exposure time of  $\sim 6.7$  h. In order to enhance low signal-to-noise features, a Gaussian smoothing with a radius of 4 pixels has been applied to the simulations.

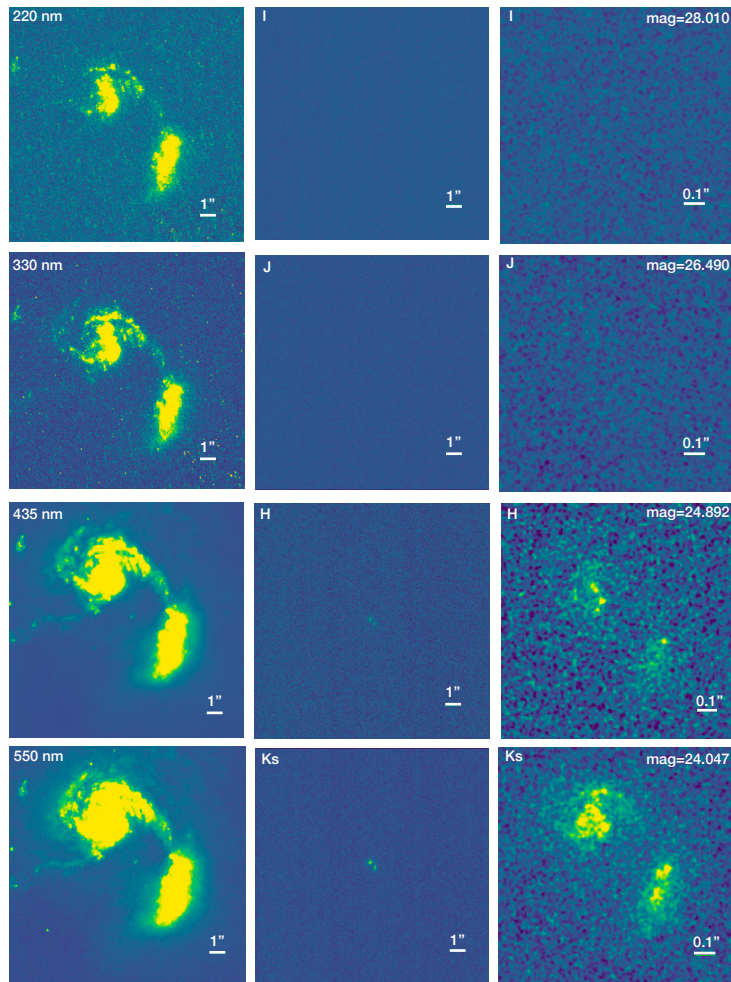


Figure 4.11: Same as in fig.4.10, with NGC6090 shifted at  $z=3$ . The simulated images were obtained adopting a total exposure time of  $\sim 8.3$  h. In order to enhance low signal-to-noise features, a Gaussian smoothing with a radius of 3 pixels has been applied to the simulations.

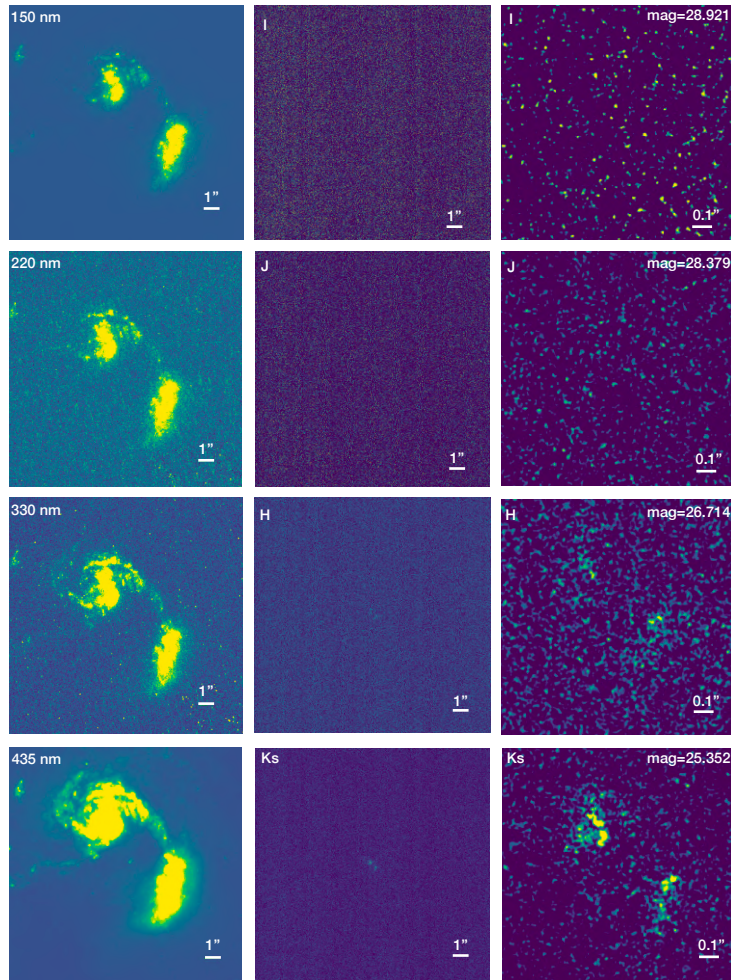


Figure 4.12: Same as in fig.4.10, with NGC6090 shifted at  $z=4$ . The simulated images were obtained adopting a total exposure time of  $\sim 12.5$  h. In order to enhance low signal-to-noise features, a Gaussian smoothing with a radius of 6 pixels has been applied to the simulations.

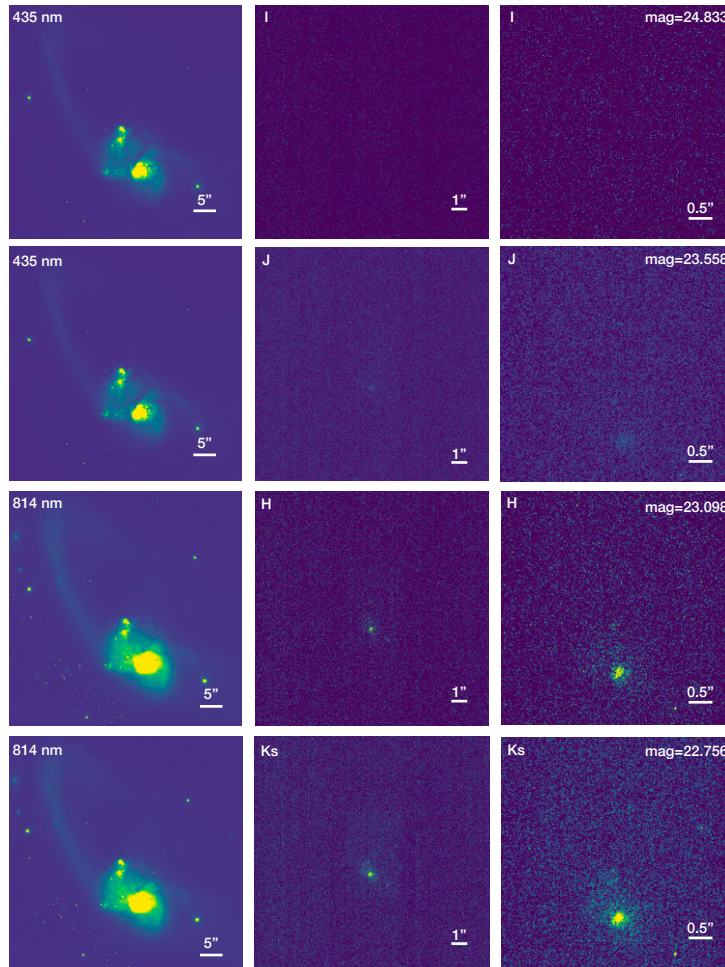


Figure 4.13: SIMCADO simulations for a galaxy like IRAS 20551-4250 shifted at  $z=2$ . The first, second and third columns correspond to a FoV of  $55'' \times 55''$ ,  $16.4'' \times 16.4''$ , and  $5'' \times 5''$ , respectively, with the first column being the local observed galaxy, and the second and third ones corresponding to the high-redshift simulations. For each image, we provide the HST filter central wavelength or the MICADO band (top left), the displayed angular scale (bottom), and the magnitude of the simulated galaxy (third column, top right). The images were obtained adopting a total exposure time of  $\sim 8.3$  h. In order to enhance low signal-to-noise features, a Gaussian smoothing with a radius of 3 pixels has been applied to the simulations.

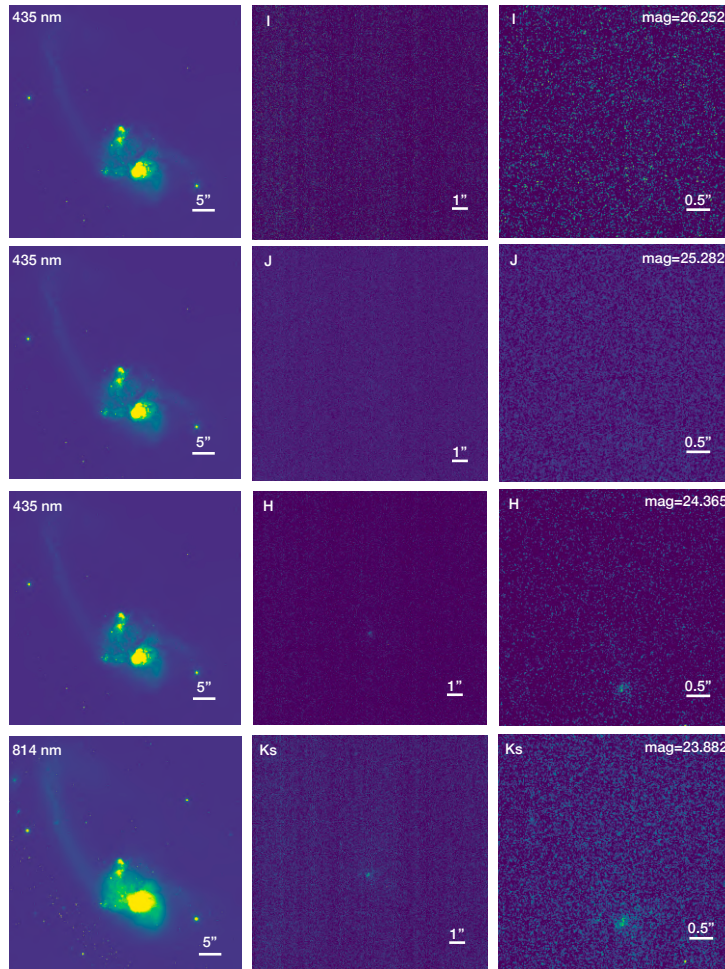


Figure 4.14: Same as in fig.4.13, with IRAS 20551-4250 shifted at  $z=3$ . The simulated images were obtained adopting a total exposure time of  $\sim 10.4$  h. In order to enhance low signal-to-noise features, a Gaussian smoothing with a radius of 4 pixels has been applied to the simulations.

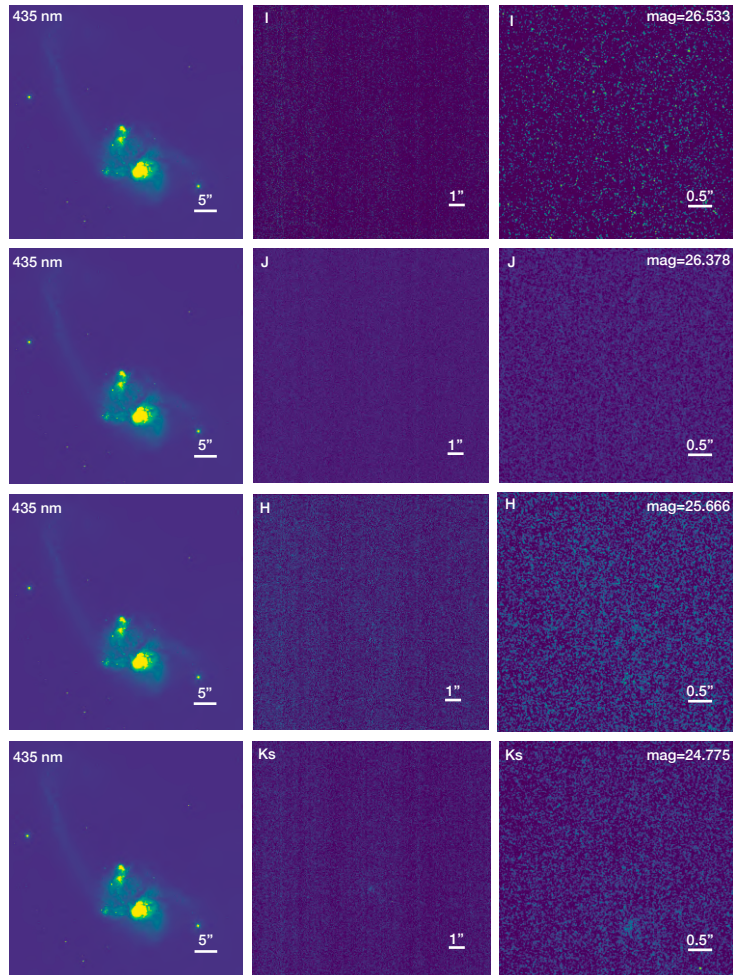


Figure 4.15: Same as in fig.4.13, with IRAS 20551-4250 shifted at  $z=4$ . The simulated images were obtained adopting a total exposure time of  $\sim 12.5$  h. In order to enhance low signal-to-noise features, a Gaussian smoothing with a radius of 5 pixels has been applied to the simulations.

The local HST images show very well that the five chosen LIRGs/ULIRGs are characterised by dusty, obscured and irregular shapes; indeed, all the galaxies exhibit a highly distorted morphology, characterized by the presence of elongated tidal tails indicative of an intermediate stage of merging. This is particularly evident in the images of NGC6090 and IRAS 20551-4250, for example.

As our goal is to evaluate the potentialities offered by ELT high resolution in understanding galaxy properties in the high-redshift Universe, it is worth to comment our results on the simulated images in terms of physical information (e.g., global galaxy morphology, spatial distribution of star forming knots, presence of multiple systems, etc.) that future MORFEO+MICADO observations will be able to provide. Fig.4.10, for example, shows that MORFEO+MICADO will allow us, for a galaxy like the LIRG NGC6090, to recover its peculiar and merger-like morphology. Indeed, individual star-forming regions (with a scale of  $\sim 0.16$  kpc) in this galaxy would be well identified up to redshift 4, as shown in fig.4.12. This is an unachievable result for the current instrumentation and will be possible only thanks to the advent of the ELT, which therefore will bring a revolution in our understanding of the high-redshift Universe, allowing to characterize distant sources with unprecedented detail. In our simulations we note that these galaxies will be un-detected in the shorter-wavelength bands (i.e. I and J) at  $z > 2$ . This is somehow expected since the higher the redshift, the shorter the sampled rest-frame wavelength for a given observation band; indeed, at  $z \sim 4$ , the I and J band sample the FUV and NUV rest-frame wavelengths, respectively (see tab.3.1), where the LIRG spectrum is known to be dimmed and extinguished by dust. This is quantified by the magnitudes provided in tables 3.3 to 3.7 in the previous chapter which, for LIRGs shifted at  $z=4$ , are in the range 26-30 (AB mag) in the I and J bands. In addition, the local HST images in the UV band have a worse quality than the optical ones, with significant background noise which propagates into the simulations. On the other hand, we are particularly able to observe and resolve the galaxies in the Ks band, which samples the rest-frame optical spectrum. Indeed, the H and (especially) the Ks bands result the most effective ones to study obscured galaxies in the high-redshift Universe with the ELT, permitting us to resolve the morphologies of the HST-dark galaxies (see fig.4.10, 4.11, 4.12).

Finally, we note that compact sources can be easily detected, and their morphologies characterized with high detail, up to redshift 4, while extended and more diffuse systems tend to be lost due to their low surface brightness

(see section 4.3). Therefore, our SIMCADO simulations confirm that surface brightness is a crucial factor for a source detectability with a high spatial resolution facility such as MORFEO+MICADO on ELT (further discussions on section 4.3).

In conclusion, our work suggests that the optimal solution to observe the high-redshift Universe with MORFEO+MICADO is using the H-Ks bands to resolve and characterize smaller and compact sources.

## 4.2 HST-dark galaxies

After demonstrating how local LIRGs would appear at high redshift with the capabilities of the ELT, now we proceed to report the simulation results for the HST-dark galaxies discussed in section 3.3. In particular, every source has been simulated in each of the four broad bands of MICADO (IJHKs) and at its best-fit photometric redshift.

As discussed in the previous chapter, for each HST dark galaxy, we assumed the morphology of the local galaxy whose SED is more similar to the HST-dark best fit template; more specifically, we adopted the HST rest frame image corresponding to the MICADO band of observation at the redshift of the HST-dark system. We note that the morphology of NGC6090 was associated with two HST-dark sources, i.e. those with IDs 3 and 12. Therefore, as these two sources also have a comparable SED and photometric redshift, we choose to report the results only for one of the two (i.e. HST-dark galaxy 12) in order to avoid redundant images and considerations.

As anticipated in the last section, all the simulation results are reported in tables of images defined in the same way as the LIRGs' ones.

Figures 4.16 to 4.20 show the simulation results obtained for each HST-dark galaxy, with a fixed exposure time of  $\sim 17$  hours.

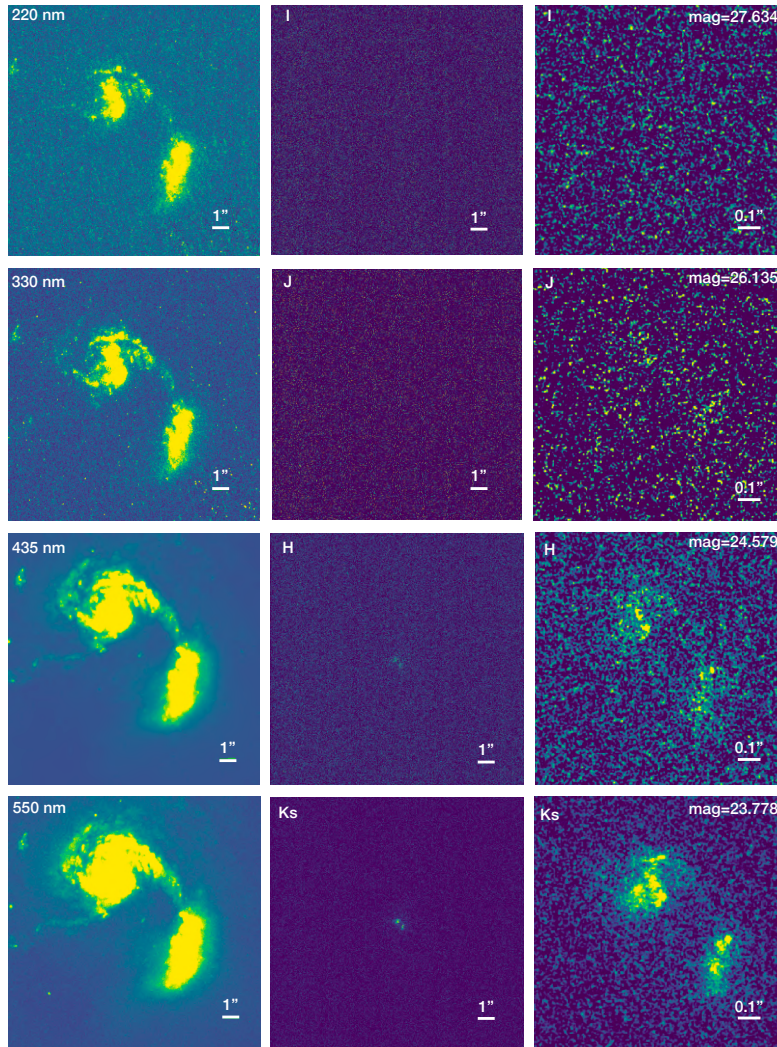


Figure 4.16: SIMCADO simulations for the HST-dark galaxy with ID 12 at  $z=2.85$ . The first, second and third columns correspond to a FoV of  $16.4'' \times 16.4''$ ,  $16.4'' \times 16.4''$ , and  $1.2'' \times 1.2''$ , respectively. For each image, we provide the HST filter central wavelength or the MICADO band (top left), the displayed angular scale (bottom), and the magnitude of the simulated galaxy (third column, top right). The images were obtained adopting a total exposure time of  $\sim 16.7$  h. In order to enhance low signal-to-noise features, a Gaussian smoothing with a radius of 2 pixels has been applied to the simulations.

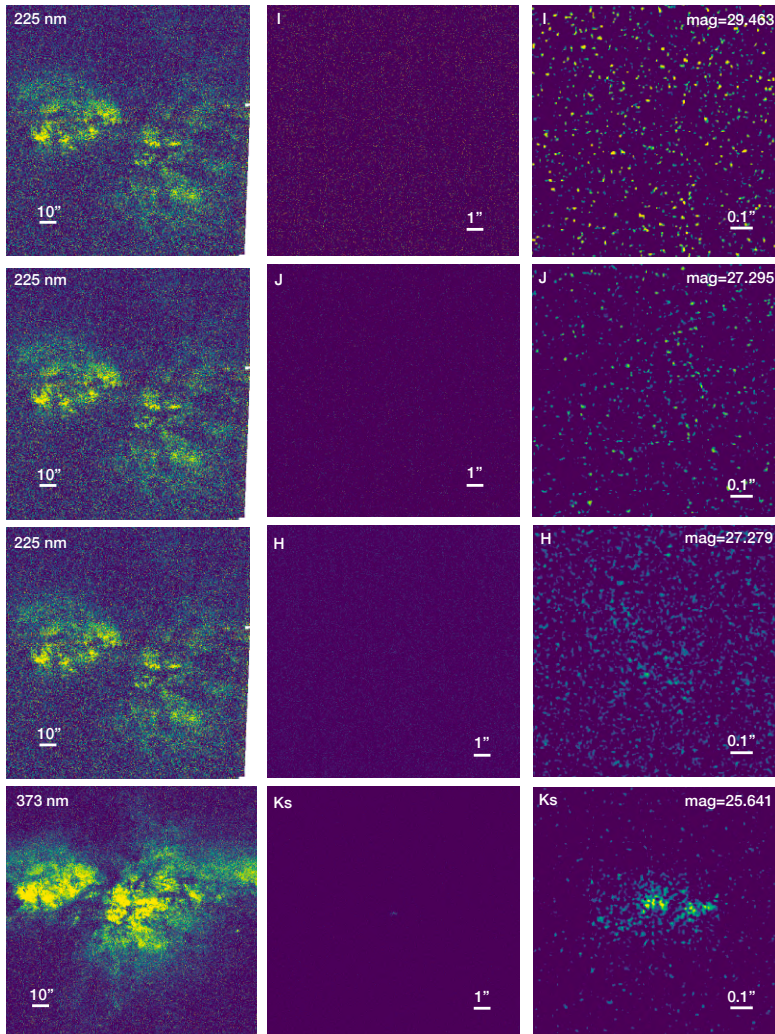


Figure 4.17: SIMCADO simulations for the HST-dark galaxy with ID 32 at  $z=5.84$ . The first, second and third columns correspond to a FoV of  $160'' \times 160''$ ,  $16.4'' \times 16.4''$ , and  $1'' \times 1''$ , respectively. For each image, we provide the HST filter central wavelength or the MICADO band (top left), the displayed angular scale (bottom), and the magnitude of the simulated galaxy (third column, top right). The images were obtained adopting a total exposure time of  $\sim 16.7$  h. In order to enhance low signal-to-noise features, a Gaussian smoothing with a radius of 2 pixels has been applied to the simulations.

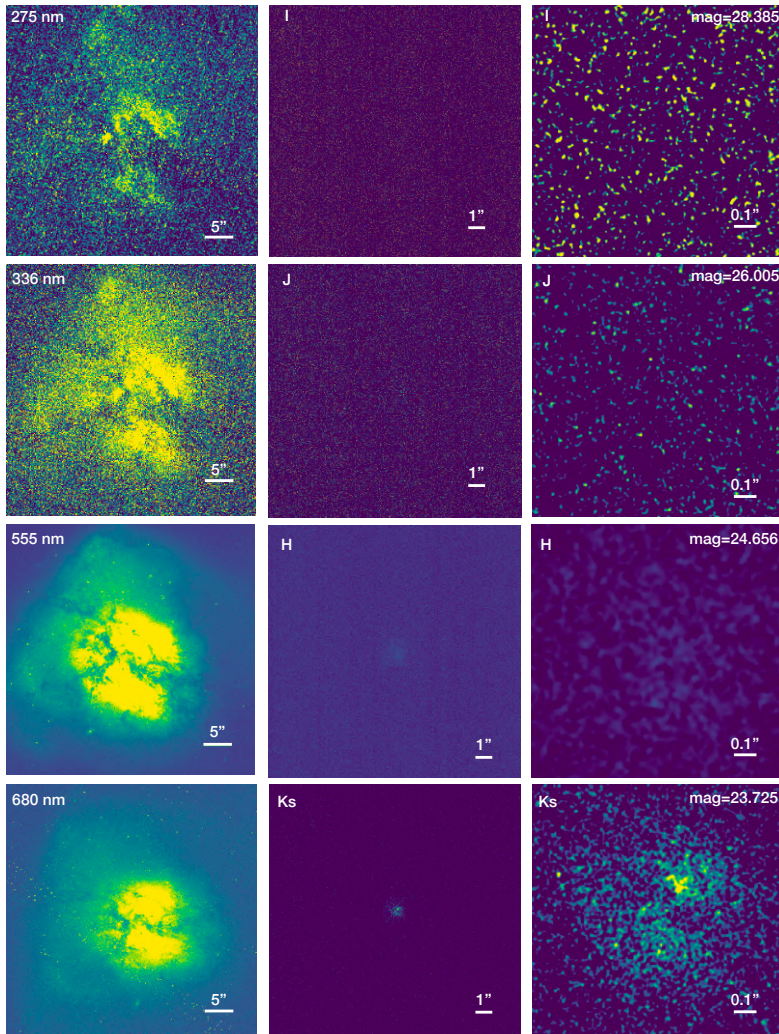


Figure 4.18: SIMCADO simulations for the HST-dark galaxy with ID 41 at  $z=2.23$ . The first, second and third columns correspond to a FoV of  $45'' \times 45''$ ,  $16.4'' \times 16.4''$ , and  $1.2'' \times 1.2''$ , respectively. For each image, we provide the HST filter central wavelength or the MICADO band (top left), the displayed angular scale (bottom), and the magnitude of the simulated galaxy (third column, top right). The images were obtained adopting a total exposure time of  $\sim 16.7$  h. In order to enhance low signal-to-noise features, a Gaussian smoothing with a radius of 3 pixels has been applied to the simulations.

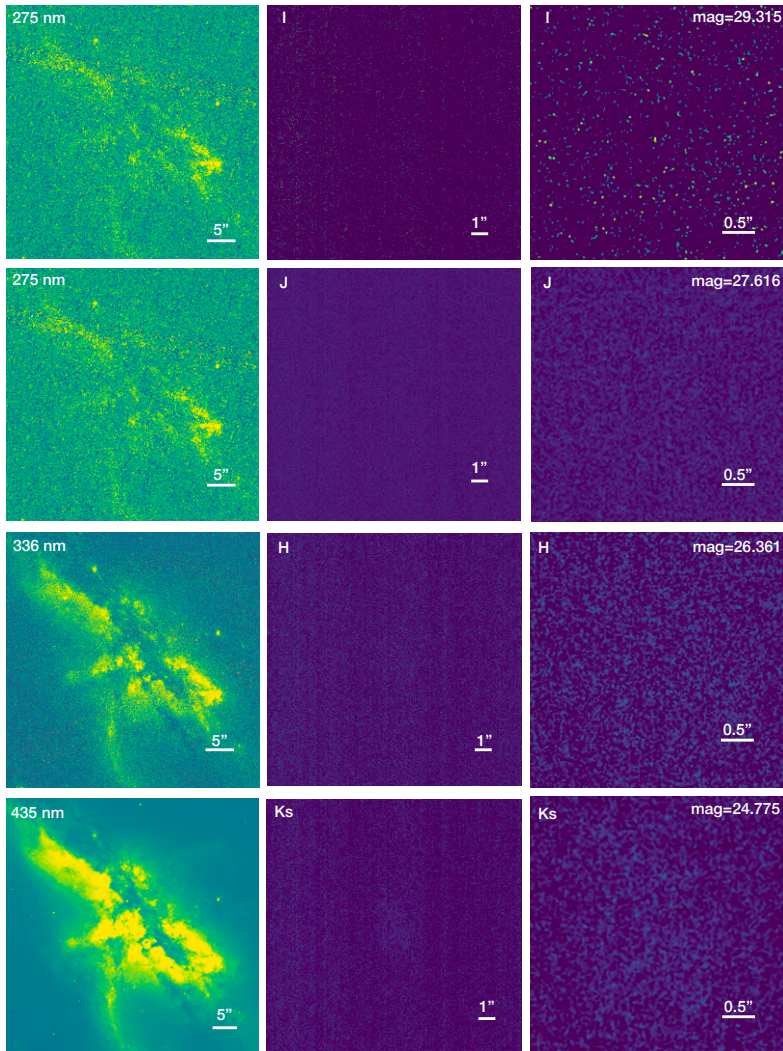


Figure 4.19: SIMCADO simulations for the HST-dark galaxy with ID 48 at  $z=4.08$ . The first, second and third columns correspond to a FoV of  $55'' \times 55''$ ,  $16.4'' \times 16.4''$ , and  $4'' \times 4''$ , respectively. For each image, we provide the HST filter central wavelength or the MICADO band (top left), the displayed angular scale (bottom), and the magnitude of the simulated galaxy (third column, top right). The images were obtained adopting a total exposure time of  $\sim 16.7$  h. In order to enhance low signal-to-noise features, a Gaussian smoothing with a radius of 7 pixels has been applied to the simulations.

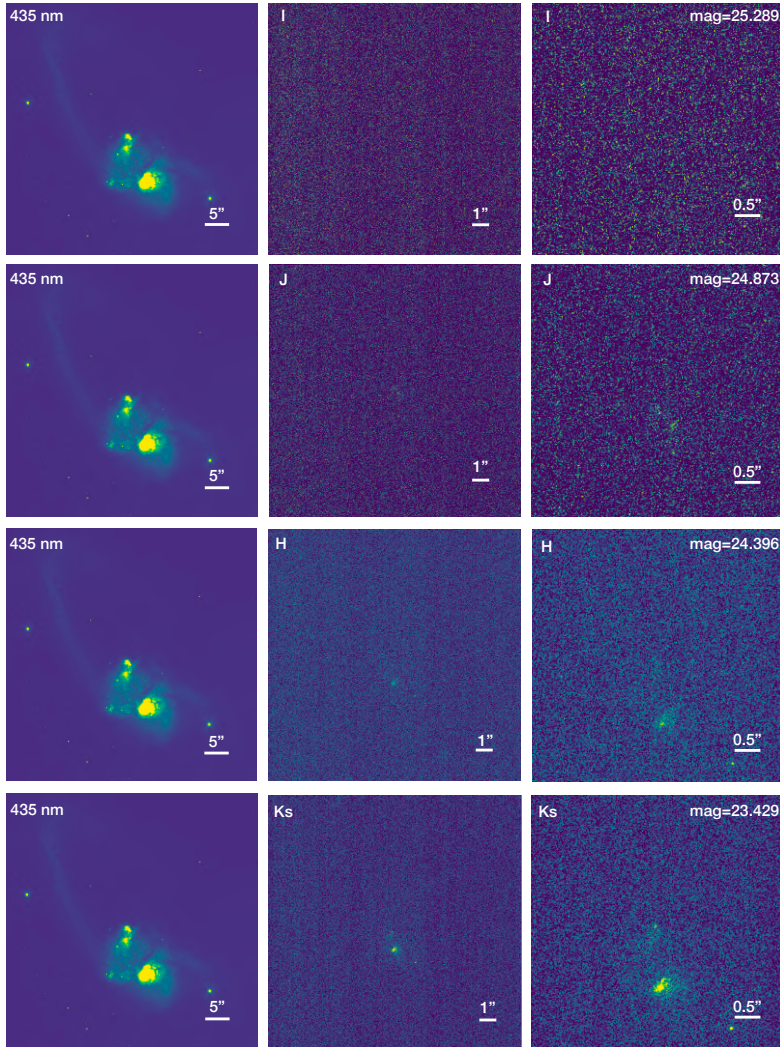


Figure 4.20: SIMCADO simulations for the HST-dark galaxy with ID 54 at  $z=3.43$ . The first, second and third columns correspond to a FoV of  $55'' \times 55''$ ,  $16.4'' \times 16.4''$ , and  $5'' \times 5''$ , respectively. For each image, we provide the HST filter central wavelength or the MICADO band (top left), the displayed angular scale (bottom), and the magnitude of the simulated galaxy (third column, top right). The images were obtained adopting a total exposure time of  $\sim 16.7$  h. In order to enhance low signal-to-noise features, a Gaussian smoothing with a radius of 3 pixels has been applied to the simulations.

As in the case of LIRGs, we note that in all the images these sources do not emerge in lower-wavelength bands, since we are simulating their rest frame UV, which drops in the presence of such a dusty environment. This result does not surprise us since we recall from section 1.4 that these sources are named after their undetectability in optical (and often NIR) wavelengths. Therefore, the H and especially Ks bands are the most suitable to observe these galaxies, if not the only ones. In fact, only in the Ks band we can still recognise the associated morphology in most cases, as we note in fig.4.16, 4.17 or 4.18.

Our simulations show again how compact sources seem to be favoured, as their morphology is still visible to higher redshifts, while extended and low surface brightness ones tend to be undetectable.

An instrument with such a high resolution as the ELT will provide images with unprecedented detail. As we pointed out multiple times, this is particularly important in studies of the high-redshift Universe, in order to shed light on how primordial galaxies form and evolve, as well as to provide the best estimate for the uncertain high-redshift end of SFRD and SMD. Thanks to the high resolution allowed by the ELT, one could clearly observe, in the simulated image of the HST-dark galaxy 12, the clumpy nature of this source (see fig.4.16). Being able to resolve and therefore observe the star-forming regions hosted by such a high-redshift galaxy (in this case  $z=2.85$ , but we simulated the local NGC6090 with the same morphology up to  $z=4$  on the last section) represents an astonishing and unprecedented result, which can be obtained only thanks to the advent of the ELT and its cutting-edge instruments. Indeed, our study demonstrates that, thanks to MORFEO+MICADO@ELT, we will be able to properly characterize the morphologies of HST-dark galaxies provided that these systems (whose nature is currently unknown) are compact, or contain compact high-surface brightness substructures; on the other hand, diffuse and extended systems will be hardly detected at high-redshift with this instrumentation.

In the former case we can infer crucial information about their morphologies and clumpiness, a result not accessible with other current instruments.

### 4.3 Surface Brightness

In order to translate the simulated images (in counts) into physical units, we calculated the surface brightness of the simulated HST-dark galaxies in the

Ks band. We recall the definition of surface brightness as the magnitude of an extended object's flux divided by its solid angle ( $[mag/arcsec^2]$ ), which can be expressed as follows:

$$SB = -2.5\text{Log}_{10}(\text{counts}/t/A) + Z_p \quad (4.1)$$

where  $t$  is the exposure time,  $A$  the area associated with the collected counts, and  $Z_p$  a zero point. In eq.4.1, all quantities are known, except  $Z_p$ . In order to derive the zero point magnitude  $Z_p$ , we use the galaxies' total AB magnitudes calculated and tabulated in section 3.3. In fact, the magnitude of a source can be expressed by the formula:

$$m = -2.5\text{Log}_{10}(\text{counts}/t) + Z_p \quad (4.2)$$

Therefore, we calculate  $Z_p$  inverting eq.4.2, where  $m$  is the galaxy total magnitude tabulated in section 3.3,  $\text{counts}$  are the total counts of the source within a given aperture directly computed from the simulated images, and  $t$  is the simulation exposure time. The derived  $Z_p$  is then used in eq.4.1 to convert the simulated images from counts to SB units. The results are shown in images 4.21 to 4.24, along with the adopted scale and colorbar. Features with typical surface brightness fainter than  $\sim 24 \text{ mag}/arcsec^2$  [Ks band AB mag] are easily lost even adopting very long integration times. These plots refer to HST-dark galaxies with IDs 12, 32, 41 and 54 (specified in the caption), while those with IDs 3 and 48 are not reported. The HST-dark 3 is not shown because, as stated earlier, it has similar morphology and characteristics to the HST-dark 12; for what concerns HST-dark 48 instead, this galaxy is too diffuse and therefore its surface brightness is too low to be detected.

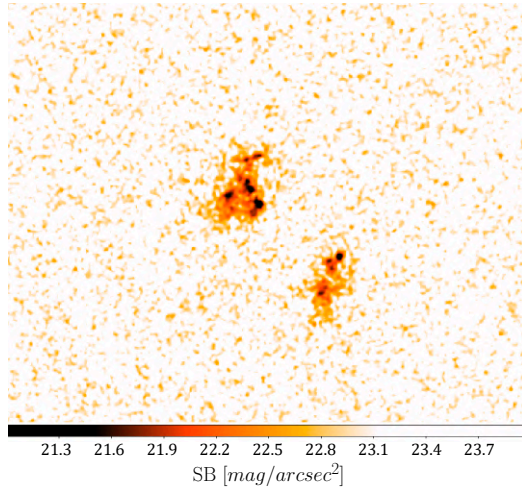


Figure 4.21: Surface brightness image calculated for the HST-dark galaxy 12 in Ks. The scale on the bottom reports the interval of AB surface brightness between 21 and 24. A Gaussian smoothing with a radius of 3 pixels has been applied to the simulations.

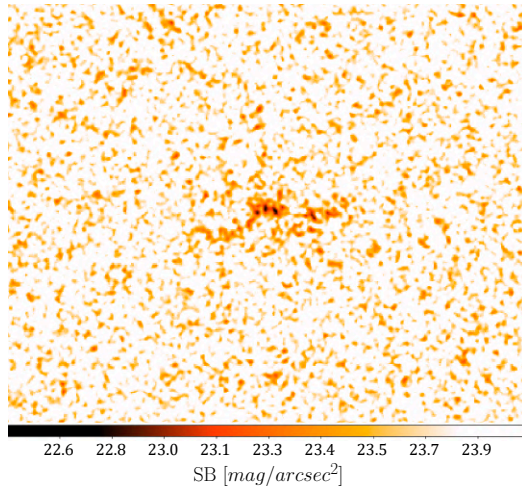


Figure 4.22: Surface brightness image calculated for the HST-dark galaxy 32 in Ks. The scale on the bottom reports the interval of AB surface brightness between 22.5 and 24. A Gaussian smoothing with a radius of 3 pixels has been applied to the simulations.

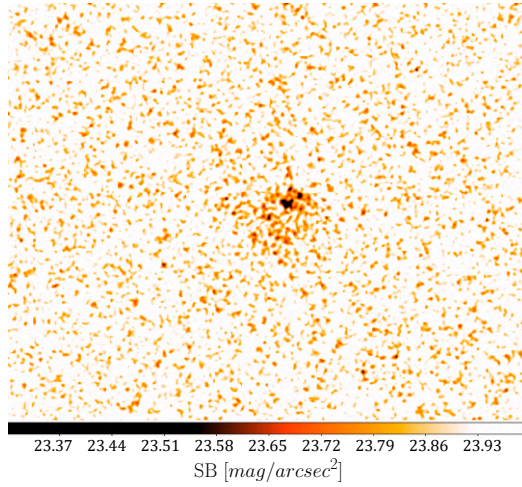


Figure 4.23: Surface brightness image calculated for the HST-dark galaxy 41 in Ks. The scale on the bottom reports the interval of AB surface brightness between 23.3 and 24. A Gaussian smoothing with a radius of 7 pixels has been applied to the simulations.

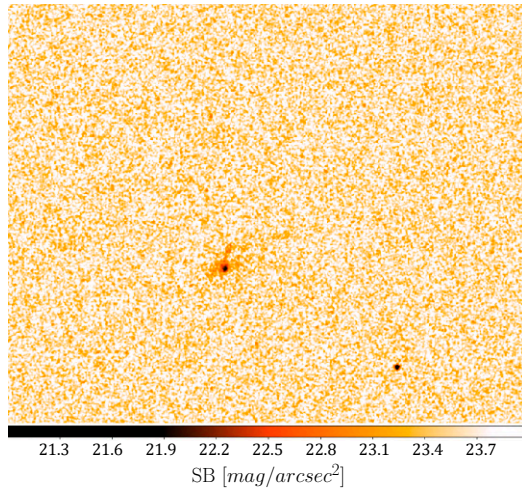


Figure 4.24: Surface brightness image calculated for the HST-dark galaxy 54 in Ks. The scale on the bottom reports the interval of AB surface brightness between 21 and 24. A Gaussian smoothing with a radius of 3 pixels has been applied to the simulations.

We already noted how our SIMCADO simulations confirm that the sur-

face brightness of an high-redshift source is a crucial factor for its detectability with a high spatial resolution instrument. This effect is evident in both cases of LIRGs and HST-dark galaxies, for example comparing the morphologies of NGC6240 and NGC6090. In the case of LIRGs, our simulations show that the morphology of NGC6090 is still observable up to  $z=4$  (see fig.4.12), while NGC6240 seems to be undetectable at the same redshift (see fig.4.9), even if its total integrated flux is brighter. This is because the first one presents a more compact morphology, and thus a higher surface brightness, than the second: NGC6240 is showed in images  $55'' \times 55''$ , whereas NGC6090 in images  $16.4'' \times 16.4''$ .

We can make a similar observation considering the case of HST-dark galaxies and comparing the simulations of HST-dark galaxies with IDs 12 (fig.4.16) and 48 (fig.4.19), which adopt the morphologies of the two local LIRGs mentioned earlier.

Indeed, high-resolution telescopes (e.g. MICADO+MORFEO, with a plate scale of 4 *mas* or 1.5 *mas*) tend to spread the emission of a source on a large number (small size) pixels, making it harder to have a strong and clear detection of low-surface brightness objects. In fact, if we use a detector to observe a certain source, then the smaller is the angular dimension of its pixels (i.e. the plate scale), the less counts each pixel will register. In the same way, if the same detector observes a source with higher surface brightness, then each pixel will register more counts, while if it observes a more extended source, then each pixel will register less counts.

We also derived the Signal-to-Noise Ratio (SNR) map for the HST-dark galaxy 12 in Ks, to measure how well this source can be observed. The result is reported in fig.4.25, along with the adopted scale and colorbar. The image shows, as expected, that the star forming regions are brighter than the diffuse emission of the galaxy, with a maximum value of  $SNR \sim 7.3$ .

In the end, we create a RGB color-combined image for the HST-dark galaxy 12, in order to show the maximum astrophysical content of the simulations in one image. In order to achieve this, we first created a new average image from images in H and Ks  $[(H+Ks)/2]$ . The image displayed in fig.4.26 is obtained from the combination of the H band (blue), the Ks band (red), and the average image from H and Ks (green). This color-combined image highlights more compact, blue, star forming regions against a more diffuse redder population.

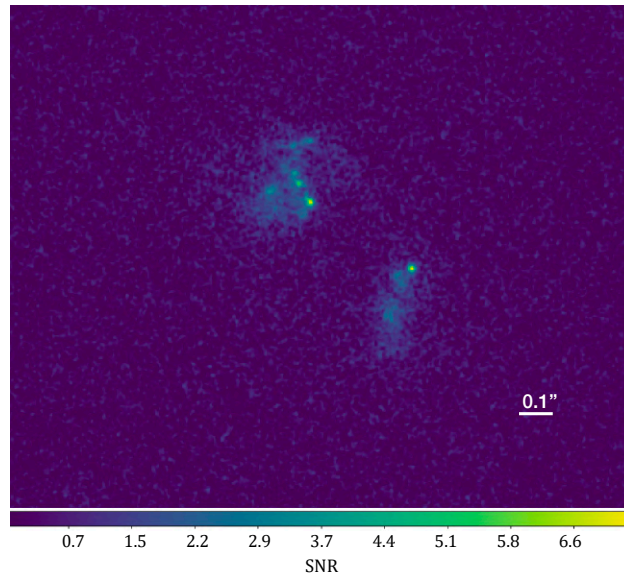


Figure 4.25: SNR map obtained for the HST-dark galaxy 12 in Ks. The scale on the bottom reports the interval of SNR between 0 and 7.3.

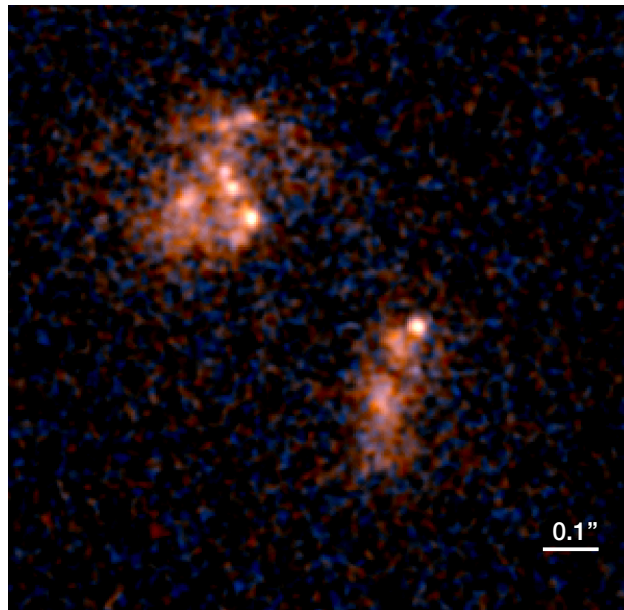


Figure 4.26: RGB image obtained for the HST-dark galaxy 12. The colours represent the emission in the H-band (Blue), H+Ks/2 (Green) and Ks-band (Red).

# Chapter 5

## Discussion and Conclusions

### 5.1 Final Discussion and Comparison with JWST

The results obtained from the simulations reported in Chapter 4 demonstrate the crucial importance of high-resolution observations, enabling us to unveil information that we are missing with current telescopes. We have shown that enigmatic and heavily-obscured objects, such as HST-dark galaxies, have properties which are still largely unknown, since the current instrumentation is unable to detect and resolve them at high redshift. However, in the next future, cutting-edge telescopes such as the JWST will help us to detect obscured sources, as the HST-dark galaxies, but it will be the ELT that will bring a real leap forward in providing details never obtained before. Fig.5.1 shows a comparison of the capabilities of the two new-generation telescopes observing the HST-dark galaxy 12, reporting on the first column the local HST rest-frame images, and the simulation results obtained with MORFEO+MICADO (center) and NIRC@JWST (right) in the other two columns.

MICADO has a resolution power about 6 times better than NIRC@JWST (e.g.  $0.012 \text{ arcsec}$  versus  $0.070 \text{ arcsec}$  at the diffraction limit at  $2.2 \mu\text{m}$ ). Therefore, it is clear how our simulations have finer spatial resolution and allow us to observe details that one would have lost with current telescopes, even with JWST. However, we also note how JWST provides a better and clearer detection; this is due to the fact that, as described in Chapter 4, the high spatial resolution (and small pixel size) of MORFEO+MICADO@ELT disfavors the detection of extended, low surface brightness emission. This example

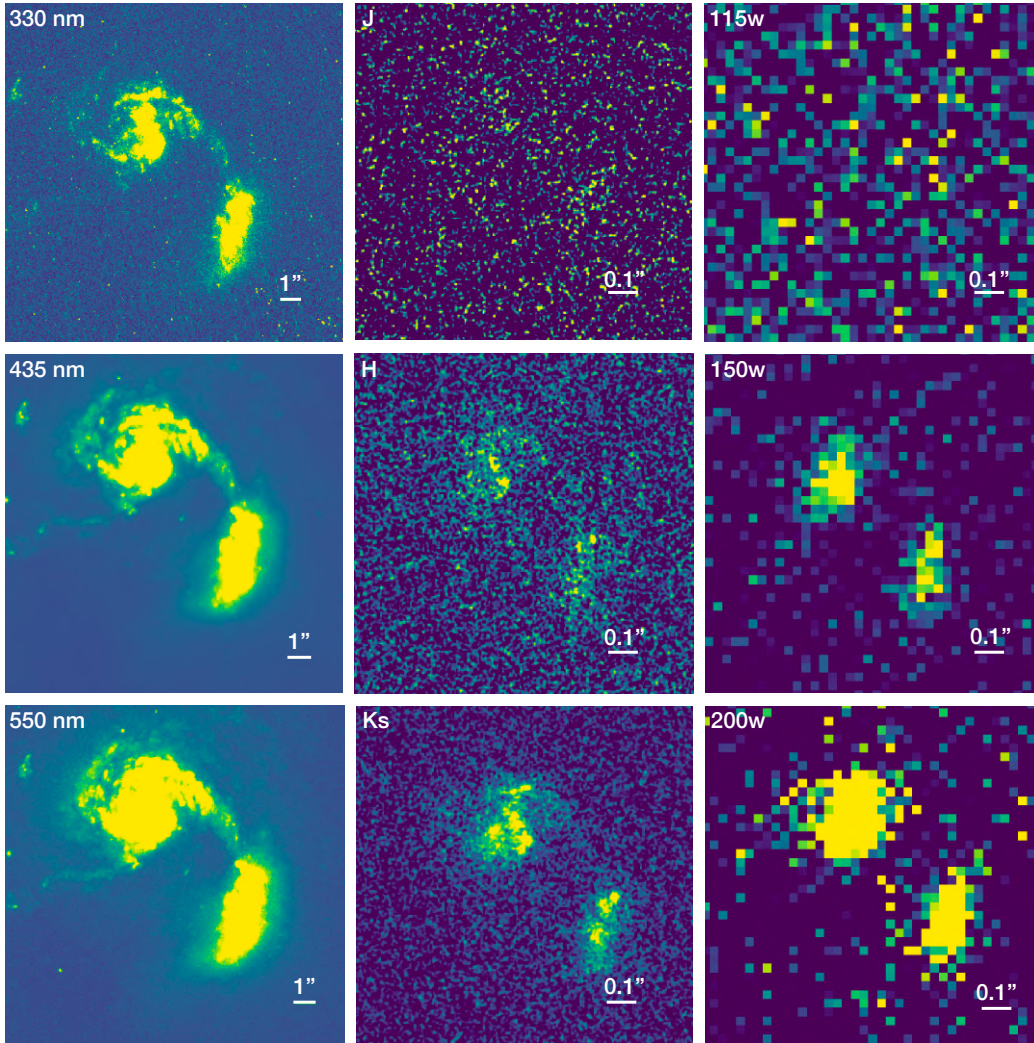


Figure 5.1: Comparison between the capabilities of MORFEO+MICADO@ELT and JWST in observing the HST-dark galaxy with ID 12. The first column shows the local HST rest-frame images, while the second and third columns report the simulations obtained with MORFEO+MICADO and NIRCcam, respectively. The images in the first, second and third columns have a size of  $16.4'' \times 16.4''$ ,  $1.2'' \times 1.2''$ , and  $1.2'' \times 1.2''$ , respectively. Each image reports its wavelength or band on the top left corner and the scale on the bottom right corner.

confirms how critical the synergy between the two instruments is, in terms of efficient detection of faint sources at high redshift by NIRC*am*@JWST and capability to infer sizes and morphologies for the most compact galaxies or their substructures with MORFEO+MICADO@ELT.

In particular, SIMCADO simulations in the middle column of fig.5.1 for the HST-dark galaxy 12 preserve clearly the clumpiness nature of the input NGC6090 morphology up to a photometric redshift of 2.85. As we clarified on Chapter 1, the possibility to observe and distinguish the shape and morphology of high-redshift sources is not only an unprecedented result, but is also of crucial importance to characterize the early Universe. For instance, being able to distinguish peculiar and disturbed morphologies, and/or the presence of two separate nuclei within a galaxy -all features typically associated with merging systems- may provide a plausible explanation for an observed intense star formation activity, which is believed to be triggered by these phenomena. In the case of HST dark galaxies, such results would place these sources in the evolutionary scenario in which they will probably become quiescent and elliptical galaxies after a burst of star formation. Conversely, the detection of regular and disk-like morphologies in high-redshift HST-dark galaxies would imply a challenge for current models of galaxy formation and evolution, making it difficult to understand how sources with this regular shape can have the extreme IR luminosity ( $\sim 10^{11}$ - $10^{12} L_{\odot}$ ) and star formation ( $\sim 10^1$ - $10^2 M_{\odot}/yr$ ) which are observed.

The characterization and morphological study of systems at different redshifts will allow us to better understand the nature of the galaxies that contribute to the high-redshift SFRD and SMD; these are fundamental "tools" to understand how galaxies evolve and change with time, but are currently very uncertain beyond the Cosmic Noon with the current instruments (section 1.2.2). Finding and fully characterizing a portion of the populations of galaxies whose contributions are still not considered in the global SFRD and SMD will allow us to provide better constraints to current galaxy evolution models.

Although in this work we assumed HST-dark galaxies to have morphologies similar to those of local LIRGs for the purpose of our MORFEO+MICADO simulations, future work may extend this approach using a wider and diversified sample of galaxy morphologies and sizes, in order to test the ELT performance for different kinds of sources. Indeed, we may consider a range of very different galaxy shapes (from ellipticals to spirals) and consider also dwarf galaxies, further testing the potential of future MORFEO+MICADO

observations in unveiling the properties of different galaxy types.

We should also consider that high-redshift sources seem to be typically more compact than low-redshift/local ones. Therefore, one should consider an additional shrinking, besides taking into account (see sec.3.2.1) the behaviour of the angular size as a function of redshift. This will positively influence the morphological studies with ELT, since the surface brightness will be higher than considered in this work.

## 5.2 Summary

The work presented in this thesis aims at probing the capabilities of high-resolution telescopes in revolutionizing our view of the high-redshift Universe, enabling us to observe details that until now are lost by using current telescopes. In particular, our study focuses on ESO's Extremely Large Telescope, the largest optical telescope ever built, and simulates how it would observe a peculiar and new class of high-redshift galaxies that escape from the current deepest optical surveys, the HST-dark galaxies. In order to pursue our goal, we used the simulation tool SIMCADO, which produces synthetic images with the same properties as those that will be obtained by the ELT with the combination of its NIR wide-field camera MICADO and its last-generation adaptive optics system MORFEO.

My work can be summarized as follows:

- We considered the sample of six ALMA-selected HST-dark galaxies from [Gruppioni et al. \(2020\)](#), with their best-fit SEDs and photometric redshifts in the range [2.23–5.85].
- As the morphology of these sources is still unknown, we considered a sample of five local LIRGs/ULIRGs in order to associate their morphologies with each HST-dark galaxy, under the assumption that their morphologies are similar, given their SED resemblance (high IR luminosity and strong UV extinction by dust grains). However, a possible and finer approach in the future could be to use for our assumptions a wider and diversified sample of galaxy types, enabling us to test the capabilities of MICADO+MORFEO on very different morphologies (e.g., including ellipticals, spirals and dwarf galaxies).
- In order to simulate how these galaxies would appear at higher-redshift, we had to consider the following effects: objects appear fainter and

smaller at increasing redshift (i.e. there is a flux dimming and also an angular size shrinking with distance). Therefore, we had to adapt the SEDs and local morphologies according to the flux-luminosity distance relation and the scaling relation for the angular dimension, in order to perform high-redshift simulations.

- Finally, we used as inputs for the simulator SIMCADO the assumed parameters, morphologies and SEDs, to create synthetic images in the four principal NIR bands IJHKs and with a pixel size of 4 *mas*. Given our ultimate goal to simulate how HST-dark galaxies will be observed by ELT, we first considered their potentially local analogues, LIRGs and ULIRGs, simulating them to redshifts  $z=2-4$ . Then we proceeded by simulating HST-dark galaxies images after associating the HST images of the LIRG/ULIRG to each high-redshift source.
- Our simulations show that their peculiar and merger-like morphologies are still detectable if shifted at high redshift, and can be seen up to  $z=4$ . Indeed, thanks to the unprecedented angular resolution of MICADO, the simulated images preserve their clumpiness at high redshifts, and allow us to observe the single knots of stellar formation: this result is not possible with current instruments and even with the cutting-edge JWST (fig.5.1).
- As expected, we note a dependence of the source detectability on the observing band. These types of galaxies seem to be undetected in the shorter-wavelengths bands I and J at higher redshifts, corresponding to their rest-frame UV, due to the large extinction in dusty environments. However, we are able to detect and resolve them in the H and (especially) Ks bands, which sample the rest-frame optical spectrum, proving that the H and Ks bands are likely the most suitable ones to observe the obscured side of the high-redshift Universe using the ELT.
- Finally, we noted that compact sources seem to be favoured, as their morphology can still be characterized with high detail, while extended and diffuse ones tend to be undetectable at increasing redshift. Indeed, our SIMCADO simulations confirm that the surface brightness of a high-redshift source is a crucial factor for its detectability using a high-resolution telescope. In fact, high-resolution facilities, like the ELT, tend to spread the emission of larger objects on a large amount of pixels,

making it harder to have a strong and clear detection of low surface brightness components. In the end, MORFEO+MICADO@ELT will work significantly better in the case of observations of galaxies with high surface brightness rather than diffuse and extended ones, suggesting that detailed morphologies and sizes of high-redshift systems will be derived only for the relatively compact galaxies or galaxy substructures.

# Bibliography

- C. Angrick and M. Bartelmann. Triaxial collapse and virialisation of dark-matter haloes. , 518:A38, July 2010. doi: 10.1051/0004-6361/20101414710.48550/arXiv.1001.4984.
- M. Aravena et al. The ALMA Spectroscopic Survey in the Hubble Ultra Deep Field: Search for [CII] Line and Dust Emission in 6. , 833(1):71, December 2016. doi: 10.3847/1538-4357/833/1/71.
- S. Arnouts et al. Measuring the redshift evolution of clustering: the Hubble Deep Field South. , 329(2):355–366, January 2002. doi: 10.1046/j.1365-8711.2002.04988.x.
- G. Bruzual and S. Charlot. Stellar population synthesis at the resolution of 2003. , 344(4):1000–1028, October 2003. doi: 10.1046/j.1365-8711.2003.06897.x.
- A. C. Carnall. SpectRes: A Fast Spectral Resampling Tool in Python. *arXiv e-prints*, art. arXiv:1705.05165, May 2017. doi: 10.48550/arXiv.1705.05165.
- C. M. Casey, D. Narayanan, and A. Cooray. Dusty star-forming galaxies at high redshift. , 541(2):45–161, August 2014. doi: 10.1016/j.physrep.2014.02.009.
- G. Chabrier. Galactic Stellar and Substellar Initial Mass Function. , 115 (809):763–795, July 2003. doi: 10.1086/37639210.48550/arXiv.astro-ph/0304382.
- L. Chomiuk and M. S. Povich. Toward a Unification of Star Formation Rate Determinations in the Milky Way and Other Galaxies. , 142(6):197, December 2011. doi: 10.1088/0004-6256/142/6/197.

- Event Horizon Telescope Collaboration. First M87 Event Horizon Telescope Results. I. The Shadow of the Supermassive Black Hole. , 875(1):L1, April 2019. doi: 10.3847/2041-8213/ab0ec7.
- J. Courtin et al. Imprints of dark energy on structure formation : no universality in mass functions? In *Invisible Universe*, volume 1241 of *American Institute of Physics Conference Series*, pages 804–810, June 2010. doi: 10.1063/1.3462720.
- O. Cucciati et al. The star formation rate density and dust attenuation evolution over 12 Gyr with the VVDS surveys. , 539:A31, March 2012. doi: 10.1051/0004-6361/201118010.
- T. Dahlen et al. Evolution of the Luminosity Function, Star Formation Rate, Morphology, and Size of Star-forming Galaxies Selected at Rest-Frame 1500 and 2800 Å. , 654(1):172–185, January 2007. doi: 10.1086/508854.
- K. M. Dasyra et al. Dynamical Properties of Ultraluminous Infrared Galaxies. II. Traces of Dynamical Evolution and End Products of Local Ultraluminous Mergers. , 651(2):835–852, November 2006. doi: 10.1086/507834.
- I. Davidzon et al. The COSMOS2015 galaxy stellar mass function . Thirteen billion years of stellar mass assembly in ten snapshots. , 605:A70, September 2017. doi: 10.1051/0004-6361/20173041910.48550/arXiv.1701.02734.
- R. Davies et al. MICADO: first light imager for the E-ELT. In *Ground-based and Airborne Instrumentation for Astronomy VI*, volume 9908 of *SPIE Conference Series*, page 99081Z, August 2016. doi: 10.1117/12.2233047.
- R. Davies et al. The MICADO first light imager for the ELT: overview, operation, simulation. In *Ground-based and Airborne Instrumentation for Astronomy VII*, volume 10702 of *SPIE Conference Series*, page 107021S, July 2018. doi: 10.1117/12.2311483.
- A. Dey et al. Observations of a  $Z = 1.44$  Dusty, Ultraluminous Galaxy and Implications for Deep Submillimeter Surveys. , 519(2):610–621, July 1999. doi: 10.1086/30739510.48550/arXiv.astro-ph/9902044.
- N. Dinshaw et al. NICMOS Observations of Interaction-triggered Star Formation in the Luminous Infrared Galaxy NGC 6090. , 525(2):702–708, November 1999. doi: 10.1086/307920.

- J. Dunlop et al. A deep ALMA image of the Hubble Ultra Deep Field. , 466 (1):861–883, April 2017. doi: 10.1093/mnras/stw3088.
- A. Enia et al. A New Estimate of the Cosmic Star Formation Density from a Radio-selected Sample, and the Contribution of H-dark Galaxies at  $z \geq 3$ . , 927(2):204, March 2022. doi: 10.3847/1538-4357/ac51ca.
- J. M. Espinosa and P. Alvarez Martin. Gran Telescopio Canarias: a 10-m telescope for the ORM. In *Optical Telescopes of Today and Tomorrow*, volume 2871 of *SPIE Conference Series*, pages 69–73, March 1997.
- G. Fiorentino et al. Deep into the core of dense star clusters: an astrometric and photometric test case for ELT. , 494(3):4413–4425, May 2020. doi: 10.1093/mnras/staa869.
- M. Franco et al. GOODS-ALMA: 1.1 mm galaxy survey. I. Source catalog and optically dark galaxies. , 620:A152, December 2018. doi: 10.1051/0004-6361/201832928.
- C. Gómez-Guijarro et al. GOODS-ALMA 2.0: Source catalog, number counts, and prevailing compact sizes in 1.1 mm galaxies. , 658:A43, February 2022. doi: 10.1051/0004-6361/202141615.
- C. Gruppioni et al. The Herschel PEP/HerMES luminosity function - I. Probing the evolution of PACS selected Galaxies to  $z \leq 4$ . , 432(1):23–52, June 2013. doi: 10.1093/mnras/stt308.
- C. Gruppioni et al. The ALPINE-ALMA [CII] survey. The nature, luminosity function, and star formation history of dusty galaxies up to  $z \leq 6$ . , 643:A8, November 2020. doi: 10.1051/0004-6361/202038487.
- B. Hatsukade et al. ALMA twenty-six arcmin<sup>2</sup> survey of GOODS-S at one millimeter (ASAGAO): Source catalog and number counts. , 70(6):105, December 2018. doi: 10.1093/pasj/psy104.
- J. M. Hill and P. Salinari. Large Binocular Telescope Project. In *Advanced Technology Optical/IR Telescopes VI*, volume 3352 of *SPIE Conference Series*, pages 23–33, August 1998. doi: 10.1117/12.319271.
- P. F. Hopkins et al. A Cosmological Framework for the Co-Evolution of Quasars, Supermassive Black Holes, and Elliptical Galaxies. I. Galaxy

- Mergers and Quasar Activity. , 175(2):356–389, April 2008. doi: 10.1086/524362.
- S. B. Howell. The grand challenges of exoplanets. *Frontiers in Astronomy and Space Sciences*, 7, 2020. ISSN 2296-987X. doi: 10.3389/fspas.2020.00010.
- O. Ilbert et al. Accurate photometric redshifts for the CFHT legacy survey calibrated using the VIMOS VLT deep survey. , 457(3):841–856, October 2006. doi: 10.1051/0004-6361:20065138.
- G. Kauffmann et al. The formation and evolution of galaxies within merging dark matter haloes. , 264:201–218, September 1993. doi: 10.1093/mnras/264.1.201.
- R. C. Kennicutt Jr. Star Formation in Galaxies Along the Hubble Sequence. , 36:189–232, January 1998a. doi: 10.1146/annurev.astro.36.1.18910.48550/arXiv.astro-ph/9807187.
- R. C. Kennicutt Jr. The Global Schmidt Law in Star-forming Galaxies. , 498(2):541–552, May 1998b. doi: 10.1086/305588.
- P. Kroupa. On the variation of the initial mass function. , 322(2):231–246, April 2001. doi: 10.1046/j.1365-8711.2001.04022.x10.48550/arXiv.astro-ph/0009005.
- C. Lacey and S. Cole. Merger rates in hierarchical models of galaxy formation. , 262(3):627–649, June 1993. doi: 10.1093/mnras/262.3.627.
- K. Leschinski et al. SimCADO: an instrument data simulator package for MICADO at the E-ELT. In *Modeling, Systems Engineering, and Project Management for Astronomy VI*, volume 9911 of *SPIE Conference Series*, page 991124, August 2016. doi: 10.1117/12.2232483.
- L. Lindegren et al. Gaia Early Data Release 3. Parallax bias versus magnitude, colour, and position. , 649:A4, May 2021. doi: 10.1051/0004-6361/202039653.
- F. Loiacono et al. The ALPINE–ALMA [c II] survey. *Astronomy & Astrophysics*, 646:A76, feb 2021. doi: 10.1051/0004-6361/202038607.

- C. C. Lovell et al. FLARES VIII. The Emergence of Passive Galaxies in the Early Universe ( $z > 5$ ). *arXiv e-prints*, art. arXiv:2211.07540, November 2022.
- P. Madau and M. Dickinson. Cosmic Star-Formation History. , 52:415–486, August 2014. doi: 10.1146/annurev-astro-081811-125615.
- B. Magnelli et al. Evolution of the dusty infrared luminosity function from  $z = 0$  to  $z = 2.3$  using observations from Spitzer. , 528:A35, April 2011. doi: 10.1051/0004-6361/200913941.
- B. Magnelli et al. The deepest Herschel-PACS far-infrared survey: number counts and infrared luminosity functions from combined PEP/GOODS-H observations. , 553:A132, May 2013. doi: 10.1051/0004-6361/201321371.
- G. E. Miller and J. M. Scalo. The Initial Mass Function and Stellar Birthrate in the Solar Neighborhood. , 41:513, November 1979. doi: 10.1086/190629.
- J. Nelson. The Keck Telescope Project. In *The Next Generation Space Telescope*, page 99, January 1990.
- J. B. Oke and J. E. Gunn. Secondary standard stars for absolute spectrophotometry. , 266:713–717, March 1983. doi: 10.1086/160817.
- P. J. E. Peebles. Large-scale background temperature and mass fluctuations due to scale-invariant primeval perturbations. , 263:L1–L5, December 1982. doi: 10.1086/183911.
- P. J. E. Peebles. *Principles of Physical Cosmology*. 1993. doi: 10.1515/9780691206721.
- P. G. Pérez-González et al. CEERS Key Paper V: A triality on the nature of HST-dark galaxies. *arXiv e-prints*, art. arXiv:2211.00045, October 2022.
- Planck Collaboration et al. Planck 2015 results. XIII. Cosmological parameters. , 594:A13, September 2016. doi: 10.1051/0004-6361/201525830.
- M. Polletta et al. Spectral Energy Distributions of Hard X-Ray Selected Active Galactic Nuclei in the XMM-Newton Medium Deep Survey. , 663(1):81–102, July 2007. doi: 10.1086/518113.

- M. E. Putman. An introduction to gas accretion onto galaxies. In *Gas Accretion onto Galaxies*, pages 1–13. Springer International Publishing, 2017. doi: 10.1007/978-3-319-52512-9\_1.
- N. A. Reddy and C. C. Steidel. A Steep Faint-End Slope of the UV Luminosity Function at  $z \sim 2-3$ : Implications for the Global Stellar Mass Density and Star Formation in Low-Mass Halos. , 692(1):778–803, February 2009. doi: 10.1088/0004-637X/692/1/778.
- D. A. Riechers et al. VLA-ALMA Spectroscopic Survey in the Hubble Ultra Deep Field (VLASPECS): Total Cold Gas Masses and CO Line Ratios for  $z = 2-3$  Main-sequence Galaxies. , 896(2):L21, June 2020. doi: 10.3847/2041-8213/ab9595.
- T. P. Robitaille and B. A. Whitney. The Present-Day Star Formation Rate of the Milky Way Determined from Spitzer-Detected Young Stellar Objects. , 710(1):L11–L15, February 2010. doi: 10.1088/2041-8205/710/1/L11.
- V. Sahni and A. Starobinsky. The Case for a Positive Cosmological  $\Lambda$ -Term. *International Journal of Modern Physics D*, 9(4):373–443, January 2000. doi: 10.1142/S0218271800000542.
- E. E. Salpeter. The Luminosity Function and Stellar Evolution. , 121:161, January 1955. doi: 10.1086/145971.
- D. Sanders et al. Ultraluminous Infrared Galaxies and the Origin of Quasars. , 325:74, February 1988. doi: 10.1086/165983.
- D. Sanders et al. The IRAS Revised Bright Galaxy Sample. , 126(4):1607–1664, October 2003a. doi: 10.1086/376841.
- D. B. Sanders et al. The IRAS Revised Bright Galaxy Sample. , 126(4):1607–1664, October 2003b. doi: 10.1086/376841.
- D. Schiminovich et al. The GALEX-VVDS Measurement of the Evolution of the Far-Ultraviolet Luminosity Density and the Cosmic Star Formation Rate. , 619(1):L47–L50, January 2005. doi: 10.1086/427077.
- N. Z. Scoville et al. NICMOS Imaging of the Nuclei of Arp 220. , 492(2):L107–L110, January 1998. doi: 10.1086/311099.

- R. K. Sheth et al. Ellipsoidal collapse and an improved model for the number and spatial distribution of dark matter haloes. , 323(1):1–12, May 2001. doi: 10.1046/j.1365-8711.2001.04006.x.
- J. Simpson et al. An ALMA Survey of Submillimeter Galaxies in the Extended Chandra Deep Field South: The Redshift Distribution and Evolution of Submillimeter Galaxies. , 788(2):125, June 2014. doi: 10.1088/0004-637X/788/2/125.
- A. Swinbank et al. An ALMA survey of sub-millimetre Galaxies in the Extended Chandra Deep Field South: the far-infrared properties of SMGs. , 438(2):1267–1287, February 2014. doi: 10.1093/mnras/stt2273.
- T. T. Takeuchi et al. The Luminosity Function of IRAS Point Source Catalog Redshift Survey Galaxies. , 587(2):L89–L92, April 2003. doi: 10.1086/375181.
- M. Talia et al. Illuminating the Dark Side of Cosmic Star Formation Two Billion Years after the Big Bang. , 909(1):23, March 2021. doi: 10.3847/1538-4357/abd6e3.
- D. Thomas et al. Environment and self-regulation in galaxy formation. , 404(4):1775–1789, June 2010. doi: 10.1111/j.1365-2966.2010.16427.x10.48550/arXiv.0912.0259.
- S. Vattakunnel et al. The radio–X-ray relation as a star formation indicator: results from the Very Large Array–Extended Chandra Deep Field–South. *Monthly Notices of the Royal Astronomical Society*, 420(3):2190–2208, 02 2012. ISSN 0035-8711. doi: 10.1111/j.1365-2966.2011.20185.x.
- F. Walter et al. ALMA Spectroscopic Survey in the Hubble Ultra Deep Field: Survey Description. , 833(1):67, December 2016. doi: 10.3847/1538-4357/833/1/67.
- F. Wang et al. A Survey of Luminous High-redshift Quasars with SDSS and WISE. I. Target Selection and Optical Spectroscopy. , 819(1):24, March 2016. doi: 10.3847/0004-637X/819/1/24.
- T. Wang et al. A dominant population of optically invisible massive galaxies in the early Universe. , 572(7768):211–214, August 2019. doi: 10.1038/s41586-019-1452-4.

- W. Wang et al. Ultradeep Near-Infrared Observations of Goods 850-5. , 690 (1):319–329, January 2009. doi: 10.1088/0004-637X/690/1/31910.48550/arXiv.0805.3503.
- C. C. Williams et al. Discovery of a Dark, Massive, ALMA-only Galaxy at  $z \sim 5-6$  in a Tiny 3 mm Survey. , 884(2):154, October 2019. doi: 10.3847/1538-4357/ab44aa.
- E. L. Wright. A Cosmology Calculator for the World Wide Web. , 118(850): 1711–1715, December 2006. doi: 10.1086/510102.
- T. K. Wyder et al. The Ultraviolet Galaxy Luminosity Function in the Local Universe from GALEX Data. , 619(1):L15–L18, January 2005. doi: 10.1086/424735.
- Y. Yamaguchi et al. ALMA 26 arcmin<sup>2</sup> Survey of GOODS-S at 1 mm (ASAGAO): Near-infrared-dark Faint ALMA Sources. , 878(1):73, June 2019. doi: 10.3847/1538-4357/ab0d22.